Universidad Autónoma de Madrid

Departamento de Física de la Materia Condensada

THE INFLUENCE OF MORPHOLOGY AND LONG RANGE INTERACTIONS ON THE ELECTRONIC PROPERTIES OF GRAPHENE

Memoria de la tesis presentada por

Fernando de Juan Sanz

para optar al grado de Doctor en Ciencias Físicas

Directora:

María Ángeles Hernández Vozmediano

Madrid, Abril de 2010

Contents

List of acronyms

This is a list of the acronyms used in the text:

- **2DEG** Two-dimensional Electron Gas
- **AFM** Atomic Force Microscopy
- **ARPES** Angle Resolved Photoemission Spectroscopy
- **DFT** Density Functional Theory
- **DOS** Density Of States
- **EDC** Energy Distribution Curves
- **LDOS** Local Density Of States
- **MDC** Momentum Distribution Curves
- **QED** Quantum Electrodynamics
- **QFT** Quantum Field Theory
- **QHE** Quantum Hall Effect
- **RG** Renormalization Group
- **RPA** Random Phase Approximation
- **SCBA** Self Consistent Born Approximation
- **SCTM** Self Consistent T-Matrix (approximation)
- **STM** Scanning Tunneling Microscopy
- **SW** Stone-Wales (defect)
- **TEM** Transmission Electron Microscopy

Publications

Part of the work presented in this thesis has given rise to the following publications:

- "*Charge inhomogeneities due to smooth ripples in graphene sheets*"

  F. de Juan, A. Cortijo and M.A.H. Vozmediano, Phys. Rev. B **76**, 165409 (2007).

- "*Dislocations in graphene*"

  A. Carpio, L.L. Bonilla, F. de Juan, M.A.H. Vozmediano, New J. Phys. **10**, 053021 (2008).

- "*Gauge fields and curvature in graphene*"

  M.A.H. Vozmediano, F. de Juan, A. Cortijo, J. Phys.: Conf. Ser. **129**, 012001 (2008).

- "*Magnetic moments in the presence of topological defects in graphene*"

  M.P. López-Sancho, F. de Juan, M.A.H. Vozmediano, Phys. Rev. B **79**, 075413 (2009).

- "*Shuffle dislocation induced magnetic moment in graphene*"

  M.P. López-Sancho, F. de Juan, M.A.H. Vozmediano, J. Magn. Magn. Mater. **332**, 1167 (2010)

- "*Dislocations and torsion in graphene and related systems*"

  F. de Juan, A. Cortijo, M.A.H. Vozmediano, Nucl. Phys. B **828**, 625 (2010)

- "*Renormalization of Coulomb interaction in graphene: Computing observable quantities*"

  A. G. Grushin, F. de Juan, M.A.H. Vozmediano, cond-mat/1002.3111

Agradecimientos

En primer lugar quiero agradecerle a Geli, mi directora de tesis, el haberme dado la oportunidad de trabajar con ella, y gran el esfuerzo que ha hecho para que la tesis saliera adelante. Su labor como directora ha sido vital en el desarrollo de la tesis, y he aprendido mucho de su manera de ver la física.

Agradezco también a Guillermo Gómez Santos por haber sido mi tutor en la UAM, con quien también he tenido interesantes discusiones.

El trabajo de esta tesis ha sido realizado en colaboracion con varios investigadores a los que también quiero dar las gracias: Luis Bonilla, Ana Carpio y Pilar López Sancho. A Alberto Cortijo le agradezco particularmente por su inestimable ayuda, sobre todo en los primeros años de tesis, y por todas las discusiones sobre física, donde he aprendido de su creatividad y originalidad. También agradezco a Fito, con quien es siempre un placer discutir.

A Klaus Ziegler me gustaría agradecerle que me acogiera en su grupo de Augsburg, donde también aprendí otra manera de hacer física. A Euyheon Hwang le agradezco su paciencia en Santa Bárbara, siempre dispuesto a explicarme con más detalles algún problema que encontrara.

El ambiente de trabajo en el ICMM ha sido siempre estimulante y quiero agradecer a todos lo que han hecho esto posible: A Paco, Ramón, Belén, Leni, Rafa, Simone, Débora, Gladys y Eduardo. También a todos mis compañeros de tesis, Juan Luis, Alberto, Javi, María, David, Carlos y Laura. Me gustaría mencionar también a Andrés Castellanos, por muchas discusiones interesantes sobre aspectos experimentales para mi desconocidos.

También quiero agradecer a los miembros de Within Experimental Error, que también han contribuido siempre al ambiente de camaradería en el ICMM que he apreciado mucho.

En el plano más personal, hay muchos amigos a mi alrededor a los que me gustaría agradecer su paciencia y apoyo durante todos los años de tesis. Agradezco a mis amigos de la carrera, Javi y Teresa, Ana, Gonzalo, Hector, Emilio y tantos otros que han compartido conmigo las comidas en la facultad de psicología, y que siempre han estado presentes cuando los he necesitado. Agradezco en particular también a Juan, Marta, y Elena.

A mis compañeros de piso durante estos años, Javi, Elena, Rebeca, Domingo y Zoe, les agradezco también la paciencia y la comprensión que me han brindado, y los buenos momentos que hemos pasado. Mis amigos A Javi, Gus, María, Rocío y Paula también me han apoyado enormemente durante la tesis y me han animado en todo momento, algo que también les agradezco.

Finalmente quiero agradecer a mi familia por el apoyo que me han dado desde principio de la tesis, porque siempre serán un referente para mí. Y a Noe le agradezco haber estado a mi lado incondicionalmente este último de año de tesis.

A todos vosotros, gracias.

Abstract

This thesis is concerned with the physics of graphene, a novel two dimensional material that has generated a lot of activity in the last years. The interest in this material relies on a number of features that make it the ideal playground to study some fundamental physics issues, as well as a viable candidate for potential applications. This work has addressed two problems of great interest in the physics of this material: the influence of morphology on its electronic properties and the effects of long range interactions.

The structural features of graphene are essential to understand its electronic properties. In this work, morphology is modelled from the complementary approaches of lattice models and continuum theories. The electronic structure of samples with topological defects is computed from a tight binding model, and the magnetic properties of the system are evaluated in a mean field Hubbard model. It is shown that magnetism is affected significantly by topological defects, which break the bipartite nature of the lattice.

As an alternative approach, the effects of morphology are evaluated in low energy continuum theories. It is proposed that electrons in corrugated graphene sheets are described by the Dirac equation in the corresponding curved background metric. It is shown how this geometrical model reproduces the effective gauge field obtained in the elasticity approach, and predicts the additional effect of the variable Fermi velocity, which has observable consquences in tunneling spectroscopy experiments.

These scheme can naturally incorporate topological defects: Disclinations are singular sources of curvature, and dislocations are modelled by torsion. The coupling of Dirac fermions to torsion is discussed in two and three dimensions and applications to related systems are described.

In this system, Coulomb interactions remain long ranged due to a vanishing density of states at the Fermi level, and their treatment always represents a difficult problem. In this work, both the effects of Coulomb impurities and electron-electron Coulomb interactions are addressed. The spectral properties of doped graphene in the presence of RPA screened random Coulomb impurities are studied by numerically solving the self-consistent Born approximation, computing the density of states, lifetime, and spectral function. The regime of doping where the SCBA improves on the first order known results is identified, and the validity of the approximations used is discussed.

Finally, it is discussed how observables are computed in the renormalized theory for the interacting many-body problem, showing how to relate the theoretical computation with

experiments to a given order in perturbation theory. The similarities of this process with the determination of the fine structure constant in QED are emphasized, discussing the possible ways of measuring the renormalized Fermi velocity. The first Coulomb corrections to the optical conductivity are computed as an example of the renormalization procedure.

Resumen

Esta tesis trata sobre la física del grafeno, un nuevo material bidimensional que ha generado gran cantidad de actividad en los últimos años. El interés de este material reside en varias propiedades inusuales que lo convierten en un sistema ideal para estudiar algunos problemas de física fundamental, así como en un candidato viable para aplicaciones. Este trabajo trata sobre dos problemas de gran interés en la física de este material: La influencia de la morfología en las propiedades electrónicas y los efectos de las interacciones de largo alcance.

Las características estructurales del grafeno son esenciales para entender sus propiedades electrónicas. En este trabajo se ha modelizado la morfología desde dos enfoques complementarios: modelos en la red y teorías continuas. La estructura electrónica de muestras con defectos topológicos se ha calculado con un modelo tipo tight binding, y las propiedades magnéticas has sido evaluadas en campo medio en el modelo de Hubbard. Se ha mostrado como los defectos topológicos, que hacen la red no bipartita, afectan de forma significativa al magnetismo de las muestras.

Los efectos de la morfología también han sido estudiados desde el enfoque complementario de las teorías en el continuo. Se ha propuesto describir los electrones en muestras de grafeno corrugado por la ecuación de Dirac en la métrica curva correspondiente. Se ha mostrado como este formalismo reproduce el campo gauge efectivo obtenido en la teoría de la elasticidad, y además predice el efecto adicional de la velocidad de Fermi variable, que tiene consecuencias observables en experimentos de espectroscopía túnel.

Los defectos topológicos también se pueden incluir de forma natural en este esquema: Las disclinaciones son fuentes de curvatura, y las dislocaciones se describen con torsión. Se ha discutido el acoplo de fermiones de Dirac a la torsion en dos y tres dimensiones, describiéndose también aplicaciones de este formalismo para sistemas relacionados.

En este sistema, las interacciones de Coulomb son de largo alcance debido a la densidad de estados nula al nivel de Fermi, y su tratamiento siempre representa un problema difícil. En este trabajo se han tratado los efectos tanto de las impurezas de Coulomb como de las interacciones de Coulomb entre electrones. Se han estudiado las propiedades espectrales de grafeno dopado en presencia de éstas impurezas, apantalladas en la aproximación RPA y distribuídas aleatoriamente, mediante la aproximación de Born autoconsistente. Se han calculado la densidad de estados, la vida media, y la función espectral. Se ha identificado el régimen donde este cálculo mejora los resultados ya conocidos del primer orden en teoría de perturbaciones, y se ha discutido la validez de las aproximaciones empleadas.

Finalmente se ha discutido el cálculo de observables en la teoría renormalizada para el problema de muchos cuerpos en interacción en grafeno, mostrando como relacionar el cálculo teórico con experimentos a un orden dado en teoría de perturbaciones. Se ha enfatizado la semejanza de este proceso con la determinación de la constante de estructura fina en electrodinámica cuántica, y se han discutido las posibles maneras de medir la velocidad de Fermi renormalizada. Como ejemplo del proceso de renormalización se han calculado las primeras correciones de la interación a la conductividad óptica.

1 Introduction

In this introductory chapter, we review the main features of the physical system studied in this thesis: graphene. We will discuss its structural and electronic properties, commenting on the most interesting problems they pose. We will then explain the organization of the thesis, briefly summarizing the works that are going to be presented.

1.1 Graphene

In the last six years, the condensed matter physics community has witnessed how graphene, the two dimensional allotrope of carbon, has rapidly become one of the new protagonists of the field, generating an enormous amount of activity. In this introduction, we will review the key features that have made graphene so attractive from the points of view of both basic sience and applications, and which explain why graphene has rightfully acquired the renowned status it holds today. While research in graphene has reached by now a certain degree of maturity, many interesting (and some hard) problems still remain to be understood, and many challenges remain open.

Since the isolation of graphene in 2004, the literature on the field has been growing at a rate that makes it difficult to keep up with all new developments. Inevitably, a comprehensive review of them is out of the scope (and purpose) of this introduction. Therefore, we will rather give an overview of the field, highlighting the most remarkable achievements, with a particular focus, when appropriate, on those most related to the work done in this thesis. For further information, we refer to the existing reviews on the subject, see for example [1, 2] from the experimental point of view and [3–6] for more theory oriented ones. We will also refer extensively to the very complete theory review [7]. For a good introduction to the field see also [8].

1.1.1 Graphene as a two dimensional crystal

Graphene is a two dimensional crystal of carbon atoms, arranged in a honeycomb (or hexagonal) lattice, see fig. 1.2. It can be thought of as the building block of other well studied carbon allotropes, such as graphite, carbon nanotubes, and fullerenes, also shown in the figure, and in fact it has been considered theoretically as the starting point for modelling such systems much before its synthesis [9].

However, it used to be common belief that, in real life, two dimensional crystals would not exist because thermal fluctuations would make them unstable at any temperature. It thus came as a surprise that, in 2004, graphene was for the first time isolated [10] by the group lead by A. Geim and K. Novoselov. (Soon after, several other two dimensional crystals were reported [11].) The method they used to isolate graphene was to mechanically cleave it from graphite samples, and then deposit it on a substrate. Their discovery immediately prompted an outburst of both theoretical and experimental activity in the field.

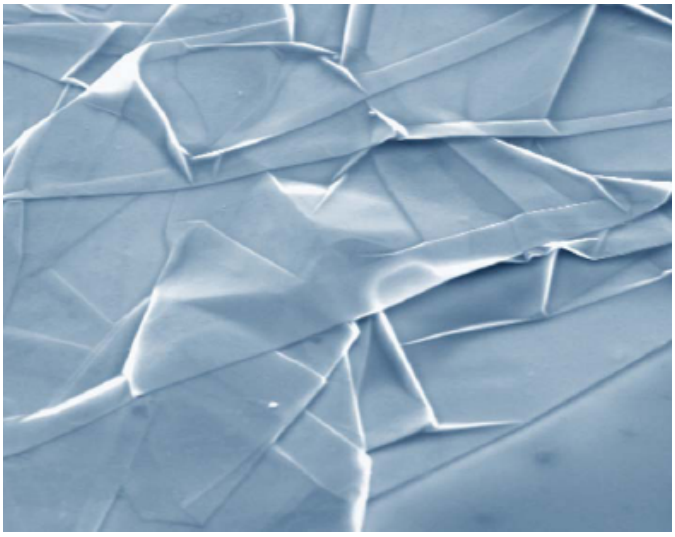

Figure 1.1: Scanning electron microscope image of single layer graphene flakes. Image taken from [8]

As it has been noted before [8], the challenge with graphene was more to see it than to produce it, because after this process the detection of monolayer samples with an optical microscope was not easy [12]. After six years, several other ways of preparing and identifying graphene samples have by now been proposed [1] and graphene is now studied in many laboratories around the world.

This first remarkable fact about graphene is therefore its very existance. Despite the theoretical concerns about its stability, the mechanical and structural properties of graphene have shown to be exceptional. Measurements of its elastic properties have revealed it to be one of the strongest materials ever measured, with a Young modulus of the order of terapascals [13].

The common belief that graphene should not be stable was based on the calculations of Landau and Peierls that state that long range crystalline order does not exist in two dimensions (See [14] and references therein. This is an example of the more general Mermin-Wagner theorem [15]) These authors showed that the in-plane thermal fluctuations of the atom positions diverged logarithmically with the size of the sample, making it unstable.

As the existance of graphene shows, the situation is of course more complicated. It is

also known from the theory of membranes [16] that if fluctuations in the third dimension are allowed, the coupling between bending (out of plane) and stretching (in plane) modes stabilizes a flat phase at low temperatures. This phase is flat only on average, but presents strong (but finite) fluctuations, so that the membrane presents ripples. This phase is not inconsistent with the Mermin-Wagner theorem because there is no long range order. The correlations in the atoms positions decay with the distance as a power law.

Of course, these results apply only for a free floating membrane. It is clear that the presence of the substrate in real samples plays a fundamental role in the structure of graphene due to their van der Waals interactions, and indeed several experiments [17–19] have shown that the morphology of graphene partially conforms to that of the substrate. But suspended membranes have also been produced, and electron diffraction experiments [20] have shown that suspended graphene is also not flat, presenting corrugations as well. Apart from thermal fluctuations and the presence of the substrate, a third origin for the curvature which has not been studied as thoroughly are topological lattice defects, which have also been observed in graphene [21, 22].

1.1.2 Electronic structure of graphene

Another aspect of graphene that attracts a lot of attention concerns its electronic properties. The electronic structure of the carbon atom is $1s^2 2s^2 2p^2$, so it has four orbitals in its outer shell. The different structures of carbon compounds can be understood in terms of the different hybridizations of these orbitals. In the case of graphene one s and two p orbitals hybridize into sp^2 orbitals, known as the σ orbitals, which then make covalent bonding with three other atoms, giving rise to graphene's honeycomb structure. The σ bonds are thus responsible for graphene's mechanical properties.

The remaining p_z orbitals, also known as π orbitals, give rise to the conduction and valence bands. The band structure of graphene was studied as early as 1947 by Wallace [9] in terms of a tight binding model, which was used as the building block to describe the band structure of graphite. The tight binding description of graphene has been discussed at length in the literature [7], so we only highlight its more relevant aspects. In the next chapter the tight binding method will be described in more detail.

The most important fact about the hexagonal lattice is that it has two atoms per unit cell, and it is therefore not a Bravais lattice. It can be subdivided in two Bravais lattices, which means that the Hamiltonian in k space will be described by two component wavefunctions, one for each sublattice.

The Hamiltonian as obtained from the tight binding model reads

$$H = \begin{pmatrix} 0 & \sum_i exp^{ik\delta_i} \\ \sum_i exp^{-ik\delta_i} & 0 \end{pmatrix}, \tag{1.1}$$

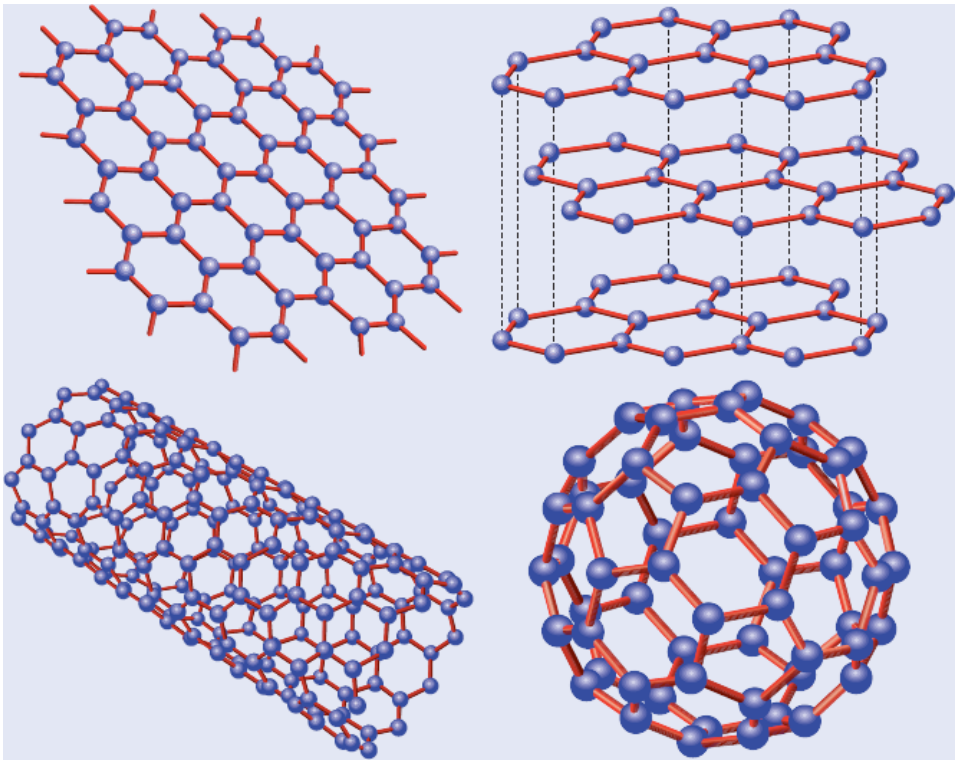

Figure 1.2: Different allotropes of carbon. Graphene (upper left), carbon nanotubes (lower left), graphite (upper right) and fullerenes (lower right). Image taken from [8]

where the three nearest neighbour vectors, shown in fig. 1.3, are

$$\delta_1 = \tfrac{a}{2}(-\sqrt{3}, -1) \quad \delta_2 = \tfrac{a}{2}(\sqrt{3}, -1) \quad \delta_3 = a(0, 1) \ . \tag{1.2}$$

From this Hamiltonian the band structure of graphene can be readily obtained:

$$E = \pm t \sqrt{3 + 2\cos(\sqrt{3}k_y a) + 4\cos\left(\frac{\sqrt{3}}{2}k_y a\right)\cos\left(\frac{3}{2}k_x a\right)}. \tag{1.3}$$

This band structure is depicted in fig. 1.4.

The first feature that makes graphene so different from other 2D materials is that, in its neutral state, the Fermi surface reduces to two Fermi points, also known as valleys, which can be taken to be $K_\pm = (\pm 4\pi/3\sqrt{3}, 0))$, as we can see in fig. 1.4. (We can see six different points, but in fact only two of them are inequivalent). Because of this it is sometimes refered to as a semimetal or a zero gap semiconductor. Expanding the Hamiltonian (1.1) around one of the Fermi points, we get the effective low energy Hamiltonian

$$H = v_F \begin{pmatrix} 0 & k_x + ik_y \\ k_x - ik_y & 0 \end{pmatrix}, \tag{1.4}$$

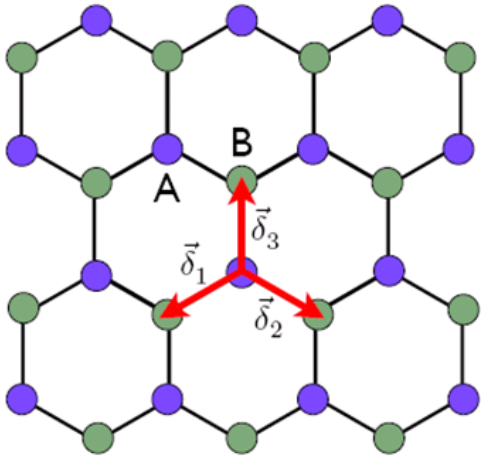

Figure 1.3: The hexagonal lattice of graphene. The two sublattices A and B are shown in different colours. The three nearest neighbour vectors (1.2) are also shown.

where

$$v_F = \frac{3ta}{2} \tag{1.5}$$

i.e. the low energy electronic excitations in graphene behave as massless Dirac fermions (in two spatial dimensions) where the Fermi velocity v_F plays the role of the velocity of light (the expansion around the other inequivalent valley gives another Dirac Hamiltonian related to this one by time reversal symmetry). This model does not depend on the particular derivation of the band structure, and follows from the symmetries of the hexagonal lattice [23, 24].The validity of this effective description in terms of Dirac fermions was confirmed in the first transport experiments in graphene by measuring the quantum Hall effect [25, 26]. The fact that the band is linear in momentum rather than parabolic has been observed explcitly in angle resolved photoemission spectroscopy (ARPES) experiments [27]. The Dirac fermion model has proven to be a very robust description for the low energy properties of graphene [7].

This is another of the main reasons that have made graphene so attractive, since the electronic properties of this system differ substantially from the conventional two-dimensional electron gas. The fact that the low energy electrons in graphene behave like chiral relativistic particles have lead to a number of exotic predictions, and moreover it represents a beautiful playground to discuss analogies with phenomena traditionally associated with high energy physics [28]. For example, chiral relativistic particles tunnel through potential barriers in an unconventional way known as Klein tunneling, and in particular tunnel with probability one at normal incidence, independently of the barrier height [29]. Another side of this effect is that the conservation of chirality implies the absence of backscattering, a relevant effect for the transport properties of the system. Another interesting analogy is that many types of disorder in graphene such as elastic strains or topological defects can be modeled in terms

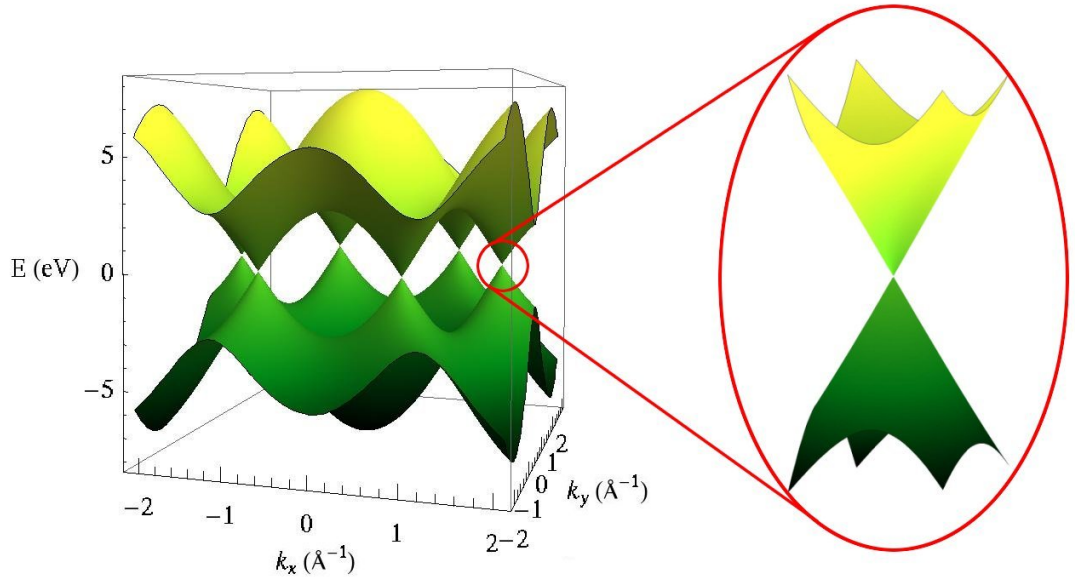

Figure 1.4: Band structure of graphene as obtained from (1.3). The conduction and valence bands touch at six points, only two of which are inequivalent.

of effective gauge fields [30], or as we will see in the works presented in this thesis, as Dirac fermions in curved space. The localization behaviour of Dirac electrons in random potentials is also very different form those of Schroedinger electrons, as they belong to a different symmetry class in the classification of random matrix theory [31].

More insight into the peculiar behaviour of Dirac fermions can be obtained by computing their electronic density of states, which is:

$$\rho(E) = \frac{|E|}{2\pi v_F^2} \tag{1.6}$$

per valley and spin, in contrast to the 2DEG where the DOS is constant with the energy. This in particular implies that the density of states at the Fermi level vanishses. A very interesting implication of this fact is that screening is very poor, and the Coulomb interactions remain truly long ranged. This is another unique fact of systems with Dirac points, which is very relevant for the many-body effects produced by electron-electron interactions. These many body effects represent another interesting face of graphene, especially since the recently reported fractional quantum Hall effect [32, 33]. In this thesis we are going to study the interaction effects in graphene and the way in which they affect observable quantities.

The vanishing density of states at the Fermi level also leads to the poor screening of external potentials to which the real sample of graphene may be subjected, in particular those produced by charged impurities. The unconventional screening of Coulomb impurities

in graphene has recieved much attention [34–37], and as we will see, it is a very important matter for the transport properties of the system. We will also study the influence of Coulomb impurities in graphene in this thesis.

Despite having zero density of states at the Fermi level, the early experiments already showed that graphene presents a finite DC conductivity [25, 26]. Although a finite value was expected from early calculations [38], the precise value found in experiments was different, and the discussion about what this value should be has generated a lot of activity [39, 31, 40–42].

From the electronic point of view, it is another interesting fact that graphene can be gated and shows a strong field effect, so the number of carriers can be modified substantially in an easy way [10]. This ability to control directly the carrier density is very important to study the transport properties of graphene, especially from the point of view of applications, and the doped graphene system has also been studied extensively.

At finite doping, graphene shows metallic behaviour, with a very high mobility which varies little with temperature. The first experiments in graphene on SiO_2 reported room temperature mobilities of 15.000 $cm^2\ V^{-1}\ s^{-1}$ [26], but by now samples of turbostratic (multilayer) graphene have been shown to reach up to 250.000 $cm^2\ V^{-1}\ s^{-1}$ [43] at room temperature. This is another remarkable fact. These mobilities are higher than those of any known semiconductor (in ambient conditions), so this makes graphene a very good candidate for electronic applications [1].

The question of what is the specific mechanism that limits the electronic mobility in graphene samples is therefore of vital importance and the answer is still debated [44]. Several proposed scattering mechanisms are related to the effects of morphology in the electronic properties, for example, the corrugations of the samples, topological defects, or resonant scatterers such as vacancies. The other main candidate is scattering by random charged impurities from the substrate. In this thesis we are going to study the effects on the electronic properties of both the morphology and the charged impurities.

Another very interesting aspect of the physics of graphene are its magnetic properties. Ferromagnetic order has been observed in bulk graphite samples [45] and shown to be intrinsic to carbon [46]. Signatures of magnetism have also been observed recently in graphene [47].

The mechanism behind magnetism in graphene is known to be related to the presence of vacancies and edges, and has been widely studied [48–52]. However, the influence of topological defects on magnetism remains unexplored, despite the experimental evidence of their presence [21, 22], and this topic will also be addressed in this thesis.

1.2 Organization of the thesis

After this introduction to the physics of graphene, we now summarize the work to be presented in this thesis. We are going to study several problems in graphene that have been introduced in the previous section. The thesis has been structured into two main parts.

In the first part, we will study the role of morphology in the electronic properties of graphene. As we have seen, several experiments have shown the presence of both smooth corrugations and topological defects in graphene samples, and their effects are important for the transport properties of the system.

The role of morphology has been studied under two complementary perspectives. First, in chapter 2, the effects of toplogical defects have been evaluated by means of lattice models. By means of a tight binding method in real space, we have studied how the presence of defects such as dislocations and Stone-Wales defects alter the local electronic structure around them. We show how these defects produce strong modifications in the local density of states. Then we have added the effects of interactions through a Hubbard term to the model to explore the influence of defects in the magnetic properties. These are shown to depend crucially on the bipartite nature of the lattice, and topological defects which break it such as dislocations or reconstructed vacancies are shown to produce a transition between different ground states with the Hubbard interaction U.

Then, in chapter 3, both smooth corrugations and topological defects are studied from an alternative perspective. We have seen that Dirac fermions in graphene are a robust feature which can be traced back to the symmetries of the lattice. This leads us to propose to use continuum geometric models based on the Dirac equation in curved space to model the effects of curvature. First a smooth curved gaussian bump is presented as an example of the formalism. It is shown that the bump produces local changes in the density of states which correlate with the region spanned by the bump. Then we also show how the geometric model can be extended to include the presence of dislocations by considering a space with torsion, and discuss the possible application of this model to related systems.

The second part of the thesis is concerned with the problem of long ranged interactions in graphene. As we have seen, the vanishing density of states at the Fermi level in graphene implies that screening is poor. Moreover, we also discussed that Coulomb impurities are considered to be one of the main scattering mechanisms affecting the conductivity of the system. In Chapter 4 we have studied the spectral properties of doped graphene in the presence of random Coulomb impurities. By solving a Self-consistent Born Approximation numerically, we have computed the electron lifetime, the density of states and the spectral function of the system. We summarize how these properties are measured in experiments and discuss the relevance of our results, and compare them with other approaches. We also discuss the applicability of this model to the low doping region.

In chapter 5, we have addressed the effects of electron-electron interactions in graphene.

This problem has been treated before in a number of studies, most of which were related to renormalization. However, the problem of calculation of physical observables in the renormalized theory has not been addressed systematically. In this chapter we show how observables are computed in renormalized perturbation theory, following the analogy with the case of QED in high energy physics. In the case of graphene, the only parameter that renormalizes is the Fermi velocity v. We discuss possible experiments to measure it, as well as different renormalization conditions. We also show how the computation of response functions is carried out in this scheme, and discuss as an example the interaction corrections to the optical conductivity.

Finally, in chapter 6, we present and discuss the main conclusions of the thesis and open problems. Part of the work discussed in this thesis has been published in the articles listed before the introduction.

2 Topological defects in graphene: The lattice perspective

In the following two chapters we will discuss how the morphology influences the electronic properties of graphene. In this first chapter, we will focus on the role of topological defects, described from the point of view of models formulated in the lattice. We will first address the local electronic structure of graphene with defects with a tight binding model, and then we will proceed to add interactions in the form of a Hubbard model to see how the magnetic properties of the system are affected by the presence of defects.

The next chapter will address the influence of morphology on the electronic properties from the complementary approach of continuum models, and it will cover both topological defects and smooth corrugations.

2.1 Introduction: Topological defects

Defects in crystals have been studied extensively in solid state physics, for they are important for both the electronic and the mechanical properties. A crystalline defect can be defined very generally as a small region in the crystal where the regularity of the lattice has been drastically altered. For example, there may be missing or extra atoms of the same type of those which conform the crystal (called vacancies and intersticial atoms), or of a different type (just called impurities), or we may find a small region where the arrangement of the atoms is just different from that of the perfect lattice, i. e. where the coordination of the atoms is altered.

The idea of a topological defect is a broader concept that applies to a variety of ordered systems, crystals being one example of them [53]. Loosely speaking, a defect in an ordered medium is called topological when, in spite of looking like a local defect (i. e. the surroundings look perfectly ordered), a global operation that involves sections far away from the defect is needed to remove it. A usual way of identifying topological defects is through the effect that they have on integrals of quantities related to the order parameter along a contour that encloses the defect. These integrals are independent of the actual contour, and different from the case where the defect is not there, no matter how far we deform the contour [1].

[1] Although in crystals the term topological usually refers to this meaning, defects are sometimes also called topological in a broader sense just because the coordination of the atoms (the "topology" of the lattice)

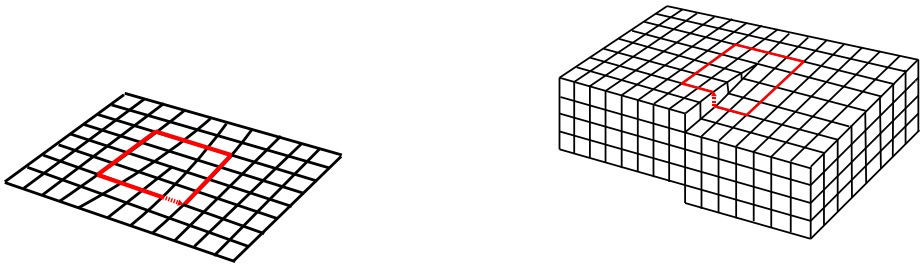

Figure 2.1: Left: Edge dislocation in a square two-dimensional lattice. The Burgers vector is parallel to the displacement. Right: Screw dislocation in a three dimensional cubic lattice. The Burgers vector is perpendicular to the displacement.

In crystals, topological defects can be classified into two kinds: Dislocations and disclinations [54]. Dislocations can be thought of being formed by performing a cut in a bulk material, and glueing together the faces produced in a different relative position, adding or removing rows atoms if necessary, see fig. 2.1. This process leaves a defect at the end of the cut that can be identified by adding discretely the vectors that join the atoms in a closed circuit enclosing the defect. Without the defect this is always zero. In the presence of a dislocation this quantity, called the Burgers vector, is non-zero and independent of the closed path chosen. This is the defining quantity of a dislocation. If the Burgers vector is paralell to the plane defined by the contour, the defect is called an edge dislocation, and if it is perpendicular to this plane, it is called a screw dislocation. These two types of defects are shown in fig. 2.1 for the case of a square lattice.

A disclination is similarly formed by adding a wedge of atoms, and it can be identified by computing the total angle subtended by a closed path enclosing the defect, called the Frank angle. In the case of a discrete crystal lattice, the Frank angle must be discrete to obtain a regular "glueing" of the cutted edges. This process of forming defects by cutting and glueing is known as Volterra construction. Note that a disclination dipole (two disclinations close to each other with opposite Frank angle) can also be seen as a dislocation.

In the particular case of the hexagonal lattice, disclinations can be formed introducing wedges of multiples of 60^{o}. This means that a hexagon in the lattice turns into another polygon, the most usual being heptagons and pentagons.

In dislocations, the addition of an extra row forms a heptagon-pentagon pair (known as a glide dislocation), according to the disclination dipole idea from the last paragraph, or an octagon with a dangling bond, (known as a shuffle dislocation) [54]. These types of defects

changes. Throughout this chapter, this difference will not matter and we will use the term in the broader sense. In the next chapter however, the true topological nature of defects will be relevant and the distinction will matter.

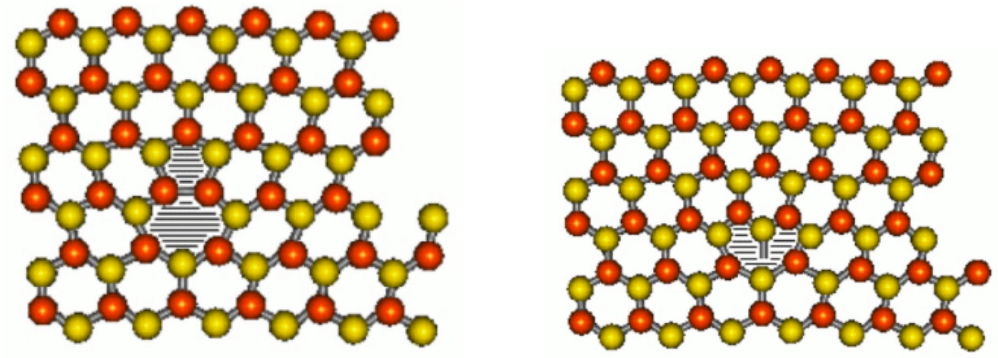

Figure 2.2: Structure of the glide (left) and shuffle (right) dislocations in the planar graphene lattice.

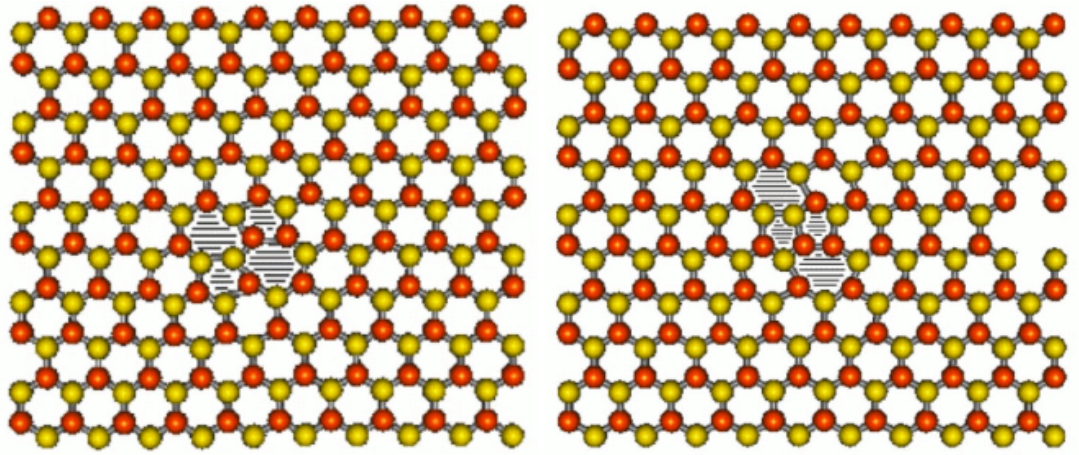

Figure 2.3: Left: Lattice structure of a Stone Wales defect. Right: Same for the dislocation dipole described in the text.

are shown in fig. 2.2. More complicated defects in the hexagonal lattice include dislocation dipoles (two heptagon-pentagon pairs), which can be joined together by the heptagons or the pentagons, and they are shown in fig. 2.3. In the first case, this is known as a Stone-Wales (SW) defect [55], and in the second case, as an inverse SW defect [56].

All these defects were very well known in the literature before the synthesis of graphene because they are present in carbon nanotubes and fullerenes, where they have been widely studied [57, 58]. The curvature of the C_{60} fullerene and other closed structures is indeed produced by pentagonal defects [59, 60], and more complex carbon nanotube structures such as caps, elbows and nanotube junctions [61, 62] also require the presence of pentagons and heptagons. These defects have also been considered theoretically as the building blocks of new carbon allotropes [63, 64, 56, 65].

Dislocations and SW defects in graphene have been studied in [66] from the point of view of elasticity theory. Glide and shuffle dislocations have been shown to be dynamically stable.

The SW defect was found to be unstable: its component edge dislocations glide towards each other and annihilate, leaving the undistorted lattice as the final configuration, contrary to the inverse SW, which was found to be stable.

In the case of graphene, several experiments have observed the presence of defects of this kind. Dislocations have been observed by Transmission Electron Microscopy (TEM) after electron irradiation [22] (see fig. 2.4), as well by Scanning Tunneling Microscopy (STM) on graphene grown on Ir [67]. Isolated disclinations have also been reported in STM experiments [21]. More complicated combinations of heptagons and pentagons have also been observed to form spontaneously with TEM [68], relaxing to the undistorted lattice after a few seconds (see also fig. 2.5). The octagon defect (shuffle dislocation) has been recently observed in TEM as well [69].

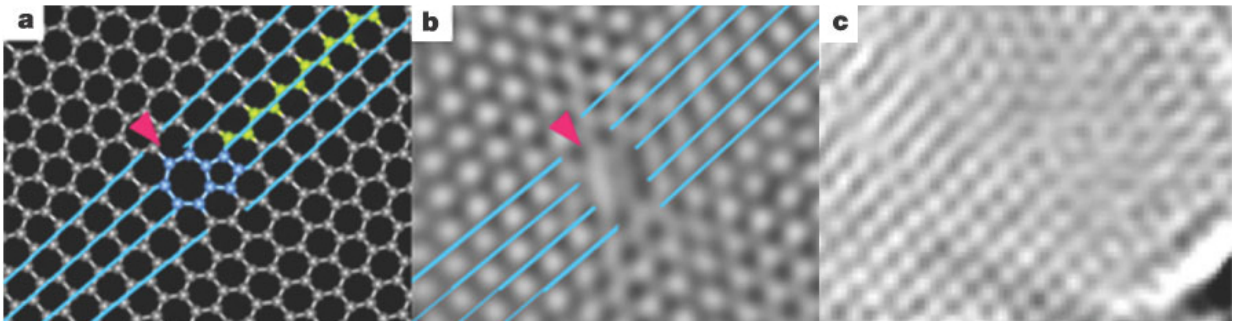

Figure 2.4: Observation of a dislocation in single layer graphene induced by electron irradiation. a) Ideal model of the dislocation. b) Simulation of the corresponding TEM image. c) Actual TEM image. (Images adapted from [22])

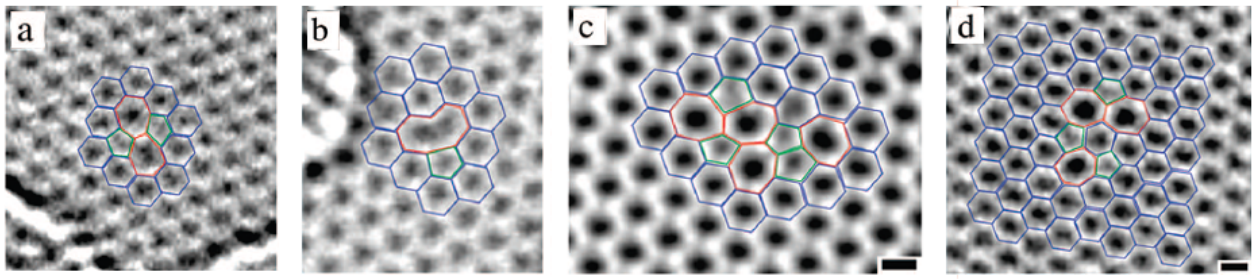

Figure 2.5: TEM images of various metastable defects in graphene. a) Stone-Wales defect. b) Reconstructed vacancy. c-d) More complex heptagon-pentagon defects. (Images adapted from [68])

In summary, both theoretical and experimental findings support the idea that topological

defects are present in graphene samples, and therefore they should be taken into account when evaluating the electronic properties. In this chapter, we address the computation of such properties with lattice methods. The corresponding discussion from the continuum point of view will be presented in the next chapter.

2.2 The tight binding method

A natural starting point to describe the electronic properties of solids is to evaluate their bare band structure. Neglecting all interactions reduces the problem to that of diagonalizing the one-particle Schroedinger Hamiltonian of an electron in the potential of the lattice, something that can be done with various degrees of accuracy with different strategies. A discussion on this problem can be found in almost all solid state physics books, for example [70, 71].

A first class of approaches, for example, assume that the lattice potential is weak, so that pertubation theory based on free electron eigenstates is a realiable description. However, this is not the case for many materials, including carbon. Much more sensible results can be obtained in these cases by considering the opposite limit, in which electrons are tightly bound to the lattice atoms, so atomic orbitals are used as the reference states for perturbation theory. The simplest of these methods is thus known as the tight binding (TB) method, or the linear oombination of atomic orbitals (LCAO) method.

Since it is a very standard procedure, we will just quote the main result of this method, and we refer to the mentioned books for a derivation. If the wavefunction is expressed in terms of atomic orbitals $\phi(\vec{r})$ (assuming only one orbital per atom) as

$$\Psi(\vec{r}) = \sum_i c_i \phi(\vec{r} - \vec{R}_i), \tag{2.1}$$

and the overlap factors between different sites are neglected, the Schroedinger equation for the electrons can be expressed with a matrix Hamiltonian as

$$H_{ij} c_j = E c_i, \tag{2.2}$$

where

$$H_{ij} = \int d^3 r \phi(\vec{r} - \vec{R}_i) U(r) \phi(\vec{r} - \vec{R}_j), \tag{2.3}$$

and $U(r)$ is the lattice potential. Since all atoms in the lattice are equal, there are only a few different values that H_{ij} can take. When $i = j$ this value is called the on-site energy β, and when i and j are nearest neighbours this is the nearest neighbour hopping integral t. It is usually assumed that atomic orbitals do not spread much away from their atoms, so that the integral in (2.3) is assumed to vanish if i and j are further neighbours.

The power of this method is that the hopping integrals need not be computed from first principles, but can be measured to fit the band structure. For the case of graphene, several

comparisons of the tight binding method with more elaborate *ab initio* computations [72, 73] have shown that it is a good approximation, especially for the low energy properties. The approximate value of the nearest neighbour hopping in graphene is $t \sim 2.7$ eV.

This Hamiltonian has a simple solution when the lattice is infinite and perfectly periodic, so that the eigenstates are given by Bloch's theorem. In this case, a discrete Fourier transform diagonalizes the "spatial part", and the problem reduces to the diagonalization of a small matrix, whose size is determined by the number of orbitals contained in the unit cell (The product of the number of atoms per unit cell times the number of orbitals per atom, assumed to be one in this chapter). This was shown in the introduction for the case of graphene, where the peculiarity of having two atoms per unit cell in the Bravais lattice gives a 2x2 matrix which reduces to the Dirac Hamiltonian around the K points.

Discrete translational symmetry simplifies the calculations in practice, but the tight binding method retains almost its full power even if this symmetry is not present. Even if a discrete Fourier transform is meaningless, the method can still be used in real space. The only limitation is that finite size systems have to be considered, since in absence of Bloch's theorem, the size of the matrix to diagonalize is now the total number of atoms.

With modern computers, exact diagonalization can be performed in reasonable times for systems with thousands of atoms, which still makes this method useful to discuss physical systems. And while a system may be too large for our numerical capabilities, we may be interested in the local electronic properties only around a particular place, for example if it is the only one where the lattice deviates from its periodic structure.

We are going to focus on this problem for the case of graphene. In particular, we are interested in the local electronic structure of the electron states near topological defects, such as dislocations. For this purpose, it is enough to consider one of such defects in the center of an otherwise hexagonal lattice, and in this case the exact diagonalization can be performed easily.

2.2.1 Electronic structure of dislocations

As mentioned in the introduction to the subject, topological defects have been found in graphene samples, and they should affect the electronic properties. In this section we will evaluate the local density of states in a honeycomb lattice with a dislocation (both glide and shuffle types) using the tight binding method described previously.

As discussed before, dislocations can be seen as formed by adding or removing a row of atoms to the lattice. Therefore, the presence of a single dislocation prevents the use of periodic boundary conditions. (Periodic boundary conditions in the real space tight binding method are implemented by adding hopping terms t linking the corresponding sites in the boundaries). Therefore, for this case, we will use open boundary conditions. This is an important fact to stress, because it is known that zero modes appear associated to the edges

in graphene, which should not be atributed to the presence of the topological defects we are studying.

An option to avoid edge states is to consider two dislocations, so that the added row of atoms starts in one of them and ends in the other. In this case the boundaries are still regular, and periodic boundary conditions can be used. This will be the scheme used in the next section when computing the magnetic properties of the system.

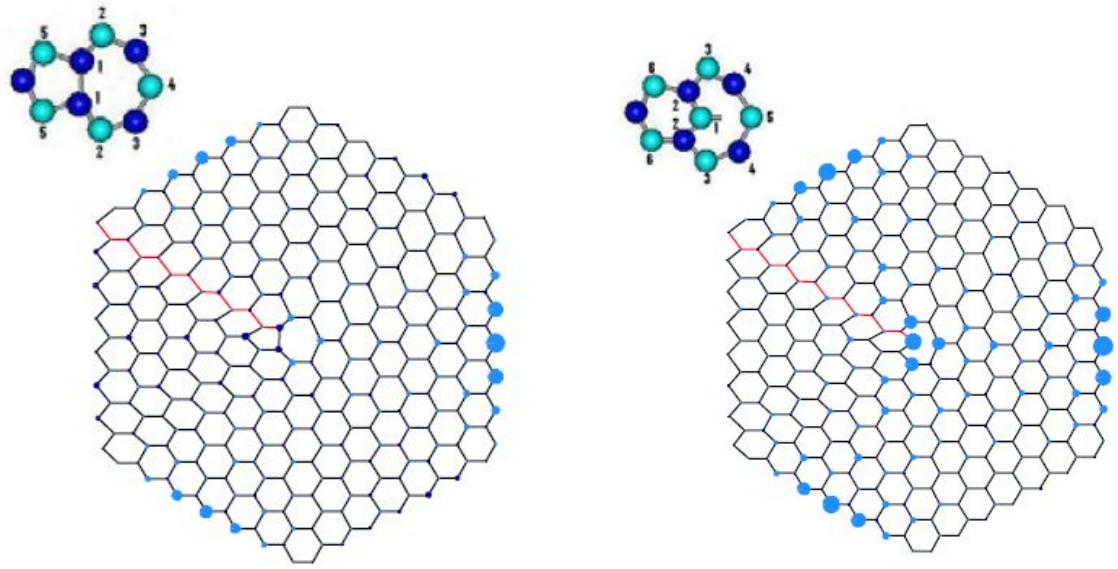

Figure 2.6: Left: Lattice structure and charge density for a low energy eigenstate in the presence of a glide dislocation shown in the inset. Right: Same for the shuffle dislocation.

fig. 2.6 shows the configuration of the lattice for the dislocations depicted in the inset where the atoms that constitute the defect are numbered. The extra rows of atoms characteristic of these edge dislocations are shown in red. The area of the circles is proportional to the squared wavefunction for one of the lowest energy eigenvalues. Notice that, as mentioned before, the wavefunction is noticeably large in the edges, a fact which is not to be attributed to the dislocations.

In fig. 2.7, we show the LDOS for the five sites around the defect numbered in the inset of fig. 2.6 and for an extra site located at a certain distance from the defect. The LDOS is drastically distorted at the defects but rapidly recovers the normal shape away from the center of the defect. The pentagon heptagon pair (glide dislocation) breaks the electron hole symmetry of the system, and this is reflected in the asymmetry of the LDOS. The LDOS at zero energy is not zero, but it has a minimum in all the cases. The sixth graph shows the LDOS at an atom located six lattice units apart from the defect. This is the distance at which the influence of the dislocation ceases to be noticeable.

The shuffle dislocation has a more pronounced effect on the LDOS. As it can be seen in

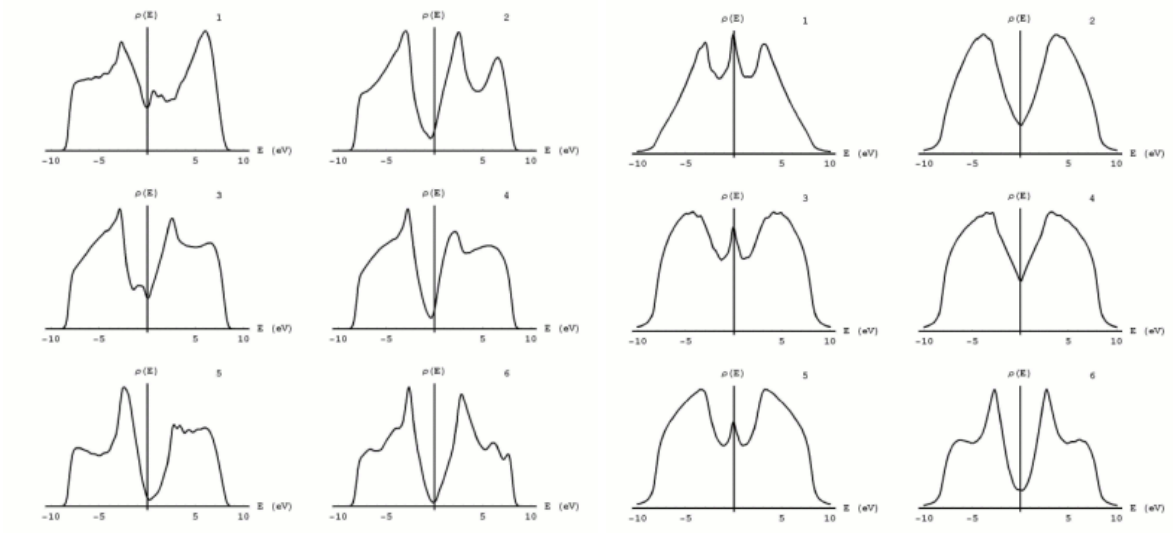

Figure 2.7: Left: for the graphene sample with a glide dislocation depicted in fig. 2.6, LDOS at the numbered sites around the defect shown in the inset of fig. 2.6. Right: same for the sample with a shuffle dislocation.

fig. 2.7, at zero energy there appear sharp peaks at the position of the dangling bond atom and at neighboring sites of the same sublattice whereas dips in the LDOS appear at the sites of the opposite sublattice. The distortion in the LDOS decays faster with the distance in the case of a shuffle dislocation than in the case of a heptagon-pentagon pair. The right panel of fig. 2.7 shows that the DOS of the perfect lattice is already recovered at position 6 of the inset in fig. 2.6, one lattice distance away from the defect. The mid gap state induced by the defect is strongly peaked at the defect position, similarly to what happens with the zigzag edges states. This type of dislocation does not break the electron-hole symmetry of the lattice.

The electronic structure of the two dislocation dipoles described in the introduction (SW and inverse SW defects) is shown in figs. 2.8 and 2.9. These dipole defects induce a stronger local distortion of the charge density than single dislocations. The states close to zero energy present some accumulation of charge near the defects, but the normal LDOS is rapidly recovered as we move away from the defects.

2.3 Magnetic properties

In the introduction of this chapter, we have explained that neglecting interactions is only a starting point towards the description of electronic systems. Interactions *do* play a role in these systems, and sometimes the puzzle is actually to explain why in some situations the non-interacting picture is nevertheless approximately correct.

Magnetism is a physical property that is directly related to interactions. In this section

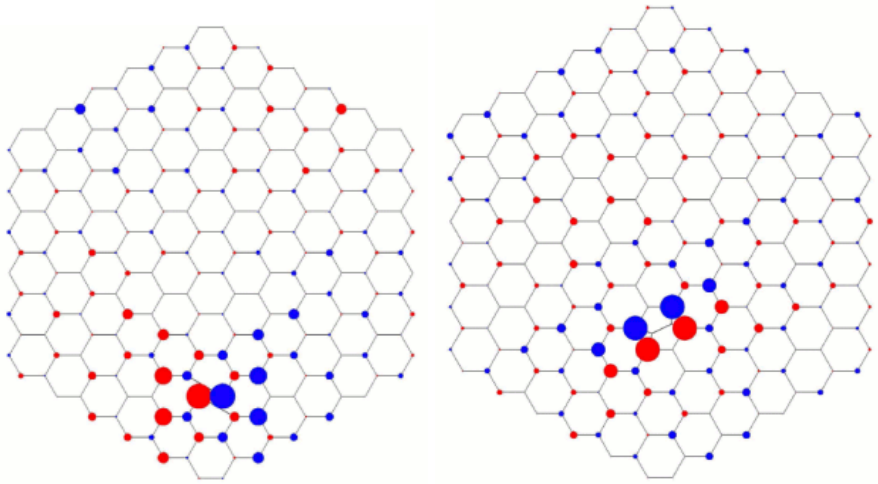

Figure 2.8: Left: Lattice structure and charge density for the fourth positive-energy eigenstate in the presence of a Stone Wales defect. Right: Same for the dislocation dipole described in the text.

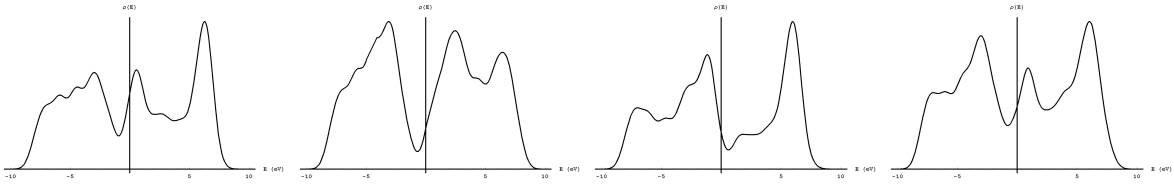

Figure 2.9: From left to right: Local density of states of a real SW defect at the site shared by the two adjacent pentagons and at its nearest neighbor. LDOS of the dislocation dipole discussed in the text at the site shared by the two heptagons and at its nearest neighbor.

we will discuss the experimental evidence pointing to intrinsic magnetism in graphene, and how interactions can be included in the tight binding model through a Hubbard interaction to model the magnetic properties of the samples. As we will see, the Hubbard model picture has provided an intuitive way of understanding magnetism in bipartite lattices thanks to Lieb's theorem. However, topological defects make the lattice non bipartite, and the aim of the section is to show, by means of a Hubbard model in a lattice with these defects, that their presence may drastically alter the magnetic properties.

As we mentioned in the introduction, several experiments have reported the observation of ferromagnetism in carbon-based compounds. Ferromagnetic order enhanced by proton irradiation has been observed in graphite samples [45] and demonstrated to be due to the carbon atoms by dichroism experiments [46]. Ferromagnetism has also been reported in carbon nanotubes induced by magnetic impurities [74] and in honeycomb lattice arranges of first row elements [75]. Signatures of magnetism have also been observed recently in graphene [47].

The mechanism leading to ferromagnetism in carbon structures is well known. In the presence of defects that change the coordination of the carbon atoms, such as vacancies, cracks, or edges, spin polarized states are generated in the region of defects, with energies close to the Fermi level [76]. Defects and edges are therefore crucial to explain the magnetic properties. This mechanism can be understood intuitively, as we said, with a Hubbard model for the honeycomb lattice, which we now introduce.

The Hubbard model [77] is probably the simplest way to add the effects of electron-electron interactions to systems whose bare band structure is well described by a tight binding model (see [71] for an introduction). The model assumes that the Coulomb interaction is totally screened, and it can be represented by an on-site repulsion term of strength U. The Hamiltonian for the model reads:

$$H = -t \sum_{<ij>,\sigma} c_i^+ c_j + U \sum_i n_{i\uparrow} n_{i\downarrow}, \tag{2.4}$$

where $< ij >$ stands for nearest neighbors of the honeycomb lattice and σ for the spin degree of freedom. The Hubbard model was first introduced to study the effects of correlations in narrow band metals, but since then it has been used for many other systems. Its success relies on the fact that, while it may look like an oversimplified model, it correctly accounts for the qualitative physical properties, such as the transition to a Mott insulating state.

In the case of ideal graphene, the applicability of the Hubbard model requires further discussion. As we mentioned in the introductory chapter, the density of states of graphene at half-filling vanishes, and therefore Coulomb interactions remain long ranged. Replacing this long range interaction by the Hubbard term, with which electrons see each other only in the same site, would not seem to be a sensible approximation.

However, the systems that we are going to describe contain vacancies and defects, and it is well known that these generate zero modes [78, 79], i.e. a finite density of states at the Fermi level. This resonance in the density of states due to vacancies has been recently observed [80]. This density of states provides the necessary screening to justify the validity of the Hubbard model. Furthermore, it is reassuring that results obtained with more complicated Density Functional calculations are often in agreement with those obtained from a Hubbard model [72].

An approximate value of the Hubbard coupling U in graphene can be estimated in several ways from first principles calculations. The values obtained usually lie in the range $U/t \approx 1-2$ [72, 81], but higher values have also been quoted [7].

As we have seen in the introduction, graphene is an example of a bipartite lattice, i.e. a lattice consisting on two different sublattices A and B where atoms of A are only linked to B and viceversa. Concerning the ground state of a Hubbard model in such a lattice, E. Lieb [82] proved a very useful theorem stating that for a repulsive value of the Hubbard interaction U the ground state of the half filled lattice is non degenerate and has a total spin equal to half

the number of unbalanced atoms: $2S = N_A - N_B$. This rule has been confirmed recently in a number of studies of graphene with vacancies, edges or larger defects [48–52] and in the case of bilayer graphene [83, 84], and the Lieb theorem has become a paradigm of magnetic studies in graphene clusters and in nanographite.

What is more interesting, the rule seems to survive when more complicated *ab initio* calculations based on different variants of Density Functional Theory (DFT) are performed [85–87]. The purpose of this section is to emphasize the fact that the crucial property that determines the magnetic behavior of the lattice is its bipartite nature, as it was already established in the original paper [82]. Vacancies, islands, cracks or whatever defects preserving this property have been shown to follow the prediction of Lieb's theorem, but what happens with topological defects? As we have seen in the previous section, both heptagons and pentagons break the sublattice symmetry by joining two atoms of the same lattice. We will show that even a slight frustration of the bipartite nature of the lattice such as this is enough to alter Lieb's rule. Since, as we have seen in the previous section, topological defects in graphene are very likely to be present in any sample, it is important to evaluate the effects that they produce.

The purpose of this chapter is to study the mean-field solutions of the Hubbard Hamiltonian for graphene in the presence of defects that make the lattice non-bipartite. We will first study the simple case of a vacancy in which two of its adjacent atoms have been joined by a link. This example allows to see very clearly the influence of the link between atoms of the same sublattice in the zero modes. After that, we will study the more complicated, but also more realistic case of a dislocation.

2.3.1 Lieb's theorem

In order to get some insight into what can happen when the sublattice symmetry is broken by defects, we will heuristically discuss Lieb's theorem, along the lines of the original paper's remarks. The actual proof of the theorem is rather complicated, however, but one can get an intuitive understanding with simple arguments, and that is what we will do here.

Consider a tight binding Hamiltonian in a bipartite lattice (and for the moment $U = 0$). This means that there are an abitrary number of atoms N_A in sublattice A, and N_B in sublattice B, with the only restriction that any atom has hopping elements only to the atoms of the other sublattice. The Hamiltonian matrix of this system can be written as

$$H = \begin{pmatrix} 0_{N_A \times N_A} & h_{N_B \times N_A} \\ h^{\dagger}_{N_A \times N_B} & 0_{N_B \times N_B} \end{pmatrix}. \tag{2.5}$$

We immediately see that the number of independent rows of this matrix is at most $2N_A$, this is, the rank of H is $2N_A$. Let's assume without loss of generality that $A > B$. Since the dimension of H is $N_A + N_B$, this implies there are $N_A - N_B$ zero eigenvalues. Moreover, it's also not difficult to see that the rest of eigenvalues must come in $\pm$ pairs.

To find the total spin of the ground state, we just fill electronic states up to half filling. $2N_A$ electrons fill the negative energy eigenstates in pairs of opposite spins, and we are left with $N_A - N_B$ electrons to distribute in $N_A - N_B$ zero modes (each of which admits two electrons, with spins up and down, respectively). We then see that degenerate ground states with different total spin are possible, depending on how we distribute the electrons. The most that can be said is that a state with total spin $2S = N_A - N_B$ does exist among all the possible ground states.

On the other hand, now consider the case where $U >> t$. It is not difficult to see that in this case the model behaves as a Heisenberg antiferromagnet. If t were strictly zero, then we would just have a totally polarized lattice where each spin can point in an arbitrary direction. The addition of a small t can be seen to generate, in perturbation theory, the Heisenberg antiferromagnetic coupling. The total spin of this system in the ground state is necesarily $2S = N_A - N_B$.

We still don't know what happens in the general case, but it can be argued by a continuity argument that the total spin remains $2S = N_A - N_B$ all the way down to $U = 0$. There the ground state is degenerate, but among the different ground states at least there is one with spin $2S = N_A - N_B$. This is of course not the proof of Lieb's theorem, which can be found in the original reference [82], but it is the key point that will allow us to discuss topological defects in the next section.

2.3.2 Introducing a pentagon

The previous intuitive argument makes it easier to see what happens when we modify the bipartite nature of the lattice (note that in this case Lieb's theorem has nothing to say, since the main hypothesis doesn't hold now). We will do so by performing the seemingly inocuous modfification of linking two atoms from the same sublattice from those atoms left with coordination two around a vacancy. This configuration has been observed to form naturally as the first step of vacancy reconstruction [88, 89] and has also been shown to lower the energy in density functional studies of vacancies [90].

We can see rather generally that, in the case of $U >> t$, this modification is indeed inocuous. The antiferromagnet would not be perfect in this case, but the ground state would still have the same spin (with a different energy), because we just have to add up and down spins, and these are the same.

But what happens in the $U = 0$ limit? Since the degeneracy of the zero modes was what guaranteed that the maximun spin state existed among the ground states, and the zero modes due to the vacancies do not exist any more, the continuity argument may not hold now. In this simple case of just one vacancy and a pentagon, we note that the number of electrons is odd, so if there is no degeneracy at the Fermi energy, the spin will be one, because there is no partner to fill its level. But if we go to the more interesting case of two

vacancies of the same sublattice, with now an even number of electrons, and close one of them to form a pentagon, we will lose a zero mode, (and in general electron hole symmetry) and the state with maximum spin will not exist. We realize that if there is no state with the appropiate total spin at $U = 0$, then at some threshold U_c there must be a transition to a different state. The continuity argument doesn't hold anymore.

Now we will see all this at work in Hubbard's model by solving it in some specific cases.

2.3.3 Results: Mean field calculation

Partially reconstructed vacancies

After the introductory discussion of the last section, we now solve explicitly the Hubbard Hamiltonian in a mean field approximation. We begin by studying configurations of two vacancies belonging to the same sublattice in a graphene sheet where in one of them two of the sites of coordination two have been joined by a link forming a pentagon as described in the previous section, and shown in fig. 2.10. This is the simplest situation to exemplify the behavior that we want to emphasize.

fig. 2.10 shows the ground state configurations for a value of the Hubbard repulsion U=1 (throughout the chapter U will be measured in units of the hopping parameter t), for both the pentagonal defect and the vacancy. The total spin of the ground state in the standard configuration shown in the left side of the figure is $S_z = 1$, what accounts for half the two impaired atoms of the same sublattice. The polarization for each site of the lattice is represented by an arrow (its scale in units of $\hbar$ is also shown adjacent to each figure). We see a relatively strong polarization localized at the atoms surrounding the vacancy as expected. In the right hand side of fig. 2.10 a vacancy and the discussed pentagonal defect are shown. This little frustration of the sublattice order is enough to destroy the polarization around the two vacancies and the total spin of the ground state changes to zero.

The structure presented in the figure corresponds to a density of defects, vacancies in this case, of one percent, which is large. We have performed the calculation with various defect densities from 0.1 to 10^{-3} and the results remain the same independent not only of the density of defects but of the relative distances among them. We have also computed the case in which both vacancies have a pentagonal link and the results are the same: in the presence of at least a pentagonal ring there is a critical value of U of approximately $U \sim 2$ above which the spin of the ground state recovers the full value $S_z = 1$. This is in agreement with what has been explained in the previous section.

To better appreciate the effect of the pentagonal link we note that the critical U to polarize the ground state for vacancies in the bipartite lattice is zero if the density of vacancies is not too big. In the non-frustrated case there is also a transition from an unpolarized semimetal with magnetic moments strongly localized at the positions of the uncoordinated atoms surrounding the vacancy to a perfectly ordered anti-ferromagnetic state with two -frozen- holes

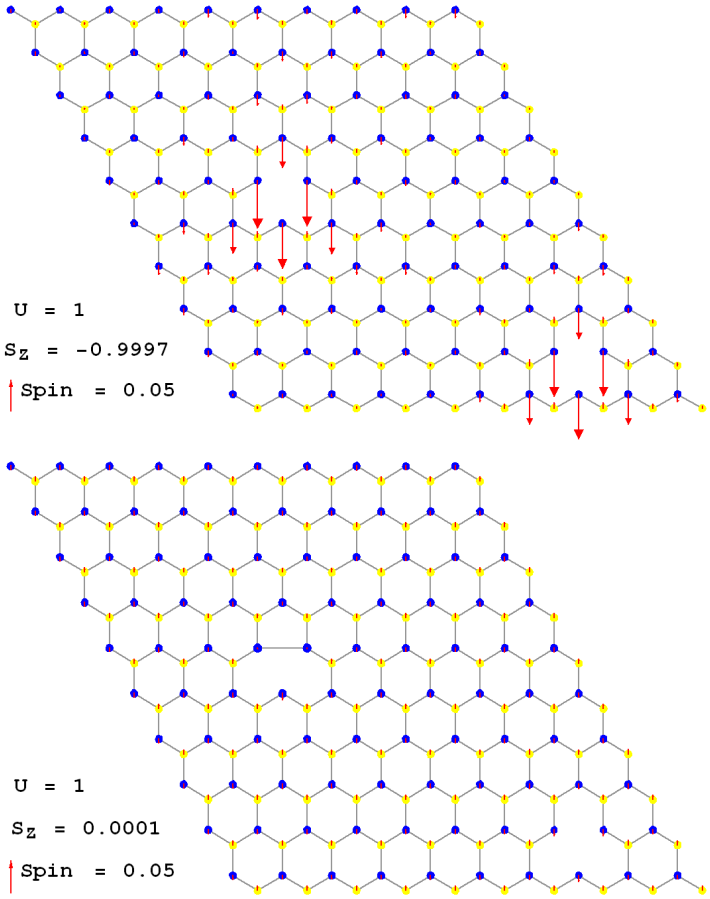

Figure 2.10: Ground state of the system with two vacancies (left) and the pentagonal vacancy discussed in the text. The circles represent the charge in the atoms and the arrows represent the spin. It can be seen how a single link connecting atoms of the same sublattice changes the ground state as discussed in the text.

and with total spin determined by the unpaired electrons. The low U configuration has been described by Lieb in the original paper as an example of itinerant ferromagnetism, and the high U case as ferrimagnetism, where there is a perfect antiferromagnetic order in a system with a non zero total spin. It is quite remarkable that the presence of a single link frustrating the sublattice symmetry in a cluster or up to 3200 atoms is enough to rise the critical U to the rather high value of $U = 2$. As noted before, the critical value found in this case is similar to the one that sets the semimetal to antiferromagnetic insulator transition in the perfect system.

Dislocations

Next we turn to the more interesting case of having dislocations in the lattice. As explained in the introduction, this is a more realistic situation, since dislocations are to be expected in

real samples. The presence of dislocations can affect the magnetic properties of the graphene samples in two ways: Shuffle dislocations can nucleate local magnetic moments similar to the ones induced by vacancies while the structure of the glide dislocations frustrate the bipartite nature of the lattice.

In order to eliminate the influence of the edges and perform the calculation with periodic boundary conditions we introduce a pair of dislocations such that the extra row begins in one and ends in the other one. fig. 2.11 shows the basic structure discussed in this work. The shuffle dislocation is made of an octagon with an unpaired atom of a given sublattice. The dislocation line ends in a glide dislocation made of a pentagon-heptagon pair. This basic block does not alter the edges of the sample and should behave like a single vacancy.

We have checked that indeed the total spin of the lattice for this configuration is S=1/2 for a critical value of $U \sim 0$ showing that the dangling bond of the shuffle dislocation behaves as a vacancy of the other sublattice, that of its missing nearest neighbor. If a vacancy of the same sublattice than the dangling bond atom is added, the total spin of the system is zero in agreement with Lieb's theorem. When the additional vacancy belongs to the opposite sublattice, a critical value of the interaction U_c is needed to obtain the total spin S=1. For $U < U_c$ the total spin is zero. The situation is similar to the one discussed previously with pentagons but in the case of the dislocations there is a critical region $0.2 < U < 1$ where the fully polarized and the unpolarized ground states are almost degenerate in energy and we find a coexistence of both cases. In fig. 2.11 we show the two spin configurations obtained at a value of U=0.3 for two defects located at the same relative distances on the lattice with total spin $S_z = 0$ (left) and $S_z = 1$ (right).

This situation points towards a first order magnetic transition in the presence of dislocations but this issue can not be explored with the techniques of the present work.

Finally, we would like to discuss the effects of Stone-Wales defects in magnetism. Although they have almost no effect on the electronic structure as we discussed in the previous section, their presence does alter the magnetic structure of the unperturbed lattice due to the presence of odd-membered rings. Their effect is similar to the pair of dislocations discussed in Sec. IV: in a lattice configuration with a number of dangling bonds of the same sublattice and in the presence of a SW defect a finite critical value of U is needed to reach a fully polarized ground state. This result agrees with the effect studied in Ref. [91] where Stone-Wales defects were assumed to be responsible for the destruction of the magnetization of graphene with atomic hydrogen adsorbed.

2.4 Discussion

In this chapter we have evaluated the effects of topological defects on the electronic structure of graphehe. With a tight binding model, we have described how the two types of disloca-

tions, shuffle and glide, induce distortions in the local density of states at low energies that decay rapidly with the distance to the defect. The presence of a dangling bond in the shuffle dislocations drastically enhances these effects but, as in the case of zigzag states, the low energy states are very localized.

Dislocations in metals have been proposed to give rise to electron localization in 3D systems [92] although the tendency to localization seems to be much weaker in 2D crystals [93]. The nature of the lowest energy states found in this work is an indication that dislocations probably do not localize states at zero energy in the honeycomb lattice, in agreement with what happens in metals [93]. Further systematic studies of the role of topological defects in localization are very interesting to consider in the future.

Then we have discussed how magnetism is modified by the presence of topological defects by means of a Hubbard model. To our knowledge this is the first work where this has been addressed in the literature. The importance of the present work relies on the fact that dislocations and other frustrating defects are very likely to be present in the real graphene samples and they should be taken into account.

We have shown that the nucleation of magnetic moments in the graphene honeycomb lattice is severely modified by the slightest frustration of the bipartite character of the lattice. The most dramatic effect appears when considering standard vacancies of the same sublattice. It is known that for values of the defect density not exceeding a certain value of about one percent, the ground state of the system at half filling has maximal spin given by the sublattice unbalance for any value of the Hubbard U. This result has been proven to be quite robust and to apply for interactions beyond the Hubbard model. We have shown that the presence of a single link frustrating the sublattice symmetry in a cluster of up to 3200 atoms is enough to rise the critical U to a rather high value of U=2. This critical value is similar to the one that induces an antiferromagnetic instability in the perfect lattice estimated to be in mean field of the order of $U \sim 1.8$ although the value increases when more refined calculations are done up to $U \sim 4.5$ [94].

We have explored a complete variety of situations with several vacancies or with several shuffle dislocations acting as sources of unpaired electrons and found the same results. The presence of a single link joining two atoms of the same sublattice (not necessarily forming a pentagon) is enough to induce a finite critical value of U_c. In the case of more complicated distributions of dislocations or Stone-Wales defects, the critical U state depends on the density and relative position of the defects.

As a positive remark we have found that the effect of dislocations is milder to the magnetism than that of the single pentagonal rings. The situation is richer and very low critical values of U are found where the two spin polarizations coexist. The dependence of the critical U on the density and relative distances of the defects is a very interesting matter which deserves further work, but the main conclusions presented will remain as discussed.

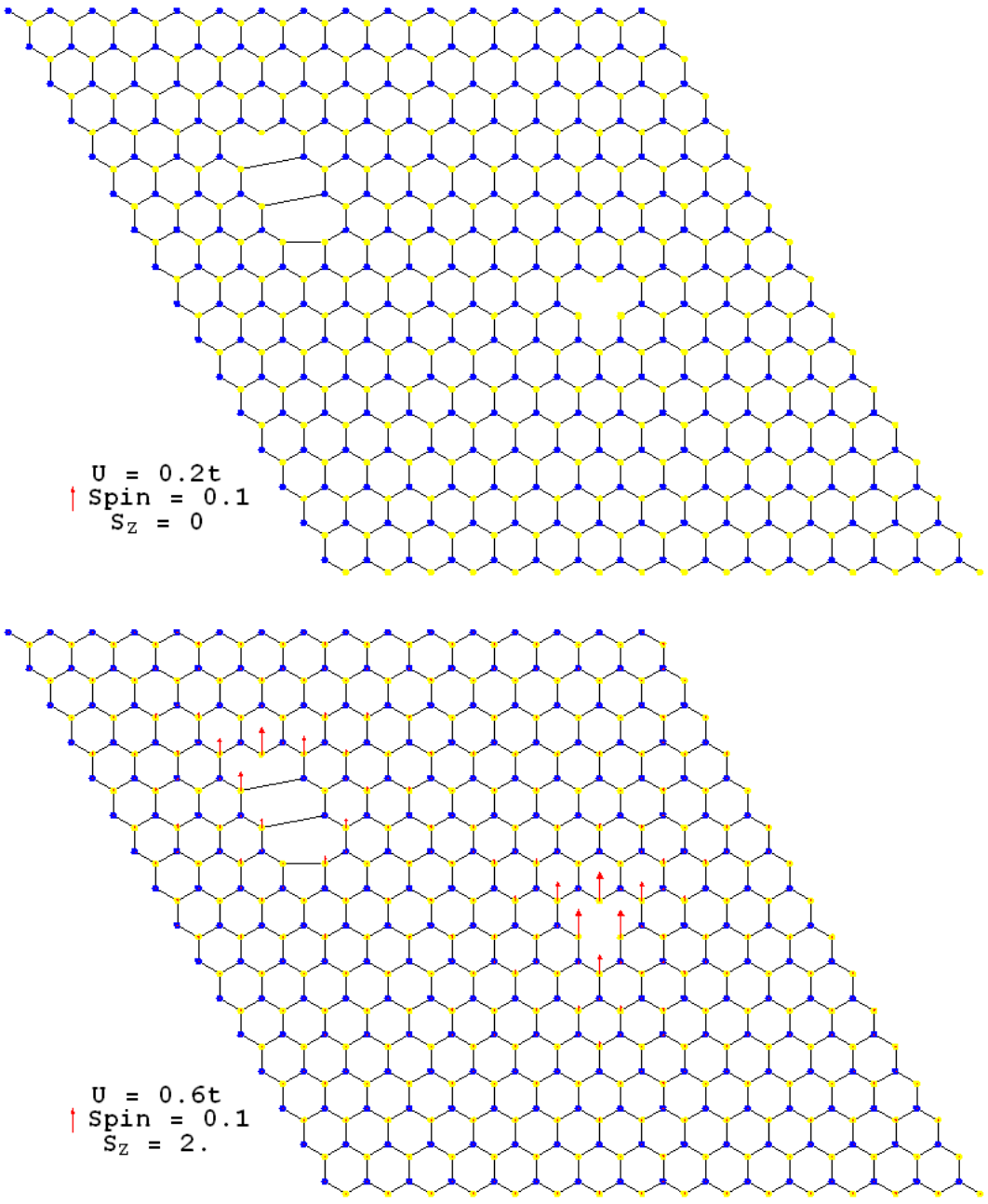

Figure 2.11: Ground state of the system with a dislocation and a vacancy. The circles represent the charge in the atom and the arrows represent the spin. Up: U/t=0.2 with total spin 0. Down: U/t=0.6 with total spin 1

3 Continuum models for curvature and topological defects

In this second chapter, we now focus in continuum models, based on field theory in curved spaces, to describe the influence of morphology in the electronic properties. These models allow a natural description of both smooth corrugations and topological defects.

We will first present an introduction to the morphological properties of graphene. Then, we will introduce the tools of differential geometry needed to describe spaces with curvature and torsion. These tools will be used to set up a model of smooth curvature to describe ripples, and to show how dislocations can be modelled with torsion.

3.1 Introduction

One of the aspects that make graphene unique is the fact that it is one of the few existing purely two dimensional crystals. Prior to the isolation of graphene, it was unclear under what conditions two dimensional, one atom thick crystals were stable, if at all. The mechanical and structural properties of graphene as a soft membrane have received much attention since its discovery [13, 95–97], but a full understanding of the situation has not been reached yet.

A detailed understanding of the morphological properties of graphene is also crucial from the electronic point of view, since the electronic structure or the transport properties may be affected by its non-trivial structural configuration. The purpose of this chapter is to discuss this interesting interplay between electronics and morphology.

Two main properties may alter the otherwise flat structure of graphene: smooth curvature, and topological defects. Topological defects have been introduced in the previous chapter, so we will start by discussing the origin and relevance of curvature. Then we will proceed to explain the theories we will use to model them, and discuss their results.

3.1.1 Corrugations in graphene

The first experiments dealing with the morphology of graphene were performed both in suspended samples and in samples on SiO_2 substrates. In suspended samples, [20] electron diffraction measurements showed that the graphene flakes presented microscopic corrugations, of an estimated size of 10nm and of heigths up to 1nm. In SiO_2 substrates, Scanning

Tunneling Microscope (STM) images were also obtained with good resolution [98, 17] (see fig. 3.1), showing that graphene also presents corrugations in substrates. The scales of these corrugations seemed to agree with those obtained from suspended samples. More recent STM experiments [99, 100, 18, 101, 102] have confirmed that corrugations are ubiquitous in samples on SiO_2 (corrugations of this type are not as important in samples grown epitaxially in SiC, where STM studies have also been performed [103–106]).

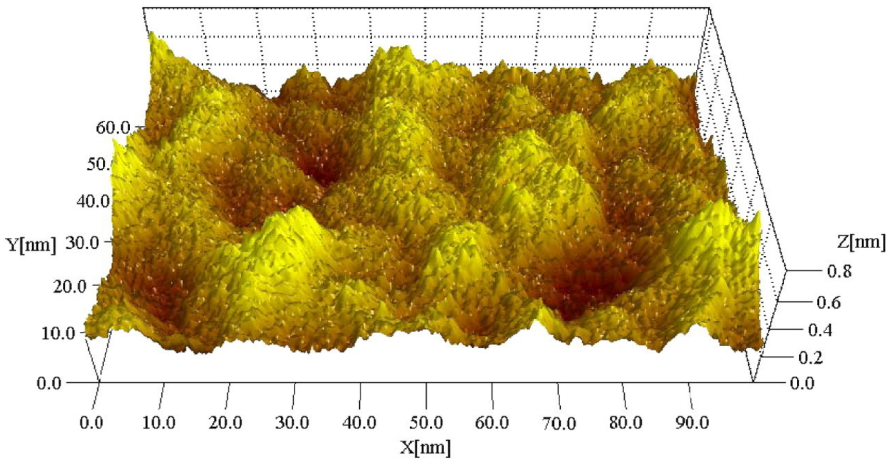

Figure 3.1: STM image of a graphene layer on SiO_2, measured in [98]. The corrugation of the surface is clearly observed (note the scale in the z direction has been enlarged to accentuate the surface features).

The origin of these corrugations is a very interesting matter. It has been shown that the SiO_2 substrate is not itself flat, so that graphene layers deposited on it partially inherit its morphological structure [17] due to their interaction [107]. This has been exmplified very clearly by high-resolution AFM images comparing the height profile of graphene on different substrates [19]. When graphene is deposited on a substrate much flatter than SiO_2, such as mica, its height fluctuations diminish, to the order of 20 pm. Interestingly, this is the order of magnitude of fluctuations in height of cleaved graphite as well. Another STM experiment [18] revealed that, in fact, intrinsic corrugations of the size of those found in suspended graphene are also found on top of the corrugations induced by the substrate (but interestingly, not in all samples). Another, larger class of wrinkles (up to 3nm in height) have recently been reported in [108], which do not seem to be related to the substrate inhomogeneity. Finally, STM measurements have been also performed on graphene on graphite[1], and no signatures of structural disorder were observed [109]. It is interesting to note that the morphology can be altered artificially as well. For example ripples have been induced in suspended graphene by controlled strains [97], and macroscopic bubbles can also be formed when gas is released

[1] In this experiments, monolayer flakes are searched which are almost decoupled from the graphite substrate, see [109]

from the substrate [110].

While the presence of intrinsic ripples is widely acknowledged, their origin has been debated, and we refer to [7] for a thorough discussion and references. It is known that free 2D membranes in 3D space have a low temperature stable flat phase with which nevertheless presents thermal fluctuations which could explain their origin. It has also been shown that these membranes have a tendency to crumple by generating topological defects [16], which an appealing partial explanation for the curvature (topological defects in graphene have been discussed in chapter 2), but it is not known if the physics of the crumpling transition has any relevance for graphene. In a realistic description of suspended graphene membranes one has to take into account several factors such as the scaffolds supporting the sample, the finite size or the temperature. Regardless of their origin, the experimental evidence of the presence of ripples raises the immediate question of their influence on the electronic properties of graphene, and this will be the subject of study in this chapter.

The effects of the ripples on the electronic properties have been already studied under several perspectives. Ripples were invoked in the first experiments to account for the absence of weak localization in magnetotransport [111]. In samples on SiO_2, it was also observed that as the neutrality point is approached, electron-hole charge puddles appear [112], as well as distortions in the LDOS. The origin of these puddles has been attributed both to charge impurities in the substrate [113, 114], and to the morphological corrugations [115] (see Chapter 4 for a detailed discussion on Coulomb impurities). In a recent experiment, it has been reported [101] that LDOS inhomogeneities and structural ripples do not seem to be correlated, but the situation has not been conclusively resolved.

Ripples have also been studied as a scattering mechanism influencing the conductivity, both at zero [31, 116–119, 42, 120] and finite doping [121, 122]. This is important in particular to evaluate what is the limiting factor that prevents the achievement of higher mobilities, a key issue for electronic applications. Whether ripples, or some other mechanism such resonant scatterers or Coulomb impurities are limiting the mobility is a currently debated question [44].

In the previous chapter, we already mentioned topological defects as a possible source of curvature in the samples. Most of the remarks regarding the relevance of corrugations for the electronic properties apply for them as well. They also influence the electronic structure, and their effect is also relevant for the conductivity. (A discussion about both general theory and experiments on topological defects and their relevance to graphene was presented in the mentioned chapter, to which we refer for further details.)

Since the description of topological defects fits naturally in the scheme of field theory in curved space to be used for the smooth corrugations, we will present the general formalism to be used with both first. Then we will present the application to corrugations, and finally to topological defects. As a final remark, we note that the defects to be discussed in this chapter are only those for which the term topological applies in the strict sense, i.e. those

which look like local but cannot be eliminated by local changes of the lattice.

3.2 Field theory in curved space

In this section, we describe a general formalism to study the effects of the topography of the sample on the electronic degrees of freedom. The model we propose is based on the assumption that the low–energy physics of the system is still described by a Dirac equation in the presence of both smooth curvature and topological defects. This assumption is supported by the recently demonstrated stability of Fermi points in momentum space [23].

The formalism that we are going to use is described with the language of differential geometry. We will summarize here the key concepts required for the discussion and provide all the technical details in Appendix A.

A general metric curved space, a Riemann-Cartan manifold, is characterized by two tensor fields defined in the manifold, the metric $g^{\mu\nu}$, and the torsion $T^{\lambda}_{\mu\nu}$. The metric defines a local concept of distance, from which a natural parallel transport of vectors can be defined. The torsion field can be understood as a local modification to this paralell transport.

In the case of smooth corrugations, the metric of the space in which the fermions move will be given by the embbeding of the graphene surface into three dimensional space. In the case of topological defects, there is a well established correspondence between the theory of defects in solids and the three-dimensional gravity [123, 124]. In this correspondence disclinations are known to be singular sources of curvature, and therefore provide the metric, while dislocations represent singular sources of torsion.

Once the torsion and the metric tensors are known, it is a standard procedure to derive the Dirac equation coupled to this background. The dynamics of a massless Dirac spinor in a curved, torsionless spacetime is governed by the modified Dirac equation [125]:

$$i\gamma^{\mu}(\mathbf{r})D_{\mu}\psi = 0. \tag{3.1}$$

The curved space γ matrices depend on the point of the space and can be computed from the anticommutation relations

$$\{\gamma^{\mu}(\mathbf{r}), \gamma^{\nu}(\mathbf{r})\} = 2g^{\mu\nu}(\mathbf{r}). \tag{3.2}$$

The covariant derivative operator is defined as

$$D_{\mu} = \partial_{\mu} - \Omega_{\mu}, \tag{3.3}$$

where Ω_{μ} is the spin connection of the spinor field that can be calculated using the tetrad formalism [125]. In the additional presence of torsion, eq. (3.1) takes the same form but the covariant derivative has some extra subtleties. Torsion will allow us to model dislocations in section 3.4. The technical details of the differential geometry of spaces with curvature and torsion are discussed in Appendix A.

In the torsionless case, this approach has been applied to study curved fullerenes [126–130] and to compute the response of electromagnetic charges to conical defects in planar graphene [131]. The coupling of the electronic degrees of freedom of planar graphene to conical defects has been explored in [132, 133]. There it was found that a distribution of pentagons and heptagons induces characteristic inhomogeneities in the density of states of the graphene surface. This formalism has also been used to model the coupling of scalar fields to dislocations [134], and the case of graphene was also considered in [135].

3.3 Smooth curvature: The gaussian bump

The first application of the formalism we have outlined will be to compute the modifications of the Local Density of States (LDOS) due to a smooth curved bump in the graphene sample.

3.3.1 The model

According to the previous section, what is needed is a metric describing the curvature of the surface. We will study the general case of a smooth protuberance fitting without singularities in the average flat graphene sheet. We start by embedding a two-dimensional surface with polar symmetry in three-dimensional space (described in cylindrical coordinates). The surface is defined by a function $z(r)$ giving the height with respect to the flat surface z=0, and parametrized by the polar coordinates of its projection onto the z=0 plane. The metric for this surface is obtained as follows: We compute

$$dz^2 = (\frac{dz}{dr})^2 dr^2 \equiv \alpha f(r) dr^2, \tag{3.4}$$

and substitute for the line element

$$ds^2 = dr^2 + r^2 d\theta^2 + dz^2 = (1 + \alpha f(r))\, dr^2 + r^2 d\theta^2. \tag{3.5}$$

We will assume that the surface is asymptotically flat at long distances, so that f decays with r fast enough. We will also require f to go to zero sufficiently fast in $r = 0$ so that the surface is smooth there. For clarity, we work out as an example the gaussian bump shown in fig. 3.2 defined by:

$$z = A \exp(-r^2/b^2), \tag{3.6}$$

so that

$$dz^2 = \frac{A^2}{b^4} 4r^2 \exp(-2r^2/b^2) dr^2, \tag{3.7}$$

which corresponds to eq. (3.5) with

$$\alpha = (A/b)^2, \qquad f(r) = 4(r/b)^2 \exp(-2r^2/b^2). \tag{3.8}$$

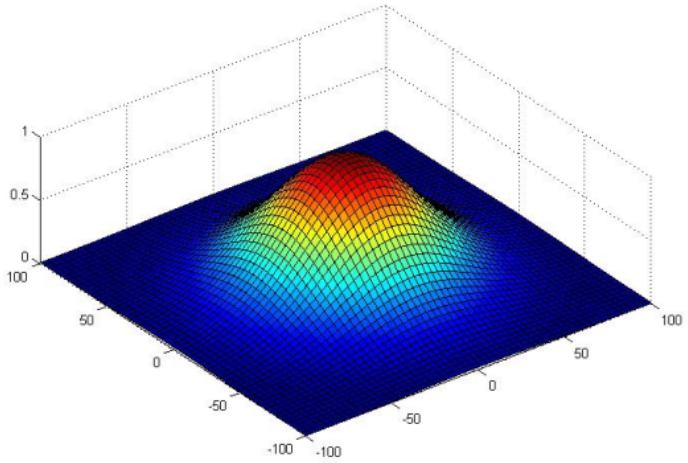

Figure 3.2: The smooth curved bump discussed in the text.

The ratio of the height to the mean width of the gaussian will be our perturbative parameter. As explained in section 3.1.1, the physical ripples observed in experiments can have heights A up to 1 nm. Their spatial extent b ranges from a few to tens of nanometers, so a typical ripple will have A/b in the range 0.1-0.3, and perturbation theory is justified.

Since we are going to work with the Dirac equation, our calculation is formally relativistic and the full space-time metric must be used. The line element reads:

$$ds^2 = dt^2 - (1 + \alpha f)\, dr^2 - r^2 d\theta^2, \tag{3.9}$$

from where we can write the metric in a more usual form:

$$g_{\mu\nu} = \begin{pmatrix} 1 & 0 & 0 \\ 0 & -(1+\alpha f(r)) & 0 \\ 0 & 0 & -r^2 \end{pmatrix}. \tag{3.10}$$

Note that curvilinear coordinates have their own geometric factors, which do not imply that the space itself has curvature. The Dirac Hamiltonian in flat space in polar coordinates can be written as

$$H_{flat} = \hbar v_F \begin{pmatrix} 0 & \partial_r + i\frac{\partial_\theta}{r} + \frac{1}{2r} \\ \partial_r - i\frac{\partial_\theta}{r} + \frac{1}{2r} & 0 \end{pmatrix}, \tag{3.11}$$

but, as discussed in Appendix A.3, the constant spin connection generated for this case is a "pure gauge" and can be rotated away by a different choice of local coordinates[2]. A discussion on this issue, as well as the calculation of the different geometric factors for the metric (3.9)

[2]We can see that the effective magnetic field generated by this potential is zero.

is given in Appendix A.3. The final Hamiltonian in the presence of the metric given by (3.9) is

$$H_{curved} = \hbar v_F \begin{pmatrix} 0 & (1+\alpha f(r))^{-1/2}\partial_r + i\frac{\partial_\theta}{r} + A_\theta \\ (1+\alpha f(r))^{-1/2}\partial_r - i\frac{\partial_\theta}{r} + A_\theta & 0 \end{pmatrix}, \tag{3.12}$$

where the effective gauge potential is related to the the spin connection (see (A.29) in the Appendix) by

$$A_\theta = \frac{\Omega_\theta}{2r} = \frac{1-(1+\alpha f)^{-1/2}}{2r}. \tag{3.13}$$

Comparing (3.11) with (3.12) we can evaluate the effects of curvature. The most interesting result of this formalism is that the curved bump has produced an effective Fermi velocity $\tilde{v}_r$ in the radial direction given by

$$\tilde{v}_r(r,\theta) = v_F(1+\alpha f(r))^{-1/2}. \tag{3.14}$$

The second effect is an effective magnetic field perpendicular to the graphene sheet, which can be obtained from the gauge field (3.13) as

$$B_z = -\frac{1}{r}\partial_r(rA_\theta) = \frac{1}{4r}\frac{\alpha f'}{(1+\alpha f)^{3/2}}. \tag{3.15}$$

The gauge field effect is more standard and has been obtained with other approaches (see [30] for a review on the different gauge fields appearing in graphene). The magnitude of this effective magnetic field is estimated to be of the order of 0.5 to 3 Tesla in the region spanned by the bump, compatible with the estimations given in [111], and it will play the same role in the issue of the weak localization of graphene as the effective magnetic fields discussed there and in [116].

The effective Fermi velocity obtained in this formalism will be in general smaller in magnitude than the free one. For a general curved surface described in polar coordinates by $z = z(r)$, the effective Fermi velocity will be

$$v_r = \frac{v_0}{\sqrt{1+z'(r)^2}}. \tag{3.16}$$

In a most general case we will have the two components of the velocity changed but always to a smaller value. This prediction can be used as an experimental test of this geometric model.

In the next section we specify the method to compute the density of states through the electron Green's function. For this purpose it is more convenient to follow the appendix and rewrite the Dirac equation in the form

$$\left[i\gamma^0\partial_0 + i\Gamma(\theta)\partial_r + i\Gamma'(\theta)\frac{\partial_\theta}{r} + V(r,\theta)\right]\Psi = 0, \tag{3.17}$$

which is the flat Dirac equation in polar coordinates in an effective potential V given by:

$$V(r,\theta) = i\Gamma(\theta)\left[1-(1+\alpha f)^{-1/2}\right](\frac{1}{2r}-\partial_r). \tag{3.18}$$

where $\Gamma(\theta) = \gamma^1\cos\theta + \gamma^2\sin\theta$. This effective potential will be used in the next section to compute the local density of states of the system. We can read in it two different terms related with our previous discussion: the derivative term has its origin in the effective r-dependent Fermi velocity and the term proportional to $1/r$ comes from the effective gauge field.

3.3.2 The Green's function in a curved spacetime. Approximations.

We now drop the polar coordinates for a moment to outline the procedure to obtain the Dirac propagator in a perturbative expansion in the small parameter α. The equation for the exact fermionic propagator in the curved space-time is:

$$i\gamma^\alpha e_\alpha^{\ \mu}\left(\partial_\mu + \Omega_\mu\right)\ G(x,x') = \delta(x-x')(-g)^{-\frac{1}{2}}, \tag{3.19}$$

where Ω_μ is the spin connection (A.29) and $\sqrt{-g}$ is the determinant of the metric (3.10), computed in (A.13). Since the flat propagator equation is recovered when $\alpha = 0$, expanding the left hand side to first order in α will give this flat equation plus a first order general term that we will call V. We can as well expand $(-g)^{-1/2} = 1-\alpha f(x)$, and sending the f term to the left hand side we get an equation resembling the flat propagator equation in a sort of potential generated by the metric

$$(i\gamma^\mu\partial_\mu + V)G(x,x') + \alpha f(x)\delta(x-x') = \delta(x-x'). \tag{3.20}$$

This equation can be solved by the usual pertubative expansion of G in a potential. Note that two approximations to order α are taking place: first, we expand the curved space exact equation for G to make it resemble the flat equation in a potential, and then we use a perturbative expansion in the potential to get the first order correction to G.

The solution for G is given by:

$$\begin{aligned} G(x,x') = G_0(x-x') - G_0(x-x')\alpha f(x) + \\ \int dx'' G_0(x,x'')V(x'')G_0(x'',x'). \end{aligned} \tag{3.21}$$

We now proceed to use this expansion in our particular case. The determinant of the metric is just:

$$g^{-1/2} = \frac{(1+\alpha f)^{-1/2}}{r} \approx \frac{1-\frac{\alpha f}{2}}{r}. \tag{3.22}$$

Expanding (3.18) to first order in α we get:

$$V(r,\theta) = i\Gamma(\theta)\left[\frac{1}{2}\alpha f(r)\right](\frac{1}{2r}-\partial_r). \tag{3.23}$$

Noting that the flat δ function in polar coordinates is $\delta(r-r')/r$, we can use eq. (3.21) in polar coordinates to get the first order correction to the propagator.

Next we need the Dirac propagator in polar coordinates. We will get it by noting that the Dirac and Klein-Gordon propagators are related by:

$$G_D^0 = D(x)G_{KG}^0, \tag{3.24}$$

where $D(x)$ is the Dirac operator. The Dirac operator in polar coordinates is:

$$\gamma^0 E + i\left[\Gamma(\theta)\partial_r + \Gamma'(\theta)\frac{\partial_\theta}{r}\right], \tag{3.25}$$

where we have defined:

$$\begin{aligned}\Gamma(\theta) &= \gamma^1\cos(\theta) + \gamma^2\sin(\theta),\\ \Gamma'(\theta) &= -\gamma^1\sin(\theta) + \gamma^2\cos(\theta).\end{aligned} \tag{3.26}$$

The Klein-Gordon propagator in polar coordinates is

$$G_{KG}(r-r',E) = \frac{-i}{4}H_0(E\left|r-r'\right|), \tag{3.27}$$

where H_0 is the zeroth order Hankel function [136]. Applying eqs. (3.25) and (3.24) we get:

$$\begin{aligned}G_D(r-r',E) = \frac{-iE}{4}\gamma^0 H_0(E\left|r-r'\right|) - \\ \frac{E}{4\left|r-r'\right|}H_1(E\left|r-r'\right|)\left[r\Gamma(\theta) - r'\Gamma(\theta')\right].\end{aligned} \tag{3.28}$$

Now we just use eqs. (3.21) and (3.28), and the first order potential (3.23) to get the local density of states

$$\rho(E,\mathbf{r}) = -\frac{1}{\pi}ImTr[G(E,\mathbf{r},\mathbf{r})\gamma^0]. \tag{3.29}$$

After two partial integrations we obtain the local density of states as:

$$\begin{aligned}\rho(r',E) = g\frac{E}{2\pi}\frac{1}{(v_F\hbar)^2}[1 - \frac{\alpha f(r')}{2} + \frac{\alpha}{8}\int drd\theta \\ \left[4E^2 f(r)r\frac{r-r'\cos(\theta-\theta')}{(r^2+r'^2-2rr'\cos(\theta-\theta'))^{1/2}}Y_1(E\Delta r)J_1(E\Delta r) - \left[2f'(r)+rf''(r)\right]Y_0(E\Delta r)J_0(E\Delta r)\right],\end{aligned} \tag{3.30}$$

where g is the spin and valley degeneracy, $\Delta(r) \equiv |r-r'|$ and Y_i, J_i are Bessel functions [136]. We will analyze this result in the next section.

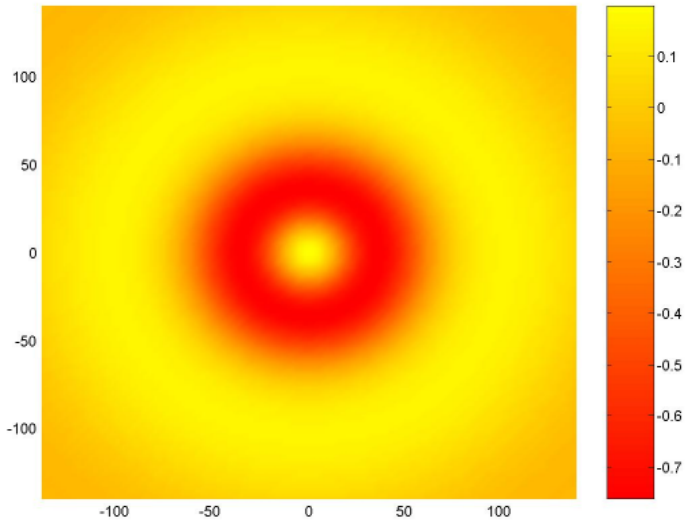

Figure 3.3: Effect of the curved bump of fig. 3.2 on the local density of states of the graphene sheet.

3.3.3 Results

We now proceed to analyze the result of eq. (3.30). We see very generally that the gaussian bump induces corrections to the LDOS which, due to the Bessel functions, show spatial oscillations whose frequency grows with the energy and whose amplitude decays with the distance as (1/r). Fig. 3.3 shows the correction to the LDOS induced by the shape of fig. 3.2 with a mean width b of 50 Å and for an energy of $E = 0.1$ eV. The color scale is indicated in the figure. Lighter (darker) color means a positive (negative) contribution with respect to the flat graphene sheet at the given energy. The maximal value of the correction related to the bare LDOS $\rho(E,r)/\rho_0(E,r)$ for a bump of a ratio $A/b \sim 0.1$ is of the order of 1 percent. If the height of the ripples goes up to 0.3b, the maximal value of the correction to the LDOS due to the curved portion can reach 10 percent.

At low energies the maximal absolute value of the correction is correlated with the zero of the curvature which, in the particular case of the gaussian bump, coincides with the mean width $\sqrt{2}b$. Fig. 3.4 shows the correction to the local density of states (dotted line) in arbitrary units, versus the shape of defect (red – upper – line) and the curvature of the defect (yellow –middle– line) for a gaussian bump of an average width of 50 Å. The energy is 0.1 eV. The figure represents real space in polar coordinates. The horizontal axis is the r coordinate while the vertical axis represents real height in the case of the upper line (shape of the gaussian bump considered). The middle line (curvature) given in eq. (A.22) is not measured in units of length. Finally the dotted curve gives the correction to the LDOS in arbitrary units. This results seems to be at odds with related works based on topological defects [132, 133] or

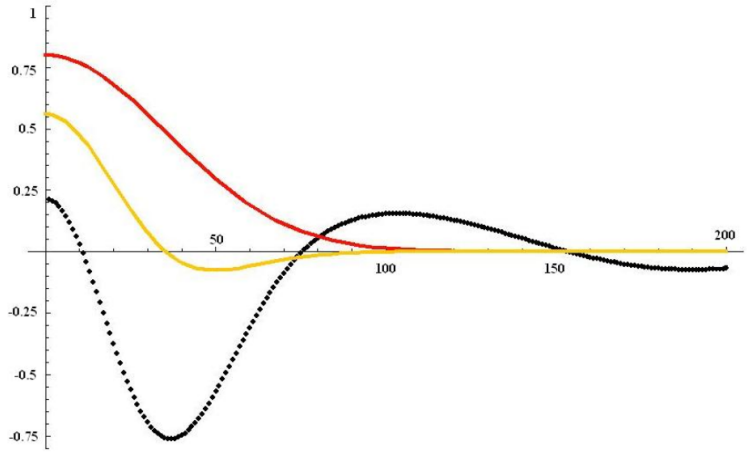

Figure 3.4: Correction to the density of states (dotted line) in arbitrary units, versus the shape of defect (red – upper – line) and curvature of the defect (yellow –middle– line) for a gaussian bump of an average width of 50 Å.

elasticity [115] that correlate the physical effect of curved portions with the actual value of the geometrical curvature.

We notice here that of the two effects of the curvature discussed in this work, only the effective magnetic field coming from the spin connection can be compared with previous works. In our case and in the general situation of having a smooth shape with axial symmetry, the effect of the effective gauge field vanishes at first order in perturbation theory and the corrections to the local density of states come exclusively from the spatial dependence of the Fermi velocity. This effect has not been noticed before because most of the previous works coupling the Dirac equation to curved space dealt either with spherical shapes where the correction to the Fermi velocity is constant and can be scaled out, or with conical shapes whose intrinsic curvature is accumulated at the apex singularity.

For simplicity we have modelled the ripples with shapes that are axially symmetric and the axial symmetry is explicit in the results. More general shapes would made the calculation much more complicated without altering the main results.

We can observe in figs. 3.3 and 3.4 that the maximal value of the correction to the LDOS is concentrated in the region spanned by the bump. In an STM experiment done on the curved surface the results on the LDOS plotted on the flat surface should resemble the rings of fig. 3.3 and would be in a very precise correspondence with the morphology of the sample.

To verify the apparent pining of the maximal value of the correction to the zero of the curvature observed in fig. 3.4 we have explored a set of gaussian shapes with different widths. The result is plotted in fig. 3.5. The correlation is good for the physical values of the bump from 2 to 5 nanometers (50 Å). Fig. 3.6 shows the dependence of the correction to the LDOS with the energy. The four plots show the correction induced by the same bump of a width

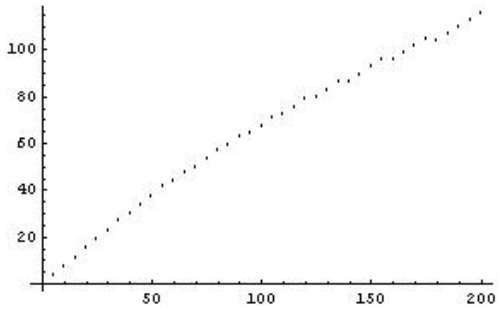

Figure 3.5: Plot of the location of the maximal correction of the LDOS for a fixed energy as a function of the extension of the Gaussian b.

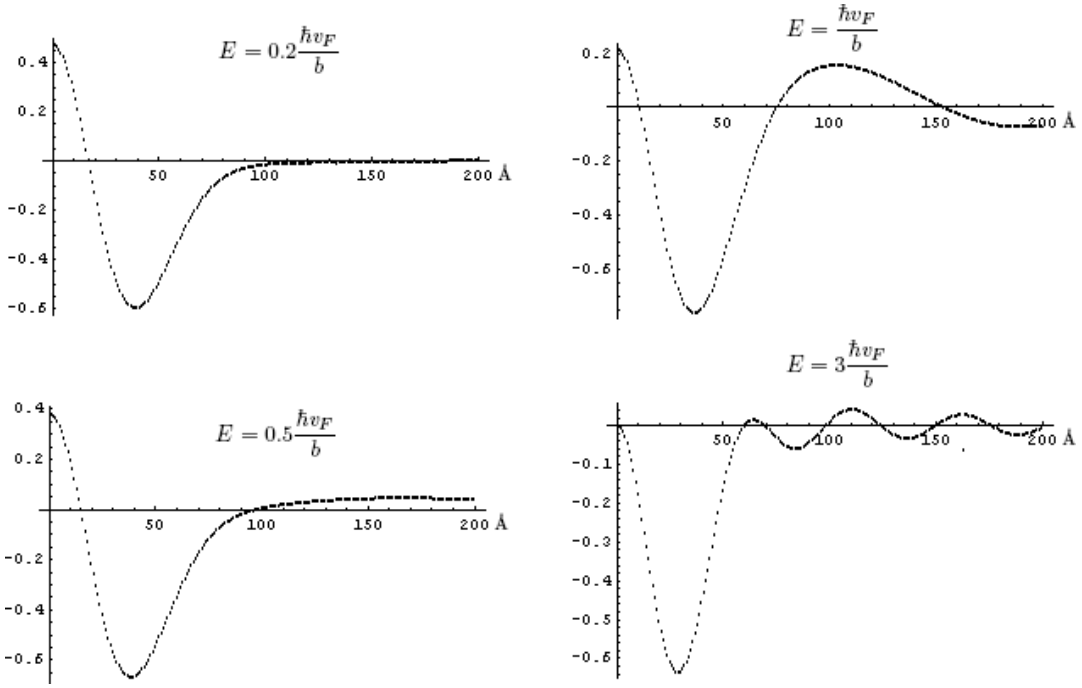

Figure 3.6: Correction to the density of states of a bump of fixed width (50 Å) for different values of the energy.

of 5 nanometers for growing values of the energy.

3.4 Dislocations and torsion

In the previous section, a model of field theory in curved space has been set up to deal with the presence of curvature in graphene samples. We have explained how the formalism can include both smooth corrugations and disclinations as sources of this curvature. In this section we propose how this model can be extended to include a finite density of dislocations,

which act as sources of torsion.

In section 3.2 we introduced the metric and the torsion field as the basic elements of a Riemann-Cartan manifold. Up to now, we have always set the torsion equal to zero for simplicity. Now, we will give a geometrical interpretation of torsion in terms of translational anholonomy, which will allow us to relate to dislocations. For this, we need to understand the meaning of the connection.

In differential geometry, a connection defines the notion of parallel transport. When a vector B^μ is parallel transported from x^μ to $x^\mu + dx^\mu$, it experiences an infinitesimal variation given by

$$\delta B^\mu = -\Gamma^\mu_{\nu\rho}(x) B^\nu dx^\rho. \tag{3.31}$$

The equivalent of the closed circuit in the definition of the Burgers vector can be defined by taking two infinitesimal vectors m^μ and n^ν, and trying to build a parallelogram with them. For this purpose, one parallel transports the vector m^μ along n^ν:

$$m'^\rho = m^\rho + n^\rho - \Gamma^\rho_{\mu\nu} m^\mu n^\nu, \tag{3.32}$$

and the vector n^ν along m^μ

$$n'^\rho = m^\rho + n^\rho - \Gamma^\rho_{\nu\mu} m^\mu n^\nu. \tag{3.33}$$

As depicted in fig. 3.4, if there is a dislocation in the region enclosed by the path, the parallelogram obtained does not close, and the part that is missing is proportional to the antisymmetric part of the connection, defined as the torsion:

$$m'^\rho - n'^\rho = \left[\Gamma^\rho_{\mu\nu} - \Gamma^\rho_{\nu\mu}\right] m^\mu n^\nu \equiv T^\rho_{\mu\nu} m^\mu n^\nu. \tag{3.34}$$

Notice that the two paths would have closed in a curved space with a standard affine connection.

In the continuum limit, one can describe a density of dislocations by the density of Burgers vector, and we see that torsion plays precisely this role. Hence the natural identification of torsion with dislocations. The connection of torsion with the continuum theory of crystal dislocations goes back to K. Kondo [137] and has been formalized in [124, 138]. A nice review on the relation of gravity with topological defects in solids is [139].

3.4.1 Dirac fermions in a space with dislocations

The dynamics of a massless Dirac spinor in a curved spacetime is governed by the modified Dirac equation (see Appendix A.4):

$$i\gamma^\mu(\mathbf{r}) D_\mu \psi = 0. \tag{3.35}$$

Coupling a Dirac field to a curved space with torsion gives the so-called Einstein-Cartan-Dirac theory. The details of the derivation of the Dirac equation in a space with torsion are

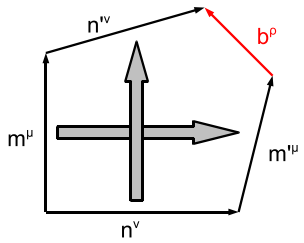

Figure 3.7: Non-closure of infinitesimal parallelograms due to the presence of torsion

given in Appendix A.4. Here we will simplify the description putting it in a different, more physical way. The minimal coupling of any geometrical or physical fields to the Dirac spinors adopts always the form of a covariant derivative:

$$\partial_\mu \Rightarrow D_\mu = \partial_\mu + A_\mu, \tag{3.36}$$

where the given vector can be an electromagnetic potential induced by a real electromagnetic field or any other real or fictitious gauge field associated to deformations or to geometrical factors [30]. In the case of having a density of dislocations in the graphene sheet modelled by torsion we can construct two potential candidates to gauge fields. In four dimensions, from the rank three torsion tensor (A.5) $T_{\mu\nu\rho}$ the following vectors can be built:

$$V_\mu = g^{\nu\rho} T_{\nu\rho\mu} S_\mu = \epsilon_{\mu\nu\rho\sigma} T_{\nu\rho\sigma}. \tag{3.37}$$

The field V_μ is a real vector and can be associated to the density of edge dislocations while S_μ is an axial (pseudo) vector associated to the density of screw dislocations. These fields couple to the vector and axial current density respectively so the full Lagrangian is:

$$L_{\text{int}} = \int d^4x \bar{\Psi} [\gamma^\mu (\partial_\mu + ieV_\mu + i\eta\gamma^5 S_\mu)] \Psi, \tag{3.38}$$

where e and η are coupling constants related to the density of edge and screw dislocations respectively. The physical consequences of the vector torsion are then similar to these coming from curvature or elasticity. The coupling of the spinor to the axial field A_μ can have important consequences as it breaks time reversal symmetry.

In (2+1) dimensions the completely antisymmetric part of the torsion tensor is proportional to the Levi-Civita tensor:

$$T_{\mu\nu\rho} = \varepsilon_{\mu\nu\rho} \Phi, \tag{3.39}$$

where Φ is a pseudoscalar field.

In 2+1 dimensions there are no screw dislocations, simply because there is no third spatial dimension, and the antisymmetric part of the torsion is rather related to time displacements.

Since the time components of the torsion generated by a dislocation are zero, this term vanishes always. The remaining coupling to the trace part acts a new vector gauge field with special symmetry properties associated to the dislocations structure of the sample. This field will add up to these coming from curvature or to real electromagnetic fields.

A remaining interesting question is that of how this extra gauge field couples to the electronic excitations around different Fermi points (valleys). It is known that the fictitious gauge fields arising from elastic deformations as well as these coming from curvature, give rise to effective magnetic fields pointing in opposite directions in different valleys. The reason is that the sign of the coupling of the effective vector fields depends uniquely on the definition of the spin connection (3.40)

$$\Omega_\mu = \frac{1}{8}\omega_\mu^{ab}\left[\gamma_a, \gamma_b\right], \tag{3.40}$$

and is determined by the product of gamma matrices in it. As the effective Hamiltonians around each of the Fermi points differ in the sign of only one of the gamma matrices (they are similar to parity conjugated) the spin connection has opposite signs in the two valleys. This is irrespective of whether the connection has or not an antisymmetric part and hence applies also to the coupling induced by torsion.

3.4.2 Systems with 3D Dirac fermions

We have seen in the previous sections that the effects of dislocations in two dimensional crystals like graphene are – at most – describable in terms of a fictitious gauge field similar to the one associated to curvature. The formalism outlined in this work acquires full power when applied to three dimensional crystals supporting screw dislocations and having Dirac fermions in the spectrum. Graphite is one of the most obvious candidates where screw dislocations are very common [140] and elementary excitations behaving as Dirac fermions were predicted near the K points of the band structure in the early calculations [9, 141]. These Dirac fermions have been experimentally confirmed in [142, 143].

The other perfect candidates are the the topological insulators [144–146]. These systems can be described by massive three dimensional Dirac fermions in the bulk. specially the Z_2 type that are protected by time reversal symmetry. The axial part of the torsion will couple to the three dimensional Dirac fermions, break the TRS and affect the topological stability.

3.5 Conclusions

In this chapter we have proposed a model based in the Dirac equation in curved space to study the influence of the morphology on the electronic properties. The main result is the confirmation of the fact that the curvature of the graphene samples is correlated with the electronic structure.

In particular, we have shown that the presence of smooth ripples induces corrections to the density of states. We have considered as an example a gaussian bump of the typical sizes found in experiments, and found that the effective potential generated by the curvature induces oscillations in the local density of states that affect significantly the region spanned by the bump. A conservative estimate gives a relative correction to the flat density of the order of 0.5 to a few per cent at the energies usually explored with STM probes that should be able to correlate the morphology with the predicted correction.

With complete generality we have seen that the curvature of the graphene sheet has two distinct effects with physical consequences. First the covariant derivative induces an effective magnetic field (the spin connection) that depends on the shape of the curved surface, in the spirit of other gauge fields that have been obtained previously. However, the first order corrections to the LDOS coming from this piece were shown to vanish.

The second effect is even more interesting and comes from the curved Pauli matrices. They modify the Fermi velocity that becomes a function of the point on the graphene surface and is always lower than the free velocity. This is not to be confused with the renormalization of the Fermi velocity induced by electron-electron interactions [147] or disorder [148, 149] where the Fermi velocity becomes effectively a function of the energy. This effect has not been noticed before because most of the previous works coupling the Dirac equation to curved space dealt either with spherical shapes where the correction to the Fermi velocity is constant and can be scaled out, or with conical shapes whose intrinsic curvature is accumulated at the apex singularity.

It would also be very interesting to consider that a random Fermi velocity would affect the transport properties in an unusual way, as happens for example in [120].

Regarding dislocations, in what two dimensional graphene sheets are concerned the main results of this chapter are somehow disappointing: spinors in two spatial dimensions do not couple to the axial part of the torsion (since there are no screw dislocations). Such a coupling would have had very important consequences. The coupling to the trace part is in the form of a vector gauge field similar to the one produced by the curvature or by strain in a more conventional approach. The spatial distribution of this new gauge field will nevertheless depend on the density of dislocations.

The results of this section are more relevant for the systems that support three dimensional Dirac fermions. In these systems, the presence of the torsion axial vector as produced by screw dislocations in the Dirac equation will have important implications. As torsion breaks time reversal symmetry effectively, a random configuration of dislocations may affect the localization properties of the system.

4 Spectral properties of disordered graphene

This chapter will focus on the effect of disorder, and in particular of charged impurities, in the spectral properties of graphene. We will first present a general overview on disordered electronic systems, as well a as discussion on screening, a very important issue for this type of impurities. After that, we will be ready to discuss in some detail the complex problem of disorder in graphene.

We will then focus in particular on the effect of the mentioned Coulomb impurities on the spectral properties. We will present the methods employed in the study of this problem, the results obtained, and we will comment on them in the discussion section.

4.1 Disordered systems

Experimental condensed matter systems are never perfect or ideally pure: A given sample of a material may present structural defects in the lattice, substitutional atoms, neutral, charged or magnetic impurities, irregular strains... All these deviations from idealness, which go generically under the name of disorder, have implications for the electronics of condensed matter systems of varying relevance: Sometimes their effect can be rather weak, producing mild (but observable) changes in the physics, while in other cases even the smallest amount of disorder may give rise to qualitative (and sometimes drastic) alterations, like in the paradigmatic case of Anderson localization in two dimensions [150]. In describing a particular system, it is therefore very important to be able to evaluate the specific effects of disorder. In this section we outline the theoretical tools employed for such analysis, with the final aim of applying them to graphene.

As usual in condensed matter physics, the full Hamiltonian of electrons in a solid in the presence of many impurities, defects or the like is in principle easy to write, but in practice very difficult to solve. Moreover, one may not be interested in the local properties of a particular configuration of such defects, but rather in how the bulk features such as spectral or transport properties are generically modified by disorder. In this case, as we will explain, it is much more useful to consider an averaged theory, in which observables are computed by averaging over the positions of all impurities with a particular distribution. This is a standard way of dealing with quenched (static) disorder, and it is reviewed in detail, for example, in [151, 152]. We will mainly follow these last references in this introduction, but other recommendable books covering the topic are [139, 153, 154].

First of all, how is an averaged theory related to the particular configuration of disorder

to be found in a real sample? If the system size is large enough so that different regions of the sample can be considered independent, the integral in space of a local quantity in a configuration tends to the configuration average of that quantity. This phenomenon is called self-averaging, and it underlies the usefulness and effectiveness of averaged theories. Averaging is useful first because it provides a model in which computations can be performed more easily, but more importantly because it reveals how a disordered system can be described in terms of a few generic parameters of the disorder landscape, rahter than in terms of the details of a particular configuration.

Depending on the problem we are interested in, our averaged theory may assume some kind of correlation among the impurity positions. Throughout the literature, the term "long range disorder" is generically used to describe both the case of *long range correlations* in the potential and the case when the *potential is long ranged* itself (such as the Coulomb potential) [1]. Due to the divergent infrared behaviour of these models, they are very difficult to deal with. Uncorrelated short range disorder is therefore usually taken as a simpler model (that can nonetheless describe the effect of disorder in many cases), but as we will see, sometimes long range disorder has to be dealt with inevitably.

The mathematical way of computing observables in these averaged theories is phrased in the language of Green's functions, which we have described in the section 3.3.2. Our purpose is to average n-particle correlators from which we can obtain physical information. For example, quasiparticle lifetimes or densities of states can be obtained from the one-particle Green's function, while transport quantities like the conductivity are obtained from the two particle correlator in linear response. The averaging procedure is standard [151], and is carried out order by order in perturbation theory.

4.1.1 Perturbation theory and approximations

We now discuss some details of the perturbative averaging and some common approximations. The first thing to note is that, while the perturbative parameter for the series is in principle the strength of the impurity potential $V(q)$, the averaging procedure introduces another scale, the density of impurities n_{imp}, and the series is organized in these two parameters. The heuristical interpretation of these parameters is that, for a particular term, the power of V represents the number of scattering events, and the power of n_{imp} represents the number of impurities on which these events occur. A diagrammatic representation is customarily used with scattering events denoted by dashed lines and impurities denoted by crosses. The infinite series for a particular correlator is of course not very useful, and several approximations have been commonly used to simplify the diagrammatic series depending

[1] Note that in this sense, if the scale defined by the impurities (be it the potential range itself or the correlation length if the impurities are correlated) is comparable or larger than the size of the system, averaged results may not be enough to describe a physical realization of the disordered system

on the problem at hand. They have been derived in several ways and contexts, and thus they go under different names in the literature. We will summarize them below, following the naming of [152], commenting briefly on other commonly used conventions. Since we will be interested in spectral properties, we will show explicitly the diagrams for the self-energy, related to the one particle propagator through the Dyson equation

$$G^{-1} = G_0^{-1} - \Sigma \tag{4.1}$$

which is represented diagramatically in fig. 4.1.

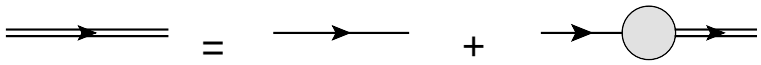

Figure 4.1: Diagrammatic representation of the Dyson equation. The double line represents the full propagator, the simple line the free (or in this case, non disordered) one, and the blob represents the self-energy.

The first approximation usually employed is to neglect the tadpole diagrams (such as the first one on the series of fig. 4.3a), since they only give a rigid shift of the energy. (Moreover, they add up to zero anyway if the same number of positive and negative impurities is considered). The next common one is to neglect multiple scattering from a single impurity, which can be done in the case of weak scatterers, when the Born criterion is satisfied[151]:

$$\frac{V(p=0)p_F^2}{v_F} << 1, \tag{4.2}$$

in three dimensions and

$$\frac{V(p=0)p_F}{v_F} << 1, \tag{4.3}$$

in two dimensions, where in both formulas p_F is the Fermi momentum, and v_F the Fermi velocity. (Note that this expression for the Born criterion applies when the range of the impurity is given in terms of p_F^{-1}. See [155] for a thorough discussion on the applicability of the Born approximation). Since in this case there is only one scattering event per impurity, we actually have a one-parameter series in terms of $n_{imp}V^2$. (This is sometimes called the gaussian limit [151], because it is equivalent to considering an average over a random potential with gaussian variance $n_{imp}V^2$, an approach better suited to path integral methods [152].) We will call this the *Born approximation*, and the first term in this series the *first order Born approximation*. The first order Born self-energy is depicted in fig. 4.2a.

In the opposite limit, if the impurity potential is strong enough, it may suffice to consider scattering from only one impurity at a time. In this case, all the relevant diagrams can be summed into an effective first order diagram known as the T-matrix of the impurity, represented diagrammatically in fig. 4.3a. This is called the *T-matrix approximation* for the self-energy, and is depicted in fig. 4.3b.

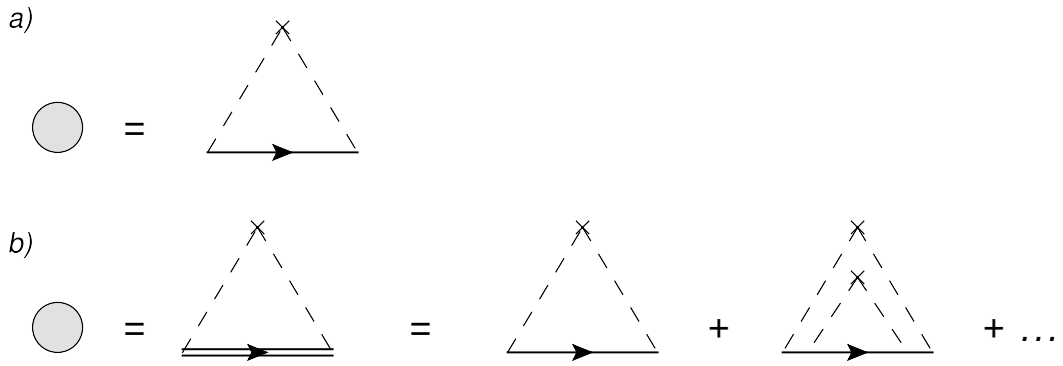

Figure 4.2: a) The first order Born self-energy. b) The self-energy in the self-consistent Born approximation, formulated in (4.4). Note the self-energy is included implicitly in the full propagator line.

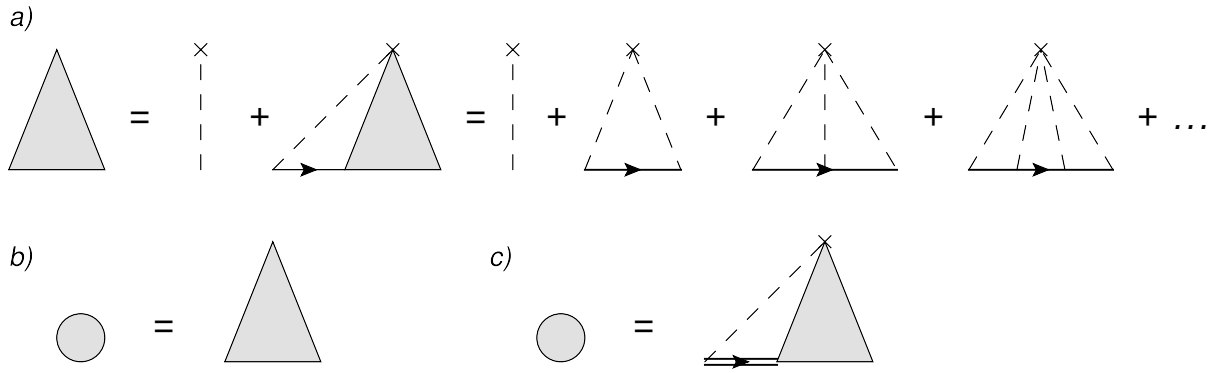

Figure 4.3: a) Diagrams for the T-matrix of a single impurity, represented by the shaded triangle. b) Self-energy in the T-matrix approximation, which uses the single impurity T-matrix as the self-energy. c) Diagrams for the self-consistent T-matrix approximation. Note again that the self-energy is implicitly included in the full propagator line.

In the presence of a Fermi surface, it is possible to go beyond these simple "first order" approximations by realizing that diagrams with crossed impurity lines are supressed with respect to the non-crossed ones by powers of $p_F l$ or $E_F \tau$, due to phase space restrictions in the momentum integrals. After dropping these terms, the remaining series can be resummed into self-consistent equations in both the Born and the T-matrix case, giving rise to the *self-consistent Born approximation* (SCBA), fig. 4.2b, and the *self-consistent T-matrix approximation* (SCTM), fig. 4.3c[2].

[2] As we anticipated, the namings of these approximations is not coherent accross the literature. The SCTM (and sometimes SCBA too) is also known as the coherent potential approximation (CPA)[154]. In other references [153] also followed by several authors, our T-matrix is called the full Born approximation, and our SCTM is called SCBA. For a coherent exposition we will therefore always follow the naming outlined in the text.

For example, the SCBA for the one particle correlator and a delta correlated potential $V(q)$reads

$$\Sigma(k,\omega) = n_{imp}\int \frac{d^n k'}{(2\pi)^n}|V(k-k')|^2 \frac{1}{G_0^{-1}(k',\omega)-\Sigma(k',\omega)}. \tag{4.4}$$

These self-consistent approximations can be understood as the semiclassical diffusive limit of disordered systems. Indeed, it can be proven that transport properties like the conductivity computed in the SCBA are equivalent to those given by the Boltzmann equation [139]. Corrections to this classical diffusive limit are obtained in inverse powers of $E_F\tau$, and are known as weak localization corrections. (It is important to note that the Boltzmann approximation is equivalent to SCBA only in the limit $E_F\tau << 1$.)

These models for disorder have proven very effective and have been used extensively across the literature, in particular for the two dimensional electron gas, providing very good agreement when compared to experiments. Reviewing this topic is far beyond the scope of this chapter, so we refer to standard books and reviews [156, 139, 155, 152, 153, 151]. This concludes our summary of the tools we will use in the description of disordered graphene.

4.2 Impurities and screening

Since in this chapter we will focus on the problem of Coulomb disorder, the issue of screening will be very relevant. We therefore review it in some detail before we address disorder in graphene. Screening is a key ingredient in the general discussion of the effect of charged impurities in any material. If a charged impurity is placed in a solid (either inside or outside), a test electron in the solid will be affected both by the bare potential of the impurity and by the charge of the other electrons that may have redistributed around it. How is the effective impurity potential modified by electron-electron interactions? This is a difficult problem, which is usually simplified by assuming a linear response approach. In this case, the response of the system is known to be given by the dielectric function:

$$V(q) = \frac{V_0(q)}{\epsilon(q,\omega\to 0)}, \tag{4.5}$$

which can be obtained from the charge-charge correlator, i.e., the polarization function

$$\frac{1}{\epsilon(q,\omega)} = 1 + V_0(q)\Pi(q,\omega). \tag{4.6}$$

In the high density limit, the polarization can be computed in the RPA approximation. This limit is defined as $r_s << 1$, where r_s is given in two dimensions by

$$r_s = \frac{1}{(\pi n)^{1/2} m e^2}, \tag{4.7}$$

where n is the density of electrons and m is the effective mass.(See [156] for a detailed discussion in the context of the 2DEG). If the density is lowered, non-linear response comes

into play (see for example [157]), and the parameter r_s determines the range of densities where the linear RPA model is applicable.

Although the particular form of the dielectric function depends on the dimension, it is a general feature that the effect of screening is to convert the infinite ranged Coulomb potential into a finite ranged one, decaying with a length scale that is given by the density of states at the Fermi level, much like in the case of Coulomb electron-electron interactions. While in the three dimensional case the screened potential has an exponential decay in real space, in two dimensions screening produces a weaker power law decay[156].

If we wish to describe not one, but many impurities, we face a more complex problem in terms of screening (ever before disorder averaging), because the screening of one impurity may depend on the charge accumulated on the rest. It is reasonable to assume independent screening of impurities when they are far apart, but this picture may start to fail when the screening length becomes bigger than the average distance between impurities $n_{imp}^{-1/2}$. The many impuritiy problem introduces another type of non-linearity which may become relevant at low dopings, where the screening is weak [158].

Even if independent screening is appropriate, it may be also relevant to take into account that, now after disorder averaging, the electrons screening one particular impurity also see the rest of the impurities in an average way. Therefore, this theory has to be corrected by computing the disordered polarization function in RPA[159], a correction that proved relevant to the experiments in the 2DEG of silicon inversion layers [160].

4.2.1 Screening in graphene

The particular case of screening of Coulomb impurities in graphene has been studied extensively, in both the zero or low doping region [161, 34, 37, 35, 162, 36, 163] and in the high doping one [34, 164]. One could expect the high doping case to be similar to the 2DEG, but a difference should be pointed out. Contrary to what happens in the 2DEG, the parameter r_s in graphene is density independent, and it is actually just the coupling constant $e^2/(\kappa v_F)$. This generates a difficulty in evaluating the range of validity of the RPA for graphene. It is understood that in the zero doping case it is definitely not valid [165], while it has been stated that in the doped case it is applicable when $r_s << 1$[166]. Since r_s is density independent, it is not clear how the two regimes interpolate, and to the best of our knowledge no quantitative criterion on $n = k_F^2/\pi$ has been established to separate them [3]. In spite of that, due to its simplicity and its qualitative success when confronted to experiments, the RPA polarizability has been thoroughly studied in the literature[168–171], and its static limit is

[3] Even at high doping, RPA has been claimed not to describe the charge-charge correlator correctly [167]. Moreover, it has been shown that, while the non-linear corrections to screening are stronger in the low density regime, they are not negligible for high density as one could expect[164]

known to be

$$\epsilon(q) = 1 + \frac{q_{TF}}{q}\Pi(\frac{q}{k_F}), \tag{4.8}$$

where $q_{TF} = 4\alpha_v k_F$ and

$$\Pi(x) = \begin{cases} 1 & x < 2 \\ 1 + \frac{\pi x}{8} - \frac{\sqrt{x^2-4}}{2x} - \frac{x \arcsin(2/x)}{4} & x > 2 \end{cases}. \tag{4.9}$$

For $k < 2k_F$, this is just the Thomas-Fermi result in 2 spatial dimensions [34], a feature that also happens in the 2DEG [156]. Thus impurities screened by graphene only differ from those screened by a 2DEG at $k > 2k_F$. While at high doping screening is therefore similar to the 2DEG, it is worth noting that when the doping goes to zero, RPA screening in graphene only changes the dielectric constant, leaving the long-range functional dependence unchanged. This is due to the vanishing density of states at the Fermi level, as discussed previously. Of course, the RPA result is questionable at zero doping, where the problem becomes strongly non-linear [161, 34, 37, 35, 162, 36, 163].

For our study of Coulomb impurities in graphene, we will stay at dopings high enough so that the SCBA applies. Bearing the previous discussion in mind, we will therefore use the linear response RPA polarizability as a model of screening. When discussing the low doping limit of our calculation, we should keep in mind that the SCBA and now also the RPA linear screening model are not applicable there.

4.3 Disorder in graphene

After setting up the context of disordered systems and discussing the issue of screening, we are ready to tackle the problem of disorder in graphene. As shown in the first section, the role of disorder in electronic properties is very important and graphene will be no exception in this sense. A large amount of the literature in graphene has been devoted to this broad topic, of which we will summarize the most relevant parts for our discussion. For further details we refer to [7], which contains an in-depth review of the subject.

Disorder may be present in graphene in a variety of forms: Vacancies, substitutional atoms, cracks and edges, topological defects, charged impurities, quenched or artificially produced strains... With respect to the low-energy electronic properties, they can be described by different types of potentials entering the Dirac equation and their correlations, in the line of the statistical model of disorder described previously.

If the disorder potentials are smooth on the scale of the lattice spacing, intervalley scattering is weak and the system can be described by a single Dirac Hamiltonian

$$H = \int d^2x \left[\psi^\dagger \boldsymbol{\sigma}\boldsymbol{\partial}\psi + \psi^\dagger V \psi\right], \tag{4.10}$$

where ψ_i are two component spinors, and the disorder potential V can be expressed in terms of the Pauli matrices

$$V = V_0\mathcal{I} + V_1\sigma_1 + V_2\sigma_2 + V_3\sigma_3. \tag{4.11}$$

Vacancies and impurities can be described by a diagonal potential V_0, while V_3 represents a random gap. The potentials $V_{1,2}$ are usually called gauge fields and may represent, for example, ripples or topological defects [7]. The potentials are usually taken to be uncorrelated for simplicity, but real disorder may present correlations which are important and should be included.

The model just described has been studied extensively in the case of zero doping and short range disorder even before graphene was synthesized because it arises in several other contexts in condensed matter physics [172, 38, 173]. In graphene it has been studied mostly for the scalar potential at the level of SCBA [174, 7, 175, 176] and with numerical recursion methods [78, 79, 177]. (The cases of the random vector/mass have also been studied, for example in [31, 117], but they will not be as relevant for our discussion)

The perturbative calculations in disordered graphene generalize easily from those explained in section 4.1.1, with the additional complication of the sublattice structure (or equivalently, the presence of two bands). The diagrammatic structure remains unchanged, but the Green's functions now have an additional spinorial structure. These are obtained by inverting the free Hamiltonian (4.10)

$$G_{ab}(k) = \frac{\omega\mathcal{I}_{ab} - \sigma^i_{ab}k^i}{\omega^2 - k^2}, \tag{4.12}$$

where the a, b are the spin indices. The Green's function, and therefore the self-energy, are 2x2 matrices, and so are the effective propagators for the averaged potential.

An alternative way to perform the calculations which has been used in the literature [169, 178, 176] is to swtich to the basis that diagonalizes the Hamiltonian. This is achieved by a unitary transformation $\psi = U\chi$, $\psi^\dagger = \chi^\dagger U^\dagger$, with

$$U = \frac{1}{\sqrt{2}}\begin{pmatrix} 1 & 1 \\ e^{-i\theta_k} & -e^{-i\theta_k} \end{pmatrix}, \tag{4.13}$$

which gives diagonal Green's functions

$$G_{ss'} = \begin{pmatrix} \frac{1}{\omega-|k|} & 0 \\ 0 & \frac{1}{\omega+|k|} \end{pmatrix}, \tag{4.14}$$

where the indices s and s' take the values $+, -$, denoting the upper and lower band. Note that since impurity scattering is elastic, the band index is conserved and therefore the off-diagonal elements are zero to all orders. The price to pay is that the impurity potential term is modified to

$$H_{imp} = \int d^2k d^2k' \chi^\dagger_k U^\dagger_k V(k-k') U_{k'}\chi_{k'}. \tag{4.15}$$

The SCBA for the short range case gives well known results. Note that, since the potential is independent of k, the self-energy in this approximation is also independent of k. At $\omega = 0$ it can be solved analitically, giving the well known finite purely imaginary self-energy

$$\Sigma(\omega = 0) = -\frac{i\Lambda}{\sqrt{\exp(\frac{4\pi v_F^2}{n_{imp} V_0^2}) - 1}}, \tag{4.16}$$

and the DOS

$$\rho_0 = \frac{1}{\pi n_{imp} V_0^2} \frac{\Lambda v_F}{\sqrt{\exp(\frac{4\pi v_F^2}{n_{imp} V_0^2}) - 1}}. \tag{4.17}$$

For undoped graphene, however, it has been long known that the SCBA is in principle not a good approximation due to the absence of a $E_F\tau$ type of parameter that would allow to neglect the crossing diagrams [179, 180]. Renormalization group calculations as well as exact results (see [173] and references therein) have been shown to differ qualitatively from the SCBA. Only in the special case of a large number of valleys N *and* disorder that mixes them all (an SU(N) non-abelian random vector potential) the parameter N plays the role of $E_F\tau$ and a non-crossing expansion is controlled, as was shown in [172], where a finite density of states and a universal conductivity $4e^2/\pi h$ are obtained.

Despite its supposed inaccuracy, the SCBA for both the scalar and vector cases gives this universal value of the dc conductivity at zero doping which is in qualitative agreement with experiment (although there is still controversy on the quantitative agreement). The dc conductivity has been studied for finite dopings also with SCBA [175], but the agreement with experiment is rather poor.

In fact, it is a major issue related to disorder to determine the dependence of the dc conductivity as a function of doping, which allows to determine the mobility. This is important because, if the predominant scattering mechanism is identified, we can try to suppress it in some way to produce higher mobilities, always an important goal from the point of view of applications.

From the first experimental samples [26], it was determined that the conductivity scales linearly with the doping. It was soon realized that this dependency of the conductivity is not obtained with the usual simple model of weak, short range disorder in the Boltzmann equation, and Coulomb impurities, which do show this linearity, were invoked to be the relevant scatterers. Several works addressed the effect of Coulomb impurities in the conductivity beyond the Boltzmann approximation [181, 114] mainly to be able to access the Dirac point. Several experiments seemed to support the Coulomb disorder scenario [182, 183], although the discussion has not been settled yet [184].

However, the situation turned out to be more complicated. First because it is important to know that other types of long-range correlated disorder such as ripples also give rise to the observed linear conductivity, see [122]. Second, and perhaps more importantly, because

strong short range scatterers giving rise to midgap states (resonant scatterers) give a linear dependence with a logarithmic correction in a semiclassical treatment that does not assume weak scattering [121, 185]. Since the weak and strong cases are so different, the SCBA may not be enough and short range scattering requires more attention. And third, because even in the weak short range case, the SCBA is equivalent to the constant Boltzmann result only for $E_F\tau >> 1$. The difference between the SCBA and Boltzmann in the case of Coulomb impurities has not been addressed yet in the literature.

The conductivity measurements pointed to the fact that dominant scattering mechanisms may differ from sample to sample. This difference can also be explored by a technique first employed in the 2DEG, which is measuring how the one-particle lifetime scales with doping, and comparing it with the transport lifetime [186]. In this context, the one particle lifetime is always computed within the first order Born approximation, while the transport time is computed from the Boltzmann theory. For example, the one-particle lifetime for a Coulomb potential screened by the dielectric function (4.8) at a density $n = k_F^2/\pi$ was computed in [186]:

$$\tau = \frac{1}{\Sigma} = \frac{k_F}{\alpha^2 n_{imp} v_F \pi I(2\alpha)}, \tag{4.18}$$

where $I(2\alpha)$ is a dimensionless function also given in [186] (for our purposes we will take $\alpha = 0.75$ and we have $I(2 * 0.75) = 0.224$). Comparing with the corresponding transport time, Hong et al. [187] reported that Coulomb impurities are the main source of scattering, while a similar analysis done in [188] concluded that the dominating disorder is given by resonant scatterers such as vacancies.

Since for the Coulomb case the one-particle lifetime (and indeed any one-particle property) has been computed only to first order, it is interesting to evaluate what changes occur when computing it with SCBA. In general, the SCBA has not been applied to Coulomb impurities because its implementation is not as simple as in the short range case (see however [189]). Solving infinite range problems in the SCBA poses a major problem due to infrared divergences (see for example [190] in the context of the 2DEG, or [191, 120] in Dirac fermions). However, in the case of long ranged Coulomb impurities and a finite density of carriers, the Coulomb potential is always screened, and this solves the infrared problem, as explained in section 4.2. In this case, the SCBA can be used, at least in a numerical fashion.

What is thus the effect on the spectral properties of Coulomb impurities beyond the first order? Our work will consist on addressing this question, but before describing our methods and results, we would like to shortly discuss what is understood by spectral properties and how they are usually measured.

4.3.1 Spectral properties of graphene

A lot of knowledge from a system can be obtained from the full one-particle Green's function. The main physical observables that can be obtained from the self-energy are the following:

- The local density of states can be measured by tunneling spectroscopy, and integrated to obtain the total density of states relevant for the conductivity. A disorder averaged theory can only provide the global density of states, obtained as

$$\rho(\omega) = \frac{1}{\pi} \lim_{x \to x'} Im[G(x, x', \omega)]. \tag{4.19}$$

- The quasiparticle lifetime, which can be obtained by measuring the exponential damping of the oscillations in the resistivity with magnetic field (Shubnikov-de Haas oscillations). As we discussed previously, this experiments have been done by several groups on graphene [187, 188]. The quantum lifetime is in general a function of energy and momentum $\tau^{-1}(k, \omega) = Im[\Sigma(k, \omega)]$, but the most interesting value is the on-shell lifetime at the Fermi energy $\tau^{-1}(k_F, E_F)$.

- The spectral function, which can be measured from angle-resolved photoemission spectroscopy (ARPES). This provides information about the excitations in the system, revealing the actual dispersion relation of the quasiparticles and their broadening, which is also the quantum lifetime discussed above. It is computed as the imaginary part of the Green's function, and in graphene it reads

$$A(k, \omega) = \frac{1}{\pi} \left[A_+(k, \omega) + A_-(k, \omega) \right] \tag{4.20}$$

  with

$$A_+(k, \omega) = \frac{Im[\Sigma_+(k, \omega)]}{(\omega - \omega_+(k) - Re[\Sigma_+(k, \omega)])^2 + Im[\Sigma_+(k, \omega)]^2} \tag{4.21}$$

  and similarly for $A_-(k, \omega)$, where $\omega_\pm(k) = \pm|k|$. ARPES is a widely used technique in condensed matter, and in particular we will mention several studies performed in graphene to compare our results with them.

After this summary, we are now ready to begin our study of the spectral properties of graphene in the presence of Coulomb impurities.

4.4 Method

For the purposes described, we will use a Dirac Hamiltonian of the form (4.10)

$$H = \int d^2x \left[\psi^\dagger \boldsymbol{\sigma} \boldsymbol{\partial} \psi + \psi^\dagger V \psi \right], \tag{4.22}$$

where we only include the potential for screened Coulomb impurities

$$V_0(r) = \sum_i^{N_{imp}} e^{i(r - R_i)q} V_C(q) \tag{4.23}$$

with V_C given by

$$V_C(q) = \frac{2\pi e^2}{\kappa\epsilon(q)}\frac{1}{q}. \tag{4.24}$$

and the RPA dielectric function given by (4.8) and (4.9) (For comparison, we will also use the Thomas-Fermi dielectric function, which as we said is just the low q limit of (4.9)). We average over the position of the N_{imp} impurities as described in section 4.1,

$$n_{imp} = N_{imp}/L^2 \tag{4.25}$$

being thus the density. We will work at a finite electronic density n, which defines the Fermi wavevector

$$k_F = (n\pi)^{1/2}. \tag{4.26}$$

After disorder averaging, we can compute the self-energy in the SCBA, which, as disussed previously, assumes weak potential (Born) and $E_F\tau >> 1$ (self-consistency). We will use band-indexed Green's functions , so that we have to compute two self-energies $\Sigma_{+,-}$. The SCBA equations equivalent to (4.4) in graphene read

$$\Sigma_+(k,\omega) = n_{imp}\int \frac{d^2k'}{(2\pi)^2}\left[V_C(k-k')\right]^2\left[\frac{1+\cos\theta}{\omega - v_F k' - \Sigma_+(\omega,k')} + \frac{1-\cos\theta}{\omega + v_F k' - \Sigma_-(\omega,k')}\right] \tag{4.27}$$

$$\Sigma_-(k,\omega) = n_{imp}\int \frac{d^2k'}{(2\pi)^2}\left[V_C(k-k')\right]^2\left[\frac{1-\cos\theta}{\omega - v_F k' - \Sigma_+(\omega,k')} + \frac{1+\cos\theta}{\omega + v_F k' - \Sigma_-(\omega,k')}\right]. \tag{4.28}$$

These are two self-consistent equations that have to be solved numerically by iteration. Note that this sets of equations imply

$$\Sigma_+(k,\omega) = -\Sigma_-^*(k,-\omega) \tag{4.29}$$

$$\Sigma_-(k,\omega) = -\Sigma_+^*(k,-\omega), \tag{4.30}$$

which just means that the self-energies for the upper and lower bands are related, a consequence of the preservation of electron-hole symmetry. For the purpose of numerical computations, it is useful to write the previous equations in terms of dimensionless variables, dividing all quantities by the Fermi energy or wavevector

$$\tilde{\Sigma}_+(\tilde{\omega},\tilde{k}) = \tilde{n}_{imp}\alpha^2\int_0^{\tilde{\Lambda}}\tilde{k}'d\tilde{k}'d\theta\left[V_C(\tilde{k}-\tilde{k}',\tilde{q}_{TF})\right]^2\left[\frac{1+\cos\theta}{\tilde{\omega}-\tilde{k}'-\tilde{\Sigma}_+(\tilde{\omega},\tilde{k}')} + \frac{1-\cos\theta}{\tilde{\omega}+\tilde{k}'-\tilde{\Sigma}_-(\tilde{\omega},\tilde{k}')}\right], \tag{4.31}$$

where the tilde denotes the dimensionless corresponding quantity, and the same applies for Σ_-. The first order Born can be obtained from this expression by taking the effective parameter $\tilde{n}_{imp}\alpha^2 \to 0$, and therefore we will define a crossover scale in momentum

$$k_F^* = \alpha \sqrt{n_{imp}} \tag{4.32}$$

below which the SCBA should start to become important.

Due to the k-dependence of the impurity potential, the solution of this equation requires to discretize the modulus of the momentum, and iterate the integral numerically until some error bound is reached. It is unfortunate that the q-space lattice has to be kept fixed so the self-energy from one iteration can be fed to the next one, because only the most rudimentary algorithms for numerical integration, such as the Simpson rule, can be used. (Interpolating in k-space at each step allowed for more efficient integration algorithms, but the overall performance of this strategy turned out to be worse than the simple Simpson rule)

This numeric solution to the SCBA equation is powerful because it uncovers the functional dependence of the self-energy on frequency and momentum, but it has some limitations. For the integration in k-space to be reliable, the step in the discretization has to be much smaller than the imaginary part of the self-energy, because this determines the size over which the function to integrate is significantly different from zero, and this area has to be covered by many steps. Since computing time increases dramatically with the number of steps, this sets a practical limitation to the lowest value of n_{imp}/n to which we have access, which is of the order of 0.1. For smaller values the interpolating method could have represented an advantage, but in this regime the difference between the SCBA and the first Born result becomes negligible, as explained previously in this section.

4.5 Results

We now present the results for the spectral properties computed from (4.27). In fig. 4.4, we show the imaginary part of the on-shell self energy for different values of the impurity concentration (thick blue lines). On-shell means here that the self-energy has been evaluated in the renormalized dispersion relation $\Sigma(\omega_R(k), k)$, which is produced by the real part of the self-energy. The red lines represent the same quantity but obtained by solving (4.27) with the simpler Thomas-Fermi dielectric function, instead of the full polarization (4.9). It can be seen that the results are similar, but the differences are large enough to conclude that a reliable calculation requires the full polarization to be used. The dashed lines are the corresponding on-shell self-energies computed with the bare dispersion relation. While using the renormalized dispersion relation is the correct procedure, we realize that the difference is not very relevant at low energies. At higher energies, however, it becomes significant, a fact that can also be observed in a slight bending of the spectral lines in the intensity ARPES plots, fig. 4.9, to be discussed below. The on-shell imaginary self-energy is seen to develop a non-zero value for electronic densities corresponding to $k_F < k_F^*$, as expected on general grounds from the SCBA.

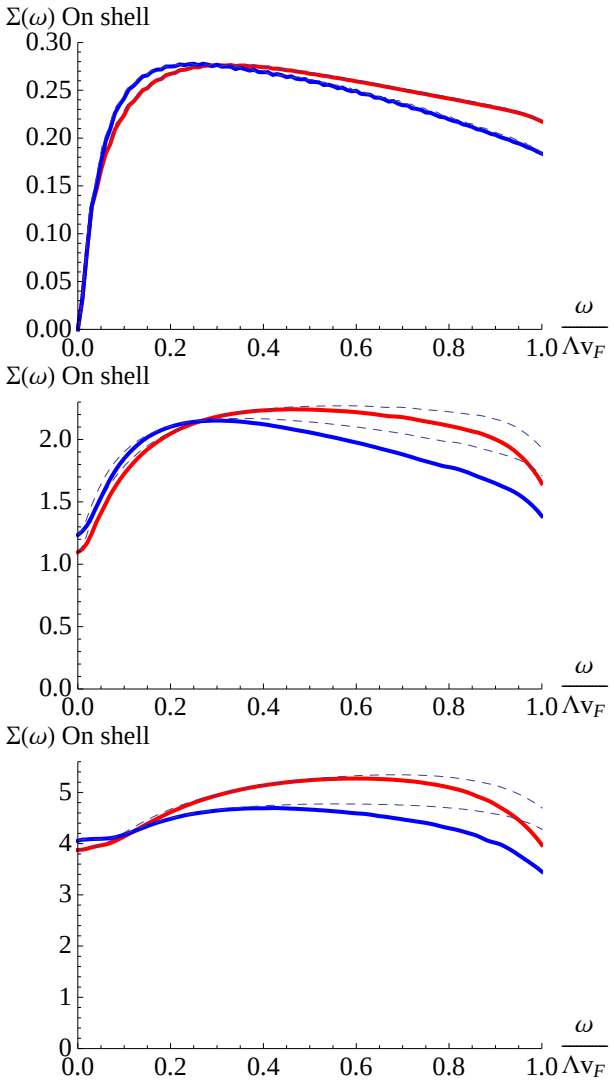

Figure 4.4: On-shell imaginary part of the self-energy, for increasing values of impurity concentration, $n_{imp} = 10^{12}, 10 \cdot 10^{12}, 30 \cdot 10^{12}$ cm^{-2}, from left to right. The thick blue line is the on-shell self-energy computed with the renormalized dispersion relation, and the red is the same for the TF model. The dashed lines have been computed with the bare dispersion relation for comparison.

A significant non-zero value is also observed in the zero energy density of states, fig. 4.5, which is computed in the standard form (4.19). In this sense, the density of states would seem to behave like the short range case. However, by comparing the two plots we also see that the DOS doesn't scale like the cutoff, but rather like the Fermi momentum. We will comment on this in the discussion section. The imaginary part of the on-shell self-energy at the Fermi level provides the one particle relaxation time τ_e. Fig. 4.6 shows a plot of the dependency of τ_e with the Fermi level k_F (dashed line) and the first order Born prediction (4.18) (full line). For each concentration of impurities, the crossover scale $k_F^* = \alpha\sqrt{n_{imp}}$ which separates

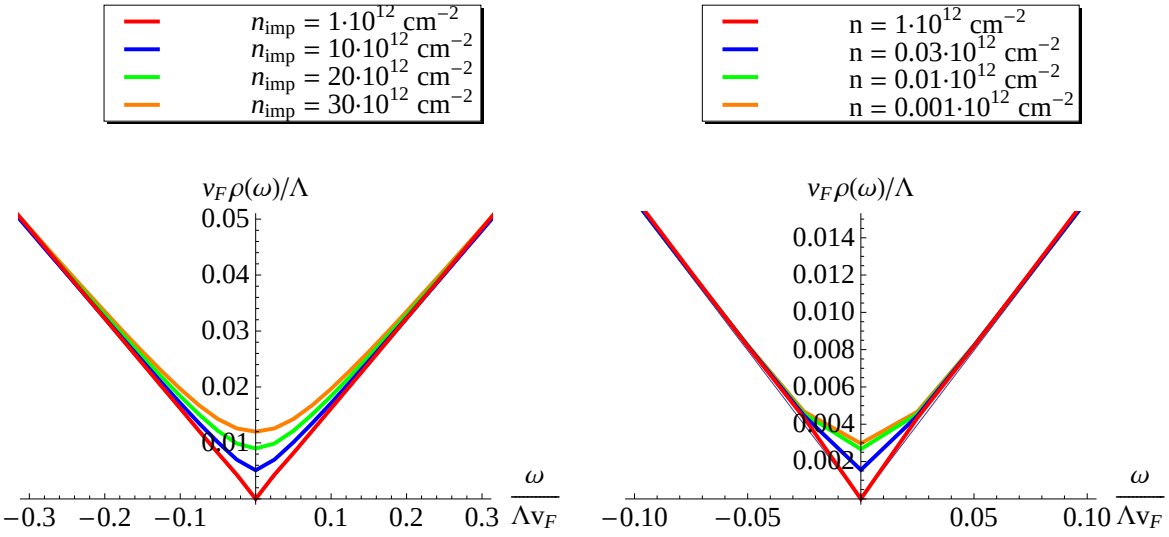

Figure 4.5: Densities of states as a function of energy. Left: For a fixed doping, varying the concentration of impurities. Right: For a fixed concentration of impurities, varying the doping.

the high and low doping region is plotted as a horizontal line. We clearly see that in the high doping region, the SCBA is indistinguishable from the first order result, a fact expected from the previous discussion. We also see how in the low doping region, deviations from the first order start to appear. Although deviations of this type are natural and expected in this region, one should keep in mind that one is formally taking the theory beyond its theoretical range of applicability. (As we explained in the previous section, both linear/independent screening and the SCBA are high density approximations) Finally, we show the results for the spectral function. Here we show first the momentum and energy distribution curves in fig. 4.7, for $n = 10^{12}$ and $n_{imp} = 10^{12}, 10 \cdot 10^{12}$. We observe the typical broadening of the quasiparticle peaks due to disorder. The intensity plots in fig. 4.9 summarize both graphs, and show very clearly the straight spectral line characteristic of the linear dispersion of Dirac fermions, broadened again by the imaginary part of the self-energy. Note that the intensity scale is the same for all three plots, and for this reason in the two first figures intensity values over 0.5 have been clipped and are represented in white for clarity. Intensity plots have been measured in several ARPES experiments [192–194, 27], and the broadened linear dispersion is observed, as we can see in fig. 4.8, consistent with our results.

4.6 Discussion

We now comment on the results obtained and on their relation to other works. The self-energies for disordered graphene have been computed explicitly in the SCBA (and SCTM) for short range disorder for example in[176, 174], and for the Coulomb case only to first

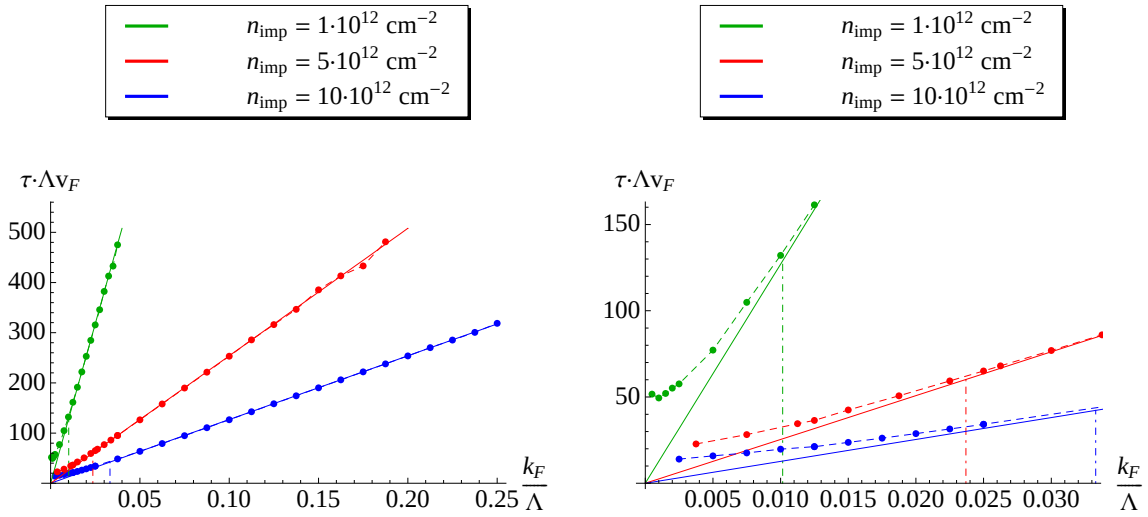

Figure 4.6: a) One particle lifetime as a function of k_F, for different impurity concentrations. The full line is the first order prediction given by (4.18). The dashed line is a guide to the eye. A horizontal dotted-dashed line is plotted at the threshold value $k_F^* = \alpha\sqrt{n_{imp}}$ for each n_{imp}. b) Same plot zoomed in the low doping region, where the SCBA effect becomes important.

order [176]. Our self-energies agree well with these first order results when the impurity concentration is low, and improve on them by showing that when $k_F < k_F^*$ a finite value of the imaginary self-energy appears at zero energy. This is also consistent with the short range case at the SCBA level. It is worth noting that the SCTM results are somewhat different than SCBA, so it would be interesting to compute the self-energy for Coulomb scatterers also in SCTM.

The densities of states obtained are also similar to what is obtained for the short range case (and also to finite size numerical calculations of the Coulomb case [181]), and one could be led to think that the screened Coulomb impurities are actually closer to being short ranged than long-ranged. Regarding this issue, it is interesting to discuss the dependency of the DOS with doping and impurity concentration. In particular, we are interested to see if the zero energy density of states is proportional to the cut-off, like in the short range case (4.17). For this purpose, we note that the self-energy satisfies the following scaling equation

$$\Sigma(a^2 n, a^2 n_{imp}, a\Lambda, a\omega, ak) = a\Sigma(n, n_{imp}, \Lambda, \omega, k), \tag{4.33}$$

which implies for the density of states

$$\rho(a^2 n, a^2 n_{imp}, \Lambda) = a\Sigma(n, n_{imp}, \Lambda/a). \tag{4.34}$$

Therefore, if the zero energy DOS were given by an expression similar to (4.17), then the quantity ρ/Λ, as plotted in fig. 4.5, should stay constant under a simultaneous change of n

and n_{imp}. We see that it clearly doesn't, concluding that the Coulomb case is different from the short range case in that the cut-off does not give the scale of the zero energy DOS.

The one-particle lifetimes are also worth looking at. We have seen there are two well differentiated regimes, separated by the crossover scale k_F^*, which determines to what extent the SCBA differs from the first order result. It is a good consistency test to check that for $k_F > k_F^*$, our numerical integration results match perfectly with the first order prediction (4.18). This allows to see clearly the deviation from linearity when the disorder gets larger. This deviation is characteristic of Coulomb impurities, and will make the quotient τ_{tr}/τ_{1p} to deviate from its constant value at dopings lower than the scale k_F^*.

The ARPES plots, on the other hand, are not such a good tool to determine the kind of disorder present in a sample, since the kind of plots in fig. 4.9 are rather generic for any type of disorder. In this plots we have observed a slight bending of the spectral line denoting renormalization of the dispersion relation, but since it gets more prononced close to the cut-off, this could very well be an artifact of the calculation and should be studied more carefully.

Summarizing, the results of our work have shown the changes produced in the spectral properties by Coulomb impurities, when their strength is such that a first order calculation is not enough, identifying the parameter k_F^* that determines quantitatively when this happens. We found noticeable effects appeared in the DOS and in the on-shell self-energy. A comment on the applicability of our approximations is in order . First, we should always keep in mind that we are using a linear RPA screening model, which will break down at low dopings, although it is difficult to quantify when. The assumption of independent screening also fails if $n << n_{imp}$. Moreover, the SCBA also requires that $E_F\tau$ be bigger than one. Many examples are known of approximations that give good results beyond their regime of applicability, so our predictions at low dopings should be considered as a hint of the effects of disorder in this regime, which should eventually be confronted with experiment.

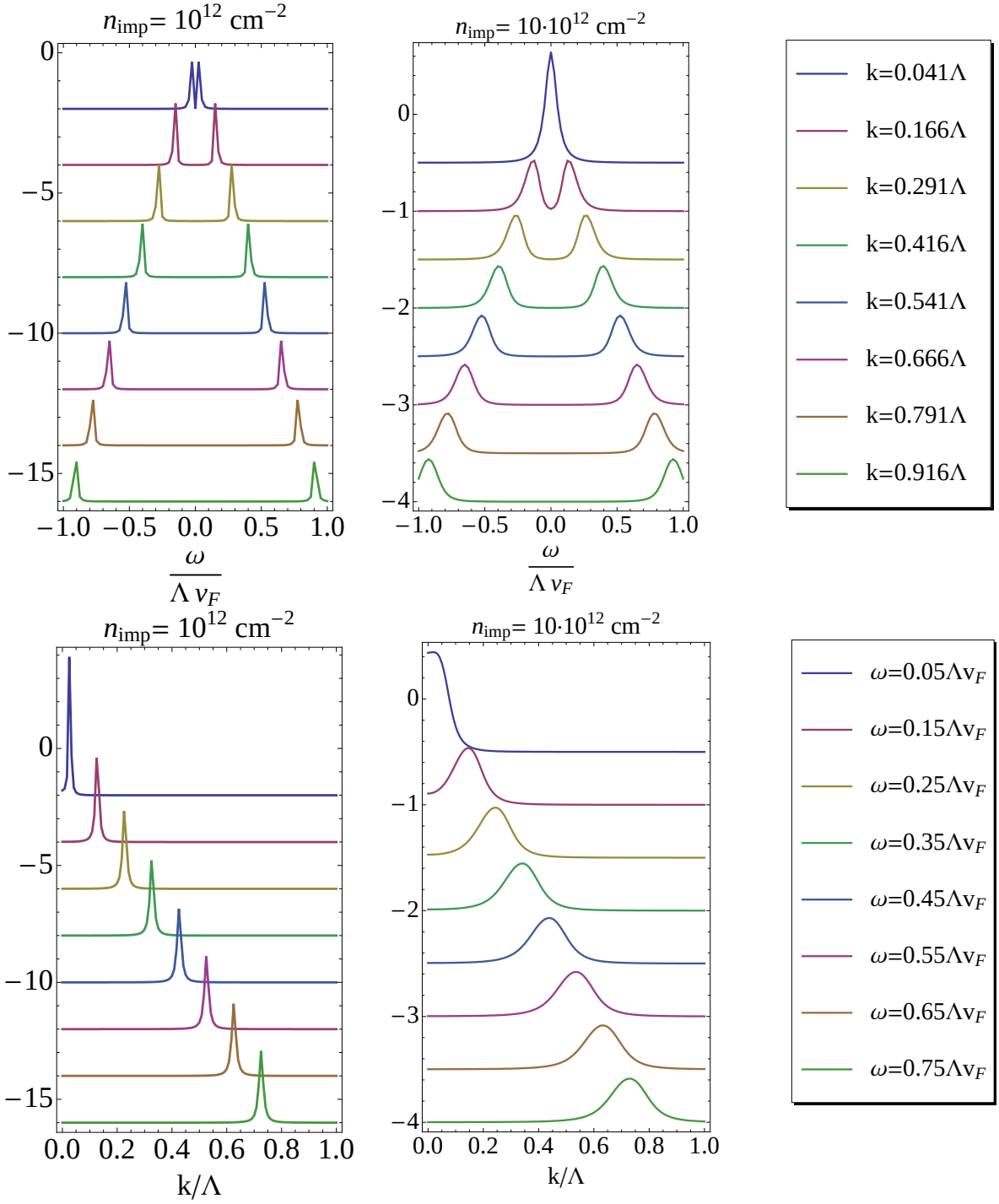

Figure 4.7: a) EDC for two values of impurity concentration, at a fixed doping of 10^{12} for two values of the impurity concentration $n_{imp} = 10^{12}\ 10 \cdot 10^{12}$ cm^{-2}. b) MDCs for the same parameters. Note the change in absolute scale from left to right.

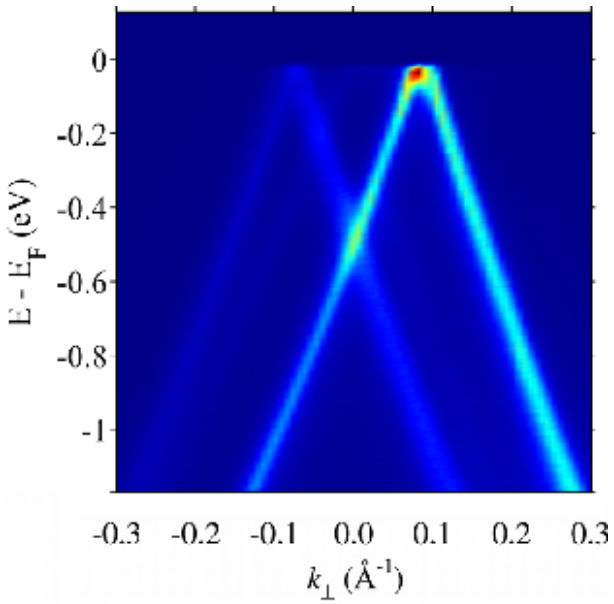

Figure 4.8: ARPES intensity plot of the spectral function of graphene, obtained from a multilayer sample where the layers are almost decoupled, see [27]

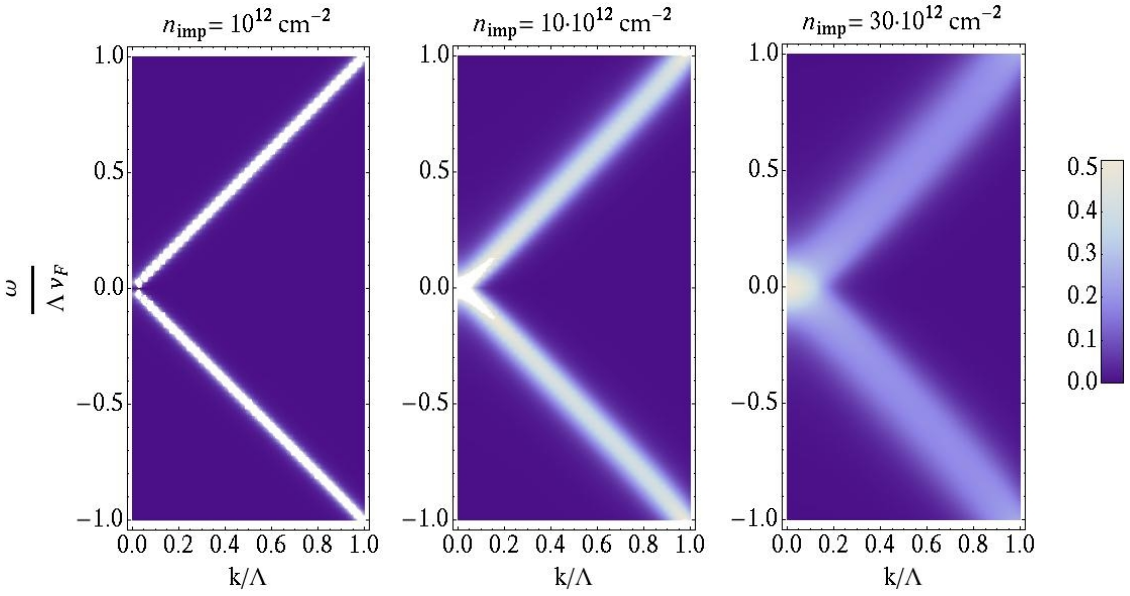

Figure 4.9: Intensity of the spectral function for $n = 10^{12}$ cm^{-2} and $n_{imp} = 10^{12}, 10 \cdot 10^{12}, 30 \cdot 10^{12}$ cm^{-2}.

5 Coulomb interactions and renormalization in graphene

In this chapter, we will address the effects of electron-electron interactions in the physics of graphene. Our discussion will be based on the ideas of perturbative renormalization, with a strong focus on the computation of physical observables and their relation to experiments.

We will first present an introduction to these topics in section 5.1. Section 5.2 will be devoted to a general analysis of the role of interactions in graphene and the setup of the appropriate renormalized field theory. Its connection with experiments will be discussed in section 5.3, and a general discussion section is presented in section 5.4. Several issues relevant to the process of renormalization and not discussed in the main body of the chapter are commented in section 5.5.

5.1 Interactions and renormalization in field theories

The problem of interactions in many-body quantum systems is a vast and complex area of research. Systems with macroscopic numbers of interacting particles are the subject of study of many branches of physics. Interactions in such Condensed Matter systems lead to a rich variety of behaviours, from the apparent absence of many-body features in systems expected to have them, to exotic states of matter bearing absolutely no resemblance to their non-interacting counterparts. Some of these systems are by now well understood, while others remain at the frontiers of research.

Many are as well the different methods that have been devised to tackle this problem under this variety of circumstances. While a comprehensive review of the issue is clearly outside of the scope of this chapter, it is fair to say, however, that a coherent picture of the problem has emerged since the development of the ideas of the renormalization group and effective theories, which have provided a unified scheme to describe many-body systems [195]. The key idea of this approach is to think in terms of the energy scales of the problem. If we are interested in the low energy physics of our system, this method allows us to obtain effective theories for the low energy degrees of freedom by systematically integrating out the high energy sector of the theory in a controlled way. In general it allows us to identify the relevant degrees of freedom as we proceed from one scale to the next, in what is called the "flow" of the theory under the renormalization group. This idea first originated in the context of statistical physics and theories of phase transitions and critical phenomena [196],

put forward by the pioneering works of Wilson [197], but the scope of its application has widened greatly ever since.

To give a more precise meaning of these ideas, it is instructive to analyze them also in another branch of physics where they have played a major role, the field of high energy physics. In paralell with the developments in statistical physics, a different problem was being addressed in this field whose solution turned out to be related to them. In high energy physics, renormalization [198, 199] started as a way to make meaningful the predictions of quantum field theories, in which fluctuations of the fields at arbitrarily short distances, or equivalently high momenta, seemed to make the physical predictions of these theories diverge with the high energy cutoff, when sent to infinity. (And even if there was some reason to keep the cutoff finite, its arbitrary value spoiled in any case the predictability of the theory).

The solution to the problem was to realize that the parameters in the Lagrangians of these theories were not directly observable, and could contain divergences. These parameters should be used to match some well chosen predictions of the theory with their experimental values, and it was shown that this cancelled the divergences in the process. After this had been done, all other observables could be accurately computed, and were made by construction independent of the cutoff, which could then be sent to infinity[1]

The theory defined in this way was known as a renormalized theory. Nevertheless, not all theories could be "fixed" in this way, so those who could be were termed renormalizable. For renormalizable theories, it was proven that the same physical predictions were obtained independently of the experimental inputs chosen, and in particular, of the scale chosen to measure them. Non-renormalizable theories seemed to require an infinite number of measurements to be fixed, apparently losing their predictive power.

Although the procedure of renormalization was initially devised to get rid of the infinities, in the modern view it is reinterpreted as the way of defining the effective parameters of the theory at a given scale. In this sense, all field theories are considered effective [200–202], because to describe the theory at a certain scale, the knowledge of the higher energy scales of the problem is unnecessary. It only influences the physics through the values of the parameters, which can be measured at the scale of interest.

In the condensed matter electronic problem, we will find that the situation is very similar to this. We will see how graphene can be described by a renormalizable theory, and our methods will paralell those employed in high energy physics. Because of this, in the next section we will cover in great detail how this procedure is carried out in practice in the case of high energy physics, preparing the ground for its applications to the case of graphene, which we will address in section 5.2.

[1] A very good review emphasizing this point of view is that by LePage [200]. This seemingly inocuous idea involves highly technical computations in practical terms, however. These are relevant to the development of the chapter and will be covered in the next section.

5.1.1 Renormalizable theories in high energy physics

In this section, we will discuss how experiments in high energy physics are described in terms of an interacting quantum field theory. We take the example of Quantum Electrodynamics (QED) as a reference, since it contains everything that will be needed to discuss the renormalized field theory for graphene. The QED example is covered in almost all textbooks on QFT, see for example [203, 199, 204].

This model contains just two types of fields, the electron field ψ and the photon A^μ. The model therefore describes two kinds of particles, and the physical observables that it can predict are scattering cross sections involving these particles. The purpose of this section is to show how these observables are computed and how they are related to experiments.

A quantum field theory is defined by a Lagrangian, which governs the dynamics of the fields. Scattering cross sections can be obtained from the Green's functions of the theory, which are in turn computed perturbatively from the Lagrangian by means of Feynman diagrams. In the case of QED, this Lagrangian is

$$\mathcal{L} = \bar{\psi}\gamma^\mu\partial_\mu\psi + m^2\bar{\psi}\psi - e\bar{\psi}\gamma^\mu\psi A_\mu + \frac{1}{4}(F^{\mu\nu})^2. \tag{5.1}$$

where ψ and A_μ are the electron and photon bare fields, and e and m the bare electron charge and the bare mass.

When computing the Green's functions of the theory, one immediately realizes that most Feynman diagrams are divergent. The diagrams are computed as integrals in momentum space, which give divergent results when the limits of integration are sent to infinity. For example, the vertex Green's function $\Gamma^\mu =< A^\mu\bar{\psi}\psi >$ which is related to Compton scattering, $e\gamma \to e\gamma$, to first order in perturbation theory is [204]

$$\Gamma^\mu(p,p') = -e^2\int \frac{d^4k}{(2\pi)^4}\frac{g_{\nu\rho}}{(k-p)^2}\gamma^\nu\frac{\not{k}+\not{p}-\not{p}'+m}{(k+p-p')^2-m^2}\gamma^\mu\frac{\not{k}+m}{k^2-m^2}\gamma^\rho \approx \int^\Lambda \frac{d^4k}{k^4} \approx \log\Lambda, \tag{5.2}$$

where Λ is an ultraviolet cutoff and $\not{k}$ is the Feynman notation for $\not{k} = k_\mu\gamma^\mu$. Physical observables cannot of course be infinity, and the procedure of renormalization was initially developed to make sense of these divergences. The solution to the problem is that the theory does make sense if the parameters in the Lagrangian are adjusted so that the Green's functions match some observables measured experimentally. This means that the bare parameters depend on the cutoff in such a way that the observables come out cutoff independent. Of course, while this idea can be expressed in a simple way, how this procedure works in practice is a complicated matter. We will therefore first show how the particular case of the renormalization of the vertex is carried out to the end, and then discuss how the procedure is implemented consistently for the whole theory to arbitrary order. The vertex calculation is discussed in detail in [203, 204].

Computing an observable

The vertex calculation we have just shown is directly related to experiments, but it contains a logarithmic divergence, as well as two undetermined parameters e and m. For an on-shell electron, the result of (5.2) can be written in the Gordon decomposition:

$$\Gamma^{\mu}(p',p) = e\left[\gamma^{\mu}F_1(q^2) + \frac{i\sigma^{\mu\nu}q_{\nu}}{2m}F_2(q^2)\right], \tag{5.3}$$

where $q = p - p'$, $\sigma^{\mu\nu} = i/2[\gamma^{\mu},\gamma^{\nu}]$ and the functions F_1 and F_2 are obtained from the direct computation of (5.2). In particular, the logarithmic divergence appears in

$$F_1(q=0) = 1 + be^2\log\Lambda \tag{5.4}$$

with b a numerical constant. This problem is solved by adjusting the unknown parameter e so that the prediction of (5.3) matches an experiment.

This experiment can be taken to be Compton scattering, where light is scattered off an electron. Obtaining the Compton cross section from the vertex (5.3) requires a few more steps, but to illustrate our point it is convenient just to assume that this experiment measures $\Gamma^{\mu}(q=0)$ directly [2]. The result of this experiment is $\Gamma^{\mu} = e_R\gamma^{\mu}$, with $e_R = 1.6\cdot 10^{-19}C$, the usual charge of the electron. Therefore, we now fix

$$\Gamma^{\mu}(q=0) = e\gamma^{\mu}(1 + be^2\log\Lambda) = e_R\gamma^{\mu}, \tag{5.5}$$

which, to first order in perturbation theory, implies that $e = e_R - e_R^3 b\log\Lambda$, and the divergence is cancelled. After this is done, we have a renormalized vertex function which can now be used to predict, for example, the anomalous magnetic moment of the electron, related to $F_2(q=0)$. This will be a power series in e, which can be computed to arbitrary precision by taking as many terms as we need, and compared to experiment. The bottom line of this example is that the problem of infinities is solved when the bare parameters of the Lagrangian are matched to experimental measurements.

Of course, this is one particular example, and it is much harder to show that this procedure actually works for all Green's functions at any order in perturbation theory. For example, the mass is still undefined in this computation, and we will need another experimental input to fix it. (This is required to compute the magnetic moment of the electron, for example)

In the next section will show how to perform this process systematically. We will see that a finite number of experimental inputs suffices to make the theory well defined at any order in perturbation theory.

Choosing to match the vertex function at zero momentum with the Compton scattering experiment is an arbitrary choice, and we could have fixed the value of the charge by any

[2] Several fine points arise in this computation, in particular due to infrared divergences, but they are inessential to the point explained. See for example [203, 204] for further details.

other experiment. The choice of the way in which we match the predictions of the theory with the experiments to fix the parameters is known as the renormalization scheme, and the one we have used is known as the on-shell scheme. The theory will give the same physical predictions for any scheme, a non-trivial issue to be discussed in the next section.

Finally, we would like to remark that the well established procedure of renormalizing QED has allowed one of the most precise confrontations of a theory with experiments, and the success of the QED predictions are rather impressive[205]. Of course, our oversimplified discussion does not represent the actual way this comparison is made, because the Compton experiment does not provide a very precise measurement of α, nor does any of the simple scattering processes most directly related to the vertex, such as Möller $e^-e^- \to e^-e^-$ or Bhabha $e^-e^+ \to e^-e^+$ scattering [204]. No matter what experiment we choose, the determination of α is never exact, of course. The best determination of α actually comes from the anomalous magnetic moment of the electron, and the confrontation is performed against other independent measurements of α, which come from, for example, the muon magnetic moment, or other atomic physics experiments such as the Lamb shift, or the hydrogen hyperfine splitting. There are also some very precise measurements of α coming from condensed matter physics experiments like the quantization of conductance in the Quantum Hall Effect.

Renormalizing the theory

In the previous example, we have seen that the vertex function $\langle A_\mu \bar{\psi}\psi \rangle$ has a logarithmic divergence at first order in perturbation theory. It is also easy to see that other Green's functions such as $\langle \bar{\psi}\psi \rangle$, $\langle A_\mu A_\nu \rangle$, $\langle \bar{\psi}\psi\bar{\psi}\psi \rangle$... have divergences as well. Then it is a natural question to ask if the procedure of renormalization can be performed in a systematic way for the whole theory, such that all Green's functions are well defined at any order in perturbation theory.

While it is non trivial to prove it, the answer to this question is well known: In the case of QED it can be done, and QED is therefore known as a renormalizable theory. Since it is discussed in many textbooks, rather than focusing on why QED is renormalizable, in this section we will take this knowledge for granted and just show how the renormalization of the theory is performed from a practical point of view. This is the most relevant information that we will need for the renormalization of the graphene model.

In a renormalizable theory, it can be proven that all divergences have their origin in a finite set of primitively divergent Green's functions. A non primitively divergent Green's function will have divergences only because it contains primitively divergent Green's functions as subdiagrams. Therefore, the whole theory can be made finite by an appropriate cancellation of these primitive divergences.

The primitively divergent Green's functions of the model are identified by their superficial degree of divergence. This is defined for a particular Feynman diagram as the power M of

integration momenta in the diagram [3]. In a renormalizable theory, all the diagrams in the perturbative series for a Green's function have the same superficial degree of divergence, which can therefore be assigned to the whole Green's function (This ultimately stems from the fact that the interaction coupling of renormalizable field theory is dimensionless). A Green's function is primitively divergent if it has $M \geq 0$.

In the case of QED, there are only three primitively divergent Green's functions, shown in table 5.1 with their superficial degree of divergence: The electron propagator $G(q) \equiv \langle \bar{\psi}\psi \rangle$, the photon propagator $\Pi_{\mu\nu}(q) \equiv \langle A_\mu A_\nu \rangle$, and the vertex function $\Gamma^\mu(p, p') \equiv \langle A_\mu \bar{\psi}\psi \rangle$[4].

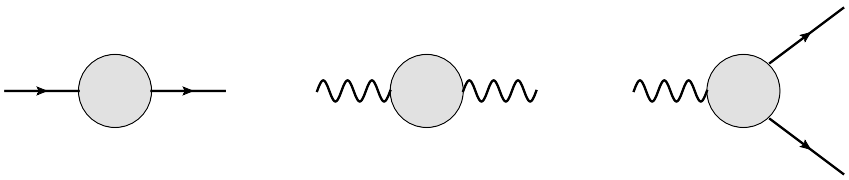

$M = 1$	$M = 2$	$M = 0$

Table 5.1: Primitively divergent Green's functions in QED, and their superficial degree of divergence M.

The reason why the renormalization can be performed is that all the divergences to be found in these Green's functions have the form of the operators that are present in the Lagrangian. These divergences are of the types we now describe.

First there are the divergences in the vertex function, which are dealt with as explained in the previous section. Then, there are two types of divergences in the two point electron function $G(q)$. The first has the form $\approx m \log^n \Lambda$ and it is easy to show that it can be cancelled in the same way as the one in the electron vertex by fixing the value of the bare mass m with another experimental input.

The second type of divergence has the form $\gamma^\mu q_\mu \log^n \Lambda$. Since the normalization of the fields was also undefined, this divergence can be cancelled by defining a renormalized field $\psi = Z_\psi^{1/2}(\Lambda)\psi_R$. The value of Z_ψ is also fixed by a renormalization condition, but in this case it is not related to an experimental input (this fine point is explained in the next section

[3] For example, the diagram (5.2) when $q \to \infty$ contains a factor d^4q in the numerator and q^4 in the denominator. This gives $M = 0$, i.e. a logarithmic divergence.

[4] The strict analysis shows that the one, three and four-photon correlators and the vacuum bubble also have $M \geq 0$. None of them need to be considered for the renormalization of the theory [199]: The vacuum bubble is unobservable, correlators of an odd number of photons vanish by charge conjugation (Furry's theorem), and the four photon correlator is not divergent due to gauge invariance despite having $M = 0$.

on renormalization conditions). Finally, the divergences in the photon propagator are dealt with in the same way by defining $A_\mu = Z_A^{1/2} A_{\mu,R}$.

The success of the renormalization of the theory is based in the fact that all divergences can be cancelled by the Λ dependence of the bare parameters in the Lagrangian. If we had found a divergence of a different type, we would have needed to introduce new operators in the Lagrangian to cancel it, which would have required an additional experimental input. This is what happens in non-renormalizable theories: as Feynman diagrams of higher orders are evaluated, more and more interactions have to added to cancel their divergences, requiring more and more experimental inputs[5].

From the practical point of view, the procedure of renormalization just described is more conveniently performed in an alternative way. Since, as we have seen, the bare parameters have no physical significance, the procedure can be restated using only the renormalized parameters, in what is known as renormalized perturbation theory. In this approach, the Lagrangian is written in terms of the physical parameters and fields, $e_R, m_R, \psi_R, A_{R\mu}$, and the cutoff dependence is shifted to the renormalization factors Z_i, which have to be determined by matching observables with experiments. The Lagrangian is written as

$$\mathcal{L} = Z_\psi \bar{\psi}_R \gamma^\mu \partial_\mu \psi_R + Z_m m_R^2 \bar{\psi}_R \psi_R - Z_e e_R \bar{\psi}_R \gamma^\mu \psi_R A_{R\mu} + Z_A \frac{1}{4} (F_R^{\mu\nu})^2. \tag{5.6}$$

It is customary to split apart the zero order term, $Z_i = 1 + \delta_i$, so that

$$\mathcal{L} = \Big[\bar{\psi}_R \gamma^\mu \partial_\mu \psi_R + m_R^2 \bar{\psi}_R \psi_R - e_R \bar{\psi}_R \gamma^\mu \psi_R A_{R\mu} + \frac{1}{4} (F_R^{\mu\nu})^2 + \tag{5.7}$$

$$\delta_\psi \bar{\psi}_R \gamma^\mu \partial_\mu \psi_R + \delta_m m_R^2 \bar{\psi}_R \psi_R - \delta_e e_R \bar{\psi}_R \gamma^\mu \psi_R A_{R\mu} + \delta_A \frac{1}{4} (F_R^{\mu\nu})^2 \Big], \tag{5.8}$$

where δ_i are called the counterterms. These counterterms are taken as new vertices, with their own Feynman rules. The counterterms are determined order by order in perturbation theory by use of the renormalization conditions. (Since in this theory only renormalized parameters and fields appear, the subscript R is unnecessary and we will drop it from now on. This way of renormalizing the theory is more convenient in practise, but it is completely equivalent to the bare perturbation theory explained before.)

This means that the procedure of renormalization is the following. First, given the Lagrangian of the theory, the primitively divergent Green's functions are identified. They are computed in perturbation theory to a given order by means of Feynman diagrams, which have to be regulated by some method (the choice of which is inessential). To a given order, one has to add all the corresponding counterterm diagrams up to that order. The Green's

[5] This used to be considered as a problem because it seemed to make the theory unpredictive. From the modern point of view, however, this is not a problem if one is looking at the low energy properties of the theory, because the effects of the new interaction terms are supressed as powers of q/μ, where μ is the coupling constant of the interaction term. Rather than being unpredictive, non-renormalizable theories have a built in cut-off μ defining their range of applicability.

function thus computed will depend on the arbitrary counterterm generated for this last order, which is fixed by renormalization conditions. After this has been done to all primitively divergent Green's functions, all cross sections for the theory can be computed to this order.

This is the final form of the method of renormalization we will employ for the graphene model. But before turning to graphene, we now discuss in more detail what is meant by renormalization conditions and how they are used. We will show several examples discussing some fine points that will be important for the implementation of the renormalized theory for graphene to be described in the next section.

Renormalization conditions

In the previous discussion, we have only shown one specific example of a renormalization condition, in the renormalization of the vertex function, stating that equivalent conditions may be defined for all primitively divergent Green's functions. In this section we give several examples of what this conditions can be chosen to be, and their implications. We will also address the question of why the conditions of the renormalization factors Z_A, Z_ψ are not associated to physical inputs.

In the case of QED, we would seem to need four conditions, to fix the values of e, m, Z_ψ, Z_A. However gauge invariance, a symmetry of the theory, fixes Z_A in terms of e and Z_ψ, so we only need three conditions. (Moreover we could think of an extra condition fixing the photon mass to zero, but this is again protected by gauge invariance). The conditions on the electron propagator $G(q)$ can be stated alternatively in terms of its self-energy Σ, defined as $G^{-1} = G_0^{-1} - \Sigma$.

The first set of conditions we will discuss is called the on-shell scheme. These conditions define the physical mass as the location of the pole in the renormalized two-point function (with respect to p^2), fixes the residue at this point to 1, and fixes the vertex at zero momentum to be the physical charge. Mathematically, this is expressed as:

$$\Sigma(p^2 = m_{os}^2) = 0, \tag{5.9}$$

$$\frac{\partial}{\partial p^2}\Sigma(p^2)\bigg|_{p^2=m_{os}^2} = 1, \tag{5.10}$$

$$\Gamma^\mu(q = 0) = e\gamma^\mu. \tag{5.11}$$

The parameters of this scheme are directly measurable, and therefore this scheme is the most straightforward to compute observables. For massless theories, the on-shell scheme is known to produce infrared divergences, and we are forced to take the renormalization point

off-shell, so conditions of the following type are employed instead:

$$\Sigma(p^2 = M^2) = M^2 + m_2^2, \tag{5.12}$$

$$\frac{\partial}{\partial p^2}\Sigma(p^2)\bigg|_{p^2=M^2} = 1, \tag{5.13}$$

$$\Gamma^\mu(q^2 = M^2) = e_M\gamma^\mu. \tag{5.14}$$

Because the substraction point is off-shell, parameters in this scheme cannot be associated directly to physical measurements. (Of course, they are ultimately related to them, only in a more indirect way). Finally, there exists another common set of conditions known as minimal substraction. In this prescription, usually combined with dimensional regularization, the renormalized Green's functions are obtained by substracting just the divergent parts of the diagrams. This prescription does not associate the substraction with a particular point in momentum space, but depends instead on an arbitrary scale μ. As in the off-shell case, the relation with experiments is more complex in this case.

Another point that we want to comment on is the fact that the renormalization factor Z_ψ is fixed by a renormalization condition that does not require an external experimental input. Instead the condition is taken to be that the pole of the electron propagator is set to 1. Why is this so? The answer comes from a point that we have overlooked in our simplified discussion, the computation of cross sections from Green's functions.

Cross sections are obtained from S-Matrix elements, which are in turn obtained from the one-particle irreducible (1PI) amputated Green's functions $\Gamma_0^{(n)}$ of the model by means of the LSZ reduction formula

$$< p_1, p_2 ... S ... k_1, k_2 >= R_{os}^{n/2}\Gamma_0^{(n)}(p_1, p_2 ... k_1, k_2), \tag{5.15}$$

where R_{os} is the residue of the bare two point function at its pole in p^2. It can be shown that the presence of this factor makes the scattering cross sections independent of the residue of renormalized two point function. This arbitrary value cancels from physical predictions, and can be set to one for simplicity [203, 198]. This cancellation also holds if we use a different prescription, as long as we arrange the correct factors for the LSZ formula [203].

We discuss this because it will be important when we go over to the condensed matter world. There, observables are not given in terms of S-matrix elements, and there is no argument to forget about the residue at the pole. This introduces the need for an extra measurement in the process of renormalization. We will also see that the equivalent of an on-shell prescription has some peculiarties as well.

Finally, we would like to remark that the definition of what the coupling constant is in particle physics is really a matter of choice. We call coupling constant to a number defined by a particular set of renormalization conditions at a particular scale. Two definitions of g

will have different values, but the observables predicted with them will be the same[6] and we can choose the prescription we prefer.

It is interesting to note that infrared stable theories with a mass represent a special class of theories in this sense, because these theories have a well defined low energy limit which is traditionally described in the on-shell scheme [199, 203], which therefore stands out as the preferred one (see [206] for a good discussion on this point). In QED, for example, one expects to obtain the $1/\vec{q}^2$ Coulomb repulsion for low energy electrons, and this form is only achieved in the on-shell scheme. The coupling defined in this scheme corresponds to our usual low energy notion of the charge of the electron, which is routinely measured in low energy experiments, and whose numerical value (actually, of α) is $\simeq 1/137$ (this is the one described in our example). This doesn't mean that other schemes cannot be used, even at low energy, it just means it is standard to employ the on-shell scheme to make contact with what is already known.

This neat definition of the coupling constant is a privilege of infrared stable massive theories, in the low energy limit. In a massless theory, or in a theory which is not infrared stable, the on-shell choice does not exist, and one has to define the coupling with some other prescription. This is the case in QCD, for example, where it is common to define α_S in minimal substraction, at the scale of the mass of the Z_0 boson [204]. Even in the case of QED at energies higher than the electron mass m the on-shell prescription is not very useful and the situation is very similar to that of QCD [206].

We want to emphasize this because in the case of graphene, we will find that there is no preferred scheme for the definition of the Fermi velocity, and a similar situation holds, with differences that we will comment in due time.

5.1.2 Interactions in many-body systems and renormalization

After the description of a renormalized theory in high energy physics, we are ready to see how an equivalent program can be implemented for electronic many-body systems in condensed matter. The idea is to look for the relevant degrees of freedom at low energies, propose a Lagrangian, and define its parameters by matching them to a set of experimental inputs.

For the case of the electron liquid, the effective low-energy theory was proposed long ago by Landau, and it is known as the Landau Fermi liquid. In this theory, the electron gas is described in terms of low-energy degrees of freedom with the same quantum numbers as the physical electrons, but in terms of renormalized parameters: the effective mass, the Z factor and Landau's interaction functions f. While his proposal was based only on general

[6] In practice, if the two renormalization points are very far apart, the differences will be noticeable. The strict statement is that the observables will be the same after the series of logarithms has been resummed, see section 5.5.2.

intuitive arguments, Landau theory has been understood recently as a fixed point of the renormalization group [207].

The theory of the electron liquid can be approached from two different perspectives. One can either start from the full many-electron problem and compute the Landau parameters through a series of (generally complex) approximations, or propose it as working effective theory in which the parameters are measured. Both approaches are complementary. Of course, Landau's theory describes only a restricted class of systems. The presence of a large Fermi surface is fundamental to its applicability, and the dimensionality of the system therefore plays a very important role (Indeed, in one dimensional liquids Landau's theory does not apply. The relevant theory for these systems is known as the Luttinger liquid [208]). Moreover, it is expected to apply at temperatures far from any phase transition.

In the case of graphene, the zero density of states at the Fermi points makes the Coulomb interactions unscreened and hence the two main assumptions of the Fermi liquid, an extended Fermi surface and short range interactions, do not apply. This makes a priori uncertain if graphene will or not behave as a Fermi liquid, an issue that was addressed in the early works of ref. [147]. In the next section we will discuss what is the relevant theory, and analyze the renormalization procedure.

5.2 Interactions in graphene

The problem of interactions in graphene is a challenging one, both from the experimental and theoretical points of view. From the experimental side the situation is unclear. While in the first experiments interactions seemed to not be playing a major role [10, 25, 26], more recent experiments point towards the relevance of interactions in graphene. The recently measured fractional Quantum Hall Effect [32, 33] is the most vivid example of the latter case, but interactions have been claimed to play a role also in other experiments [194, 209–212, 109]. From the theoretical point of view, the renormalized theory for graphene was studied even before its sythesis [147, 213], and by now the literature on this topic is rather extense, see [7] and references therein. Most of the studies on this many-body problem were performed with the tools of renormalization, but the direct connection with experiments in terms of the renormalized parameters was not addressed systematically. The purpose of this chapter is to show how this can be done for the model described in [147], in analogy with the renormalized theory of QED described in section 5.1.1.

For this, we will need the Lagrangian describing electrons in graphene. It was explained in the thesis introduction that, in the absence of interactions, the symmetries of the hexagonal lattice imply that the low energy band structure of graphene can be cast in the form of a massless Dirac Hamiltonian [23, 24]. Therefore, the starting point for our theory will be the

action:

$$\mathcal{S}_{kin} = \int dt d^2x \bar{\psi}(\partial_0 \gamma^0 + v_F \gamma^i \partial_i)\psi, \tag{5.16}$$

where the parameters are to be defined in the next section. (The requisite of time reversal invariance would require us to include the two inequivalent representations of the Dirac algebra, i.e., the two valleys, but we will not consider valley mixing effects, so a two-component Dirac fermion suffices). The normalization of the spinor field is also not fixed.

Now we will introduce interactions. In the graphene model all short range interactions are irrelevant [147, 214], in the sense explained in the previous section. The only marginal interaction is the Coulomb interaction, the one we are interested in. In this model this interaction has some peculiar features, so we will discuss it at length in section 5.5.1. In this section we show that the action for the Coulomb interaction is

$$\mathcal{S}_{int} = \int d^2x d^2x' dt \frac{e^2}{4\pi\epsilon} \frac{\bar{\psi}_x \psi_x \bar{\psi}_{x'} \psi_{x'}}{|x - x'|}. \tag{5.17}$$

The strength of the Coulomb interaction is usually expressed through the dimensionless coupling

$$g = \frac{e^2}{4\pi\epsilon v}, \tag{5.18}$$

where ϵ is the dielectric constant. This is the usual interaction term employed in condensed matter systems. As explained also in section 5.5.1, the renormalization of the model is however more conveniently performed by its equivalent description in terms of a scalar gauge field, and this is the one we will use. The complete Lagrangian for the theory is shown in the next section.

5.2.1 Renormalized perturbation theory at work

We will now describe how to compute observables in a renormalized field theory for graphene. The action we will employ, which was defined in [147] and discussed in the previous section is

$$\mathcal{S} = \int d^3k \bar{\psi} Z_\psi \left[\gamma^0 \omega + v Z_V \vec{\gamma}\vec{k}\right] \psi - Z_e e \bar{\psi} \gamma^0 \psi A_0 + Z_A A_0 |k| A_0. \tag{5.19}$$

The renormalization factors Z_i are defined implicitly through the renormalization conditions and are determined order by order in perturbation theory. As in section 5.1.1, we split the counterterms as

$$\delta_\psi = Z_\psi - 1, \tag{5.20}$$

$$\delta_v = Z_\psi Z_v - 1, \tag{5.21}$$

$$\delta_e = Z_e - 1, \tag{5.22}$$

$$\delta_A = Z_A - 1. \tag{5.23}$$

Feynman rules for the graphene model		
	=	$\dfrac{i(\gamma^0\omega + v\vec{\gamma}\vec{p})}{-\omega^2 + v^2p^2 - i\epsilon}$
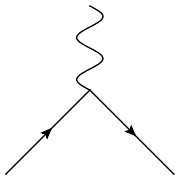	=	$-ie\gamma^0$
	=	$\dfrac{i}{2\,\lvert k\rvert}$

Table 5.2: Feynman rules associated to the graphene model, defined by the Langrangian (5.19).

Counterterm rules		
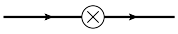	=	$-i\delta_\psi\gamma^0 k_0 - iv\delta_v\vec{\gamma}\vec{k}$
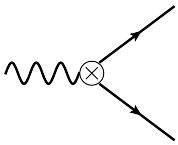	=	$-ie\delta_e\gamma^0$
	=	$-i\delta_A A_0 \lvert k\rvert A_0$

Table 5.3: Feynman rules associated to the counterterms δ_i, see eq. (5.24).

The only parameters that appear in this Lagrangian are renormalized parameters, related to experimental inputs by the renormalization conditions (when the situation requires to distinguish among different schemes, a subscript will be added, such as v_{os} in the on-shell scheme, and $v_{\overline{MS}}$ in the $\overline{MS}$ scheme). The Feynman rules for this model are the zeroth order rules given in table 5.2, plus the counterterm rules, which are obtained by considering the δ_i

as extra vertices

$$\mathcal{S} = \int d^3k\bar{\psi}\left[\gamma^0\omega + v\vec{\gamma}\vec{k}\right]\psi - e\bar{\psi}\gamma^0\psi A_0 + A_0|k|A_0 \tag{5.24}$$

$$-\delta_\psi\bar{\psi}\gamma^0\omega\psi - \bar{\psi}\delta_v v\vec{\gamma}\vec{k}\psi + \delta_e e\bar{\psi}\gamma^0\psi A_0 - \delta_A A_0|k|A_0 \tag{5.25}$$

and are given in table 5.3.

The renormalizability of this model was shown in [147]. Following section 5.1.1, the first step in the renormalization of the model is the identification of the primitively divergent Green's functions. These are depicted in table 5.4, with their corresponding superficial degree of divergence. Note that, in analogy with the QED case, we have omitted the unobservable vacuum bubble, as well as the correlators of an odd number of photon fields, which vanish by electron-hole symmetry.

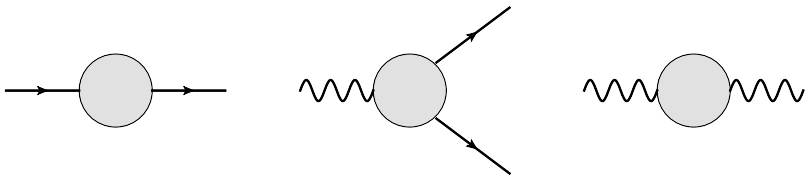

$M = 1$ $M = 0$ $M = 1$

Table 5.4: Primitively divergent Green's functions for the graphene model, and their superficial degree of divergence M. (Diagrams that vanish by electron hole symmetry are not shown)

The next step is to compute these Green's functions in perturbation theory with the Feynman rules given in tables 5.2 and 5.3, and fix the counterterms with renormalization conditions.

The renormalization conditions for the electron propagator have some particularities in this model, and therefore it is convenient to discuss them before the computation of the diagrams. We will consider two renormalization schemes, minimal substraction and on-shell scheme, to see the relation between them, and the advantages of each. These schemes were already discussed in section 5.1.1, and while the minimal substraction carries over without modification, the on-shell scheme is different and requires more explanations. For clarity in the exposition this issue has been dealt with in section 5.5.3. For the following section it is sufficient to know that we can define an on-shell prescription with just a measured point (E_R, k_R) of the dispersion relation. This observable is determined from the poles of the electron propagator, which due to the matrix structure, are the zeros of the squared inverse

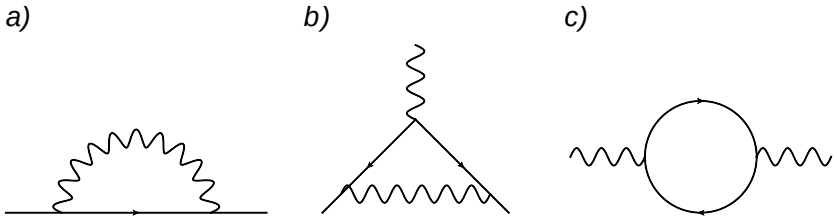

Figure 5.1: Potentially divergent diagrams at one loop order. a) Contribution to the electron propagator. b) Contribution to the vertex function. c) Contribution to the photon propagator.

propagator. Therefore, the on-shell condition is written as:

$$(G^{-1}(E_R, k_R))^2 = 0, \tag{5.26}$$

which can also be stated in the alternative way

$$G^{-1}(E_R, k_R) = \gamma^0 E_R + v_F \gamma k_R, \tag{5.27}$$

with $v_F = E_R/k_R$. This is a convenient renormalization scheme if one has access to a direct measurement of the dispersion relation, such as ARPES. In section 5.3.2 we discuss this and other possible measurements from which the Fermi velocity could be extracted.

Regarding the vertex, we will see that the electric charge does not renormalize. Therefore we will not need a condition for the vertex, and e will simply denote its bare value[7], which corresponds to $e^2/4\pi c \approx 1/137$.

After discussing the renormalization conditions, we are now ready to renormalize the theory to first order. The diagrams we have to compute are given in fig. 5.1.

5.2.2 Renormalized theory at one loop order

The electron propagator

At one loop order, the only divergent diagram for the electron propagator is given in fig. 5.1a. which has been computed in [147]. With the Feynman rules given in table 5.2, it reads

$$\Sigma^{(1)}(p) = -ie^2 \int \frac{d^3k}{(2\pi)^3} \frac{\gamma^0 \left[\gamma^0(k_0 + p_0) + v\vec{\gamma}(\vec{k} + \vec{p})\right] \gamma^0}{\left(-(k_0 + p_0)^2 + v^2(\vec{k} + \vec{p})^2\right) (\vec{k}^2)^{1/2}}. \tag{5.28}$$

Let us start with the on-shell prescription. With a sharp cutoff Λ, this diagram gives

$$\Sigma^{(1)}_{\Lambda} = -\frac{e^2}{32\pi v} v\vec{\gamma}\vec{p}(\log\frac{\Lambda^2}{p^2} + 4\log 2). \tag{5.29}$$

[7] This is a fine point which we discuss in section 5.2.3.

We observe that we find a divergence in the γ^i part, which is therefore be cancelled by a δ_v counterterm. Since there is no divergence associated to $\gamma^0 k_0$, we can set $\delta_{\psi,os} = 0 + O(e^4)$. We now have to determine δ_v according to the on-shell renormalization conditions at the point (E_R, k_R), see (5.27). We obtain

$$\delta_{v,os} = \frac{e^2}{32\pi v_P}\left(4\log 2 - \log\frac{k_R^2}{\Lambda^2}\right) + O(e^4). \tag{5.30}$$

Therefore, we obtain the following propagator to order e^2

$$G^{-1}(p) = -i\left[\gamma^0 p_0 + v_{os}\vec{\gamma}\vec{p}(1 - \frac{e^2}{32\pi v_{os}}\log\frac{p^2}{k_R^2})\right]. \tag{5.31}$$

If we had chosen the $\overline{MS}$ scheme, with dimensional regularization, we would have got

$$\Sigma^{(1)}(p) = v\vec{\gamma}\vec{p}\left[\frac{-e^2}{32\pi v}(\frac{1}{\epsilon} - \gamma + \log 4\pi - \log\frac{p^2}{\mu^2} + 4\log 2) + \delta_V\right], \tag{5.32}$$

where μ is an arbitrary scale with dimensions of momentum. The counterterm $\delta_{v,\overline{MS}}$ would be

$$\delta_{v,\overline{MS}} = \frac{e^2}{32\pi v_{\overline{MS}}}\left(\frac{1}{\epsilon} - \gamma + \log 4\pi\right), \tag{5.33}$$

which yields a renormalized inverse propagator of the form

$$G^{-1}(p) = -i\left[\gamma^0 p_0 + v_{\overline{MS}}\vec{\gamma}\vec{p}(1 - \frac{e^2}{32\pi v_{\overline{MS}}}\log\frac{p^2}{16\mu^2})\right]. \tag{5.34}$$

This prescription has the disadvantage of not being related to a particular experiment, since μ is an undetermined scale. It usually has the advantage of giving β functions independent of the mass, which is not very useful in this case.

The renormalized propagator in the on-shell scheme can be written as

$$G^{-1} = \gamma^0\omega + \bar{v}(k)\gamma^i k_i \tag{5.35}$$

in terms of a k dependent (running) Fermi velocity

$$\bar{v}(k) = v\left(1 - \frac{e^2}{16\pi v}\log\frac{k}{k_R}\right) \tag{5.36}$$

The implications of this will be discussed throughout the following sections.

The vertex function

The vertex function at one loop order is given by diagram in fig. 5.1b

$$\Gamma^0(p, p+q) = e^3\int\frac{d^3k}{(2\pi)^3}\frac{\gamma^0[\gamma^0 k_0 + v\vec{\gamma}\vec{k}]\gamma^0[\gamma^0(k_0+q_0) + v\vec{\gamma}(\vec{k}+\vec{q})]\gamma^0}{[-k_0^2 + v^2\vec{k}^2][-(k_0+q_0)^2 + v^2(\vec{k}+\vec{q})^2]|\vec{p}-\vec{k}|}. \tag{5.37}$$

Power counting reveals a logarithmic divergence, but the explicit calculation in both cut-off and dimensional regularization reveals that the divergence cancels. (Moreover, both methods give the same finite result after the cancellation, something we have checked by a direct calculation) This allows us to fix $\delta_e = 0 + O(e^4)$.

The photon propagator

The one loop correction to the photon propagator is given by the diagram in fig. 5.1c. The diagram has been computed in [147], and it reads

$$\Pi^{00}(q) = e^2 \int \frac{d^3k}{(2\pi)^3} \frac{\gamma^0 \left(\gamma^0 k_0 + v\vec{\gamma}\vec{k}\right) \gamma^0 \left(\gamma^0(k_0+q_0) + v\vec{\gamma}(\vec{k}+\vec{q})\right)}{(-k_0^2 + v^2k^2)(-(k_0+q_0)^2 + v^2(\vec{k}+\vec{q})^2)}. \tag{5.38}$$

The integral gives

$$\Pi^{00}(q) = -\frac{e^2}{16} \frac{q^2}{\left(-q_0^2 + v^2q^2\right)^{1/2}}, \tag{5.39}$$

which is finite. Again, this is consistent with the finiteness of both the vertex and the γ^0 part of the electron self-energy.

5.2.3 Renormalization at two loops order

The two loop electron self energy is given by the diagrams in fig. 5.2 The divergent parts

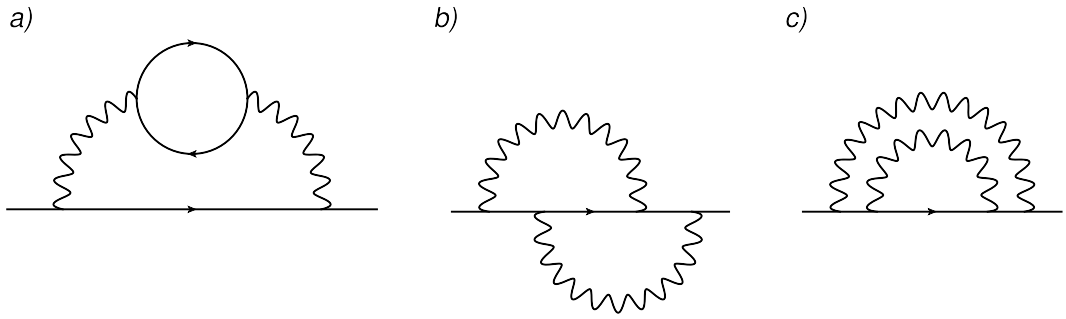

Figure 5.2: Potentially divergent diagrams at two loop order for electron self energy

of these diagrams have already been computed in the literature. For $\omega = 0$, the spatial part was computed by Mishchenko [215], showing a logarithmic divergence. The $\omega\gamma^0$ part was computed in [147], showing another logarithmic divergence. Remarkably, as we will see later, none found a $\log^2 \Lambda$ divergence. At this order, it is more complicated to disentangle the contributions of this logarithms to Z_v and Z_ψ, but it holds in general that both have a non-zero value. Therefore, we get a new contribution to the velocity renormalization, and, through Z_ψ, a non trivial scaling behaviour of the electron propagator. (However, one should look with caution to divergences in the electron propagator, which is gauge dependent. In QED, Z_ψ is logarithmically divergent in the Lorentz gauge, but the divergence cancels in the Landau gauge. [203])

The computation of the two loops vertex function is complicated, but its divergences are related to the electron Z_ψ by the Ward identity, so we will not pay further attention to it.

The relevant diagrams for the two loop photon propagator are given in fig. 5.3b and fig. 5.3c. These can be interpreted as an electron self-energy correction and a vertex correction to this propagator, respectively. The renormalization procedure requires the two loop diagrams to be computed with the set of Feynman rules containing all counterterms from previous orders. In this case, the only extra diagram to be included in the two loop photon propagator is the diagram given by fig. 5.3d.

While diagrams in fig. 5.3b and fig. 5.3d could be computed separately, it is more efficient to compute their sum, which reads

$$\Pi_{3b+3d}(q) = -e^2 \int \frac{d^3k}{(2\pi)^3}\gamma^0 G(k)\left[\Sigma_{CT} - ie^2\int \frac{d^3p}{(2\pi)^3}\gamma^0 G(k+p)\gamma^0 \frac{1}{|\vec{p}|}\right] G(k)\gamma^0 G(k+q). \tag{5.40}$$

This is so because we immediately identify the piece in brackets as the renormalized self-energy corresponding to (5.31). Therefore, the inner loop has already been computed, and what remains is

$$\frac{e^4}{32\pi v_F}\int \frac{d^3k}{(2\pi)^3}\frac{tr\gamma^0\left(\gamma^0 k_0 + v\vec{\gamma}\vec{k}\right)\vec{\gamma}\vec{k}\left(\gamma^0 k_0 + v\vec{\gamma}\vec{k}\right)\gamma^0\left(\gamma^0(k_0+q_0)+v\vec{\gamma}(\vec{k}+\vec{q})\right)\log\frac{k^2}{\mu^2}}{(-k_0^2+v^2\vec{k}^2)^2(-(k_0+q_0)^2-v^2(\vec{k}+\vec{q})^2)}. \tag{5.41}$$

The complete evaluation of this diagram is difficult without further approximation, but its potentially divergent parts can be isolated, and an explicit calculation shows that they cancel.

The vertex type correction reads

$$\Pi_{3c}(q) = \int \frac{d^3k_1 d^3k_2}{(2\pi)^6}\frac{-ie^4}{v}\frac{tr\gamma^0 G(k_1+q)\gamma^0 G(k_2+q)\gamma^0 G(k_2)\gamma^0 G(k_1)}{|\vec{k_2}-\vec{k_1}|}. \tag{5.42}$$

The first loop of this diagram is exactly the vertex (5.37), and it does not diverge. Isolating the potentially divergent parts of the full diagram, it can be seen that it does not diverge either.

In summary, this section has shown that to two loops order, divergences appear in the electron propagator only. The Fermi velocity and the electron wave function are therefore renormalized.

5.3 Observables and response functions

The previous section has focused only on the renormalization of the theory. In this section we will focus on the definition and computation of the physical observables of the renormalized theory. In particular, we will examine as an example the optical conductivity and its interaction corrections.

Up to now, the only observable that we have described is the Fermi velocity. The experiments to measure it are described in the second part of this section. But there are other

general type of observables, related to the response functions of the system. Their computation may introduce another complication in the renormalization program, because response functions are always computed as expectation values of composite operators of the field at the same point. These operators may require their own renormalization factors Z_i [216, 204], and therefore may also require an additional measurement to determine their finite parts.

The situation simplifies when computing expectation values of conserved currents, because in this case there are Ward identities that guarantee that this extra renormalization factor is 1 [216]. Conserved currents never aquire anomalous dimensions. Therefore, when deriving Kubo formulas for the response functions of conserved quantities, this problem does not appear. The response functions considered below will all come from conserved currents.

It is important to note that conserved currents in renormalized theories, as obtained by straightforward application of Noether's theorem to the renormalized Lagrangian, contain renormalization factors [217]. These are just the regular ones used in the renormalization of the theory, and have nothing to do with composite operators renormalization factors. For example, in the case of our theory, the conserved current as obtained from Noether's theorem is

$$j^\mu = (Z_\psi \bar{\psi}\gamma^0\psi, Z_\psi Z_v v \bar{\psi}\gamma^i\psi). \tag{5.43}$$

We will now derive a Kubo formula for the response of this current to an external electromagnetic field[8]. The coupling to the external field is the following

$$\mathcal{S}_{ext} = \int dt d^2x e Z_e \left[A_0^{ext} \bar{\psi}\gamma^0\psi + v Z_v A_i^{ext} \bar{\psi}\gamma^i\psi \right]. \tag{5.44}$$

A Kubo formula can be derived simply by expanding to first order in the external field [152]. Due to the fact that in this model $Z_A = 1$ always so that $Z_e = Z_\psi$, the conductivity is given by

$$\sigma^{ij}(\omega) = Z_\psi^2 Z_v^2 v^2 \frac{i}{\omega} < \bar{\psi} e\gamma^i \psi \bar{\psi} e\gamma^j \psi > . \tag{5.45}$$

This is the Kubo formula that allows to compute conductivities perturbatively (we will be interested in the longitudinal conductivity $\sigma^{11}(\omega) = \sigma^{22}(\omega) \equiv \sigma(\omega)$). An equivalent formula is usually quoted in terms of the charge-charge correlator, which can be derived by virtue of current conservation. In our case, current conservation simply gives

$$\sigma(\omega) = Z_\psi^2 \frac{i\omega}{q^2} < \bar{\psi} e\gamma^0 \psi \bar{\psi} e\gamma^0 \psi > . \tag{5.46}$$

Direct calculation shows that this is exactly the photon propagator computed previously, i.e.

$$\sigma(\omega) = \frac{i\omega}{q^2} < A_0 A_0 > \tag{5.47}$$

[8]The treatment of external fields in effective theories is dealt with, for example, in [218]

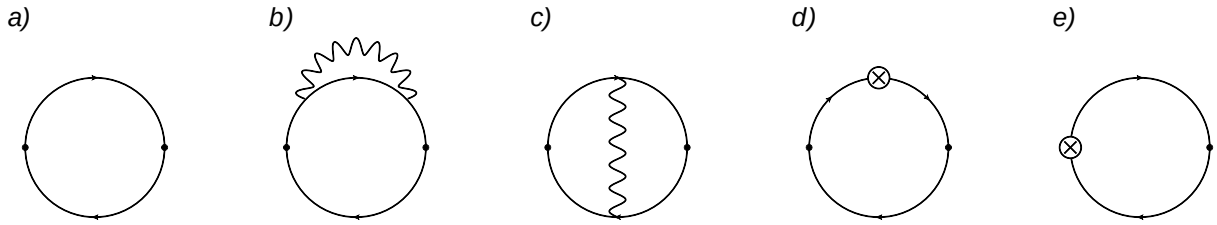

Figure 5.3: Diagrams for the conductivity. The black dots may represent charge $e\gamma^0$ or current $ev\gamma^i$ operators depending on the context, specified in the text.

5.3.1 The optical conductivity

With the expressions derived in the previous section, we can analyze the optical conductivity, which has been discussed recently in the literature [219, 42, 220]. The non-interacting conductivity can be obtained from either expression (5.45) or (5.47). This is just obtained from diagram in fig. 5.3a, where the vertices are current operators $ev\gamma^i$ for (5.45) or charge operators $e\gamma^0$ for (5.47). The non-interacting value agrees with both approaches and is given by:

$$\sigma_0(\omega) = \frac{e^2}{h}\frac{\pi}{2}. \tag{5.48}$$

The first interaction corrections can also be obtained by both the Kubo formula and the polarization method. As stated above, the polarization method just amounts to compute the photon propagator, so the conductivity is given by diagrams in figs. 5.3b, 5.3c and 5.3d with γ^0 vertices. For the Kubo formula the diagrams are the same with γ^i vertices, *plus* the corresponding counterterm coming from the Z_v factor in eq. (5.45) (The Z_ψ factor is 1 to this order) . These are denoted by diagram in fig. 5.3e. It can be checked explicitly that this counterterm cancels the divergence coming from the vertex intergral in diagram in fig. 5.3c. (This diagram diverges with γ^i vertex, but not with γ^0 vertex)

At this point, we must notice that there are no effects of renormalization to this order in the conductivity. In both the Kubo and the polarization approach, the contribution of all counterterm diagrams cancels in the imaginary part, when taking the $q \to 0$ limit. Diagram in fig. 5.3d for the polarization is simply zero in this limit, and diagrams in figs. 5.3e and 5.3d cancel each other for the Kubo approach. (This leaves two divergences in diagrams in figs. 5.3b and 5.3c that also cancel each other.) Therefore, the calculations of the optical conductivity in this approach, to this order, are exactly equivalent to those already performed in the literature [219, 42, 220]. In both Pauli-Villars and dimensional regularization, it has been shown that both the Kubo and the polarization approach give the conductivity

$$\sigma(\omega) = \sigma_0\left(1 + g\frac{19 - 6\pi}{12}\right). \tag{5.49}$$

At this point, the only effect of renormalization is the fact that the coupling constant g appearing in this formula contains v, which has to be determined experimentally. The effects of this renormalization procedure will however be relevant for the computation of the real part of the conductivity, or higher orders in perturbation theory.

5.3.2 Experiments to determine v

To be able to make physical predictions with the theory described in the section 5.2.1, we have emphasized that we need a suitable experiment to determine the value of v. The problem of determining v is essentially the same as the problem of the determination of the fine structure constant in QED described in section 5.1.1. The choice of this experiment is, in practice, not a trivial task [9]. We will now review the most relevant candidates , commenting on their adequacy to this purpose.

- **ARPES and the dispersion relation**: This is the most straightforward way of measuring v. ARPES experiments allow to map the renormalized dispersion relation, so a particular point (E_R, k_R) can be directly plugged into (5.27) to determine v. Several experiments have measured these dispersion relations [194, 193, 221, 27] under different circumstances. In fact, these experiments are also good candidates to observe the full renormalization of the Fermi velocity, but the accuracy of the measurements up to now has not been good enough to resolve it.

- **Local probes and the DOS**: Another option is to measure the total density of states as a function of the energy, which can be done with Scanning Tunneling Spectroscopy (STS) [102] or a single electron transistor [112]. This would be an indirect measurement of the Fermi velocity: the corrected DOS should be computed and fitted to the experimental one using v as a parameter.

  An alternative way consists on reconstructing the dispersion relation directly through STS, as it has been done in [105, 101]. The determination of v would proceed in the same way as in ARPES.

- **Landau levels**: In the absence of interactions, the Landau levels in a magnetic field in graphene are known to be [7]

$$E_n = v\sqrt{2eBn}, \tag{5.50}$$

  so that measuring the dependence of their position on doping n or magnetic field B could give a rather precise determination of v in the absence of interactions. Landau

[9] This experiment need not measure v directly. Any experiment measuring an observable that contains v is, in principle, just as good. Of course, the extracted value of v will depend on the approximations in the computation of the observable and the experimental errors in the measurement, thus making some methods more suitable than others.

levels have been observed with STS [222, 109] or cyclotron resonance [223] in graphene. The picture is however more complicated in the presence of interactions. A precise determination of v would require to add to the lagrangian a chemical potential and a magnetic field, to compute the energy levels corrected by interactions, and to match their positions to the experimentally measured ones using v as a fitting parameter. This method is not very suitable for our purposes, because it is not trivial that the interaction effects remain the same in the presence of a finite chemical potential. And even at zero doping, the interaction corrections to the Landau levels are complicated to compute.

- **Infrared Spectroscopy**: Another measurement has been proposed in [210] to determine the variation of the Fermi velocity, which is based on the fact that interactions lower the spectral weight in the infrared according to (5.31). If we assume that this also happens in doped samples one can expect an upward shift of the Fermi energy with respect to the non-interacting value $E_F = v\sqrt{\pi n}$. The optical conductivity measurements allow to determine E_F and n independently and measure this shift, but the problem is that computing it theoretically is very difficult. And again this has the obvious drawback that the doped system may not mantain the same interaction corrections as the doped one.

  A related optical method proposes to reconstruct the dispersion relation directly from the absorption spectrum of the sample [224]. While no doping is required in this setting, this particular experiment has the disadvantage of being performed at optical rather than infrared frequencies, so the Fermi velocity is measured at rather high energies.

In view of this discussion, the most suitable experiments both to measure the Fermi velocity and to observe its renormalization with energy are those whose measure the dispersion relation directly. This is just because the connection from the experiment to the computed observable is the simplest in this case. ARPES experiments in particular would be the ideal candidate if they had better accuracies, because they measure it for the broadest range of energies.

As a concrete example, we can take for example a point from the dispersion relation measured in [27], (E_R, k_R) = (0.1 eV, 0.016 Å^{-1}), which gives $v = 0.95 \cdot 10^6$ m/s.

We also remark that all the presented experiments have been performed in substrates of different kinds (basically SiO_2, SiC and graphite). It would be very interesting to have an experiment measuring v in a suspended sample. This would not only improve the quality of the samples, but also enhance the effects of electron-electron interactions by eliminating the screening produced by the substrate. (Optical transmission experiments have in fact been performed in suspended samples [211], but the range of energies is again optical rather than infrared and the accuracy is not too high)

5.4 Discussion

We now comment on the results shown in the previous sections. Our aim in this work was to set up a renormalized perturbation theory for graphene, so that we could evaluate the effects of interactions in this system. We have shown that, to one loop order, the theory can be fixed by the measurment of only one parameter, the Fermi velocity, which then permeates through all observables. If more precision is required, the next order in perturbation theory requires a second measurement due to wave-function renormalization. Computations to arbitrary order can be performed by fixing these two parameters.

We believe that as the experimental precision improves, the accurate determination of these observables will be important, which can only be computed with a precise measurement of the Fermi velocity. This situation is not very different from what happens with the fine structure constant in QED, as discussed in the introduction.

We have discussed possible candidates for this measurement, concluding that ARPES is the most direct way of both obtaining v and observing its renormalization. Unfortunately, the current precision of these experiments is not enough for this purpose, but it is conceivable that new experiments will improve on this, especially if ARPES is performed on suspended samples. In fact, if we assume an experimental resolution of 10 meV, and an effective coupling of order $g \lesssim 1$ (above which this description breaks down) the growth of v over two decades in energy should be

$$\frac{v(1eV)}{v(0.01eV)} \sim 2, \tag{5.51}$$

which should be observable. It will be a definite signature of the importance of interactions if the renormalization of v is observed in a clean way.

The next point we discuss is the range of validity of the model. When we discussed the Coulomb interaction in section 5.5.1, we assumed that a non-relativistic approximation could be performed, based on the smallness of the parameter v/c. We emphasized that this approximation was to be checked a posteriori, after the measurement of v. For the relevant range of energies in experiment, v seems to be of the order of 10^6 m/s, which makes this approximation justifiable. However, we have also discussed at length the renormalization of the Fermi velocity. Since the real velocity of a low-energy quasiparticle is really given by the running velocity (5.36) and not just by v, when going to low enough energies, the non-relativistic approximation may start to break down as the velocity increases. Indeed, this model does not provide any upper bound for the velocity. One can estimate a low energy cutoff for this theory by equating the running velocity (5.36) to c. This cutoff reads

$$\delta = k_R \exp\left[-\frac{16\pi(c-v)}{e^2}\right]. \tag{5.52}$$

This equation of course depends on the measured value of v at (E_R, k_R), and on (E_R, k_R) directly. With the values discussed in section 5.3.2, this cutoff has a huge exponential sup-

pression factor, so that it lies below any experimental resolution. This does not impose any real bound on the validity of the model from a experimental point of view.

Another point worth commenting is the non-renormalization of the charge in this model. We have seen this up to two loops order but, is it true in general? It has been argued [147] that it is, by the following argument. The photon propagator has a linear degree of divergence M=1, and in dimensional regularization these kind of divergences do not appear because they correspond to half integer values of Γ functions [10]. Therefore, the photon propagator cannot have divergences and the charge does not renormalize.

However, although linear divergences will not appear, charge renormalization is actually given by Z_A, which is rather obtained from terms of the type $|k|log\Lambda$, consistent with M=1. The same dimensional analysis holds actually for the electron two point function as well, where Z_v is obtained from terms $\vec{\gamma}\vec{k}\log\Lambda$. However, divergences are found in the electron propagator but not in the photon one, showing that the argument in [147] is not conclusive. Another argument has been put forward by [214], which states that for gauge type of interactions, the charge does not renormalize if the gauge field propagator is non-analytic in momentum. It would be desirable to have a more formal proof of this.

As a final remark, it is also worth recalling that our theory was derived with the assumption of no spontaneous symmetry breakdown [225, 186, 226–228]. Our theory does not rule out that this may happen if the bare theory is strongly coupled. If relaying only on perturbative calculations, this is something that has to be determined by experiments, but up to date no conclusive experiment has shown any signature of symmetry breaking and departure from the present model. It will be interesting to see how the situation develops as experiments improve.

5.5 Related issues

The main subject of this chapter has been to determine the way to evaluate the effects of electron-electron interactions in graphene through renormalized perturbation theory, focusing the discussion on the computation of physical observables and their comparison with experimental data. Therefore, throughout the chapter we have chosen to mention only in passing some issues that, while important for the understanding of the renormalized theory, did not play a fundamental role in this process of relating observables to experiments. These issues are the non-relativistic limit of the Coulomb interaction, the use of the on-shell prescription in condensed matter, and the reparametrization invariance and the β function of the model. We proceed to discuss them in the present section.

[10] A full β function being zero is of course a scheme independent fact [199]

5.5.1 The non-relativistic limit of the Coulomb interaction

In section 5.2 we stated that we would model the Coulomb interaction with the usual instantaneous potential (5.17). In this section we justify this statement and comment on several fine points regarding this interaction.

Our starting point will be to introduce the full electromagnetic interaction through minimal coupling in the model given by (5.16), in the sense of the retarded model of [147]. This assumes that the original electromagnetic interaction among the electrons remains the same in the effective model. The action for this model is

$$S = \int dtd^2x \left[\bar{\psi}(\gamma^0\partial_0 + v_F\gamma^i\partial_i)\psi + e(-\bar{\psi}\gamma^0\psi A^0 + \frac{v_F}{c}\bar{\psi}\gamma^i\psi A^i))\right]. \tag{5.53}$$

$$S_A = \frac{1}{16\pi}\int dtd^3x F^{\mu\nu}F_{\mu\nu} \tag{5.54}$$

Note that we are not using natural units for the velocities so that c appears explicitly, contrary to [147]. As explained there too, the gauge field propagates in 3+1 dimensions while the electrons live in 2+1. We have taken this route so that we can evaluate explicitly whether a non-relativistic limit is possible and under what conditions. Since (5.53) contains a velocity v that may be much smaller than c, a meaningful limit would be to drop all quantities containing powers of v_F/c. As it stands, the only approximation we can do in (5.53) is to drop the current-current interaction, which is suppressed by the dimensionless factor v_F/c with respect to the charge-charge interaction. After integrating out the scalar photon field in the Lorentz gauge, we end up with an interaction term of the form

$$\mathcal{L}_{int} = \int \rho_{\omega,k}\frac{1}{\omega^2 - c^2k^2}\rho_{-\omega,-k}. \tag{5.55}$$

This is not the usual charge-charge interaction described in condensed matter textbooks, because it is retarded. While it is tempting to drop the ω^2 in the interaction because, heuristically, c is very large, formally there is no v_F with respect to which compare. The reason why we finally end up with the instantaneous Coulomb interaction is technically different. First, suppose that we insist on keeping the longitudinal part of the current-current interaction, despite being of order v_F/c. Now split the charge-charge interaction into

$$\mathcal{L}_{int} = \int \rho_{\omega,k}[\frac{1}{\vec{k}^2} - \frac{1}{\vec{k}^2 - \omega^2}\frac{\omega^2}{\vec{k}^2}]\rho_{-\omega,-k}. \tag{5.56}$$

Then it can be proven [229] that, if the current j^μ is conserved, then for all physical amplitudes the longitudinal part cancels exactly the second term in (5.56), leaving us to all effects with an instantaneous interaction. If we had chosed to keep the scalar propagator retarded, we would have found at the end of the calculations (of gauge invariant quantities) that some extra pieces emerge proportional to v/c which should be dropped in the non-relativistic limit.

After the integration of the k_z component, we end up with the usual instantaneous model

$$\mathcal{L} = \int d^3x \left[\bar{\psi} \left(\gamma^0 \partial_0 + v_F \vec{\gamma} \vec{\partial} \right) \psi - e \bar{\psi} \gamma^0 \psi A_0 + A_0 |k| A_0 \right]. \tag{5.57}$$

That this is so can also be seen from the perspective of the Coulomb (or transverse) gauge, most commonly used in condensed matter textbooks. In this gauge, the scalar part of the interaction is automatically instantaneous (and the longitudinal part of the propagator is set to zero). In both gauges, no trace of c is found in the final lagrangian as it should be.

Finally, we comment on the apparent violation of causality implied by this instantaneous interaction. In the theory of electromagnetism ([230]), it is well known that all electromagnetic signals propagate with the velocity of light, in any gauge. While in the Coulomb gauge the scalar potential seems to be instantaneous, the electric field produced is nevertheless causal because the instantaneous part is cancelled by an opposite piece coming from the vector potential [231]. If we assume $v_F << c$, then the compensating part is neglected. This means that the interaction (5.57) *is* indeed causal but only to order v_F/c. It is only the full theory (5.53) which is causal without approximation.

We have chosen to exemplify the non-relativistic approximation in the case of graphene, but of course this approximation is commonplace in condensed matter physics. The interaction thorugh the vector potential, also known as the interaction through transverse photons, is usually neglected again because of the smallness of v_F/c [11]. It has been considered, however, because its long-range nature is protected by gauge invariance and leads to non-Fermi liquid behaviour in normal metals at low temperatures [232], such as a singular specific heat, see also [233] and references therein.

The conclusion of this appendix is that we can proceed with the instantaneous interaction (5.57), assuming that the vector part of the interaction can be neglected. Strictly, we remark once again that this is an assumption to be checked a posteriori, because, as we have seen throughout the chapter, the value of v_F is a priori not known and is fixed by experiment. Moreover, it is expected to renormalize, which means that even if we measure a small value at a certain energy, this does not mean we are allowed to neglect it for all energies.

5.5.2 Reparametrization invariance and the β function

In our discussion of renormalizable theories we have stated that the choice of renormalization point is inessential, in the sense that two different points give the same physical predictions. In this section we discuss this point and its implications.

The fact that, in a renormalizable theory, the renormalized Green's functions are invariant under simultaneous changes of the renormalization point and the running parameters of the theory is expressed by a Callan-Symanzik equation [203, 204]. By explicit use of this equation it can be shown that this invariance constrains the structure of the divergences of

[11] In typical metals this ratio is indeed small, of the order of 1/100 [70]

the theory. For example, in QED it is well known that the perturbative expansion of the fine structure constant must contain a $\log^n \Lambda$ to n loops order, and that this is a geometric series. This is known as the series of leading logarithms. The resummation of this series gives usual expression for the renormalized fine structure constant

$$\alpha(q) = \frac{\alpha(\mu)}{1 - \frac{2\alpha}{3\pi}\log\frac{q^2}{\mu^2}}, \tag{5.58}$$

which is reparametrization invariant.

In this section we will make use of this invariance in the graphene model to analyze the structure of the divergences in the perturbative series.

For the graphene model, the Callan-Symanzik equation was derived in [147]

$$\left[\mu\frac{\partial}{\partial\mu} + \mu\frac{\partial e}{\partial\mu}\frac{\partial}{\partial e} + \mu\frac{\partial v}{\partial\mu}\frac{\partial}{\partial v} - \frac{n}{2}\mu\frac{\partial\log Z_\psi}{\partial\mu}\right]\Gamma^{(n)} = 0. \tag{5.59}$$

This allows to define

$$\beta_v = \mu\frac{\partial v}{\partial\mu}, \tag{5.60}$$

$$\beta_e = \mu\frac{\partial v}{\partial e}, \tag{5.61}$$

$$\gamma_\psi = \mu\frac{\partial\log Z_\psi}{\partial\mu}. \tag{5.62}$$

As we have seen, there is no wavefunction renormalization Z_ψ to one loop order, and $\beta_e = 0$ to all orders[12]. The β function for v reads at one loop order

$$\beta_v = \frac{e^2}{16\pi}, \tag{5.63}$$

which can be integrated to give

$$v(\mu') = v(\mu) + \frac{e^2}{16\pi}\log\left(\frac{\mu}{\mu'}\right). \tag{5.64}$$

This result is what we obtained before in (5.36) with the first order Feynman diagram for the self energy identifying $\mu' = k$. However, it has been obtained by making explicit use of the reparametrization invariance of the theory, and it contains more information about the perturbative series than the one loop result. In particular, we will now see that it states that, contrary to the case of the fine structure constant, there are no more leading logarithms, this is, no $log^n\Lambda$ term appears to order n in perturbation theory. This unusual behaviour happens because the beta function at one loop is independent of v.

This fact can be seen by deriving the recursion relations among the leading log coeficients (This parallels the derivation in [199]). Consider the bare Fermi velocity in dimensional regularization. It can be written as a Laurent series in ϵ

$$v_0 = \mu^{2\epsilon}\left(v + \sum_{k=1}^{\infty}\frac{a_k(v,e)}{\epsilon^k}\right). \tag{5.65}$$

[12] See the discussion in section 5.2.3

Take the derivative with respect to μ. Since e is not renormalized, this yields

$$0 = 2\epsilon \left(v + \sum_{k=1}^{\infty} \frac{a_k(v,e)}{\epsilon^k} \right) + \mu \frac{\partial v}{\partial \mu} \left(1 + \sum_{k=1}^{\infty} \frac{a'_k(v,e)}{\epsilon^k} \right) \tag{5.66}$$

This is the usual equation that gives recursion relations among the coeficients in the logarithms, by matching powers of ϵ in the Laurent series, and which allows the resummation of the leading logarithms. (It is an equivalent statement of renormalizability).

The matching of terms to order ϵ^{-1} can be evaluated to order e^4 with the one loop calculations, yielding

$$2(a_2^0 + e^2 a_2^2 + e^4 a_2^4) = -\frac{2e^2}{32\pi} \frac{\partial}{\partial v} (a_1^0 + e^2 a_1^2), \tag{5.67}$$

where the superindex denotes the order in e. The computation to one loop shows that $a_2^0 = a_2^2 = 0$, and that the right hand side is independent of v, so this implies that

$$a_2^4 = 0, \tag{5.68}$$

this is, there is no squared log term in the two loop self-energy. This is a non-trivial implication of the renormalizability of the theory. This argument can be carried out iteratively to show that there is no log^n term at n loops, a fact has been checked explicitly to order e^4 [147, 234], as discussed in section 5.2.3. This result could have been anticipated because of the RG invariance of the theory.

5.5.3 On the on-shell prescription in condensed matter

When discussing the different renormalization schemes for the case of graphene, we just stated eq. (5.26) as the definition of the on-shell prescription without further explanation. This looks different from its high energy physics counterpart (5.9), and in particular it can be used even in the massless case. In this section we discuss these differences.

The main reason why the on-shell prescriptions differ in these cases is that Lorentz invariance does not hold in condensed matter systems. In Lorentz invariant theories, the dependence of the Green's functions on E and $\vec{p}$ appears always through the combination $p^2 = E^2 - \vec{p}^2$. The single particle pole of G with respect to p^2, located at $G^{-1}(p^2 = m^2) = 0$ actually describes all one-particle states. While the physical value of m may change with respect to the bare theory, the shape of the dispersion relation is not renormalized. This also implies that the residue of the quasiparticle pole is the same constant for all one-particle states. We note also that when this theories are massless, the on-shell prescription cannot be used, the reason being that since all diagrams must depend only on p^2, evaluating them on the mass shell $E^2 = \vec{p}^2 + m^2$ when $m = 0$ produces a singularity. An off-shell substraction point is unavoidable for these theories.

In graphene, the effective Lorentz invariance is broken by the interaction, and the "mass shell" (defined as the surface in E, p space where $G^{-1}(E,p) = 0$) is modified by interaction corrections $E = v(E, \vec{p}, e)|\vec{p}|$, with $v(E, \vec{p}, e) = v_F + O(e^2)$. Here, however, no symmetry forces the Green's functions to depend on the singular combination $E^2 - v(E, \vec{p}, e)^2\vec{p}^2$, and infrared divergences need not appear in the massless case. The on-shell prescription is consistent in this case, and measuring a single point (E_{os}, P_{os}) of the dispersion relation (from an ARPES experiment, for example) is enough to determine the parameter v_F in the Lagrangian. This was done in practice in section 5.2.1. (Of course, an off-shell substraction at an arbitrary point (E_1, p_1) can be performed as well, but the relation of v_F with the experiment becomes more complicated in this way. As we have explained in section 5.3.2, since we do have a way of measuring the dispersion relation, the on-shell prescription just described is very useful)

This on-shell prescription is different from the Lorentz invariant one because it is evaluated at a particular state (E_{os}, P_{os}), rather than for all one-particle states. This is important because it means that the residue of the pole at different one particle states depends on $\vec{p}$, while it is a constant in Lorentz invariant theories. There is no meaningful concept of *the* one-particle pole residue. There may be a particular place in the dispersion relation where we may be interested in defining the residue, for example at the Fermi surface in the Landau Fermi liquid, which defines the usual Z factor. In the case of graphene the Fermi surface reduces to a singular point where the on-shell condition cannot be applied, but any other choice of the renormalization point is allowed. Renormalizability guarantees that the observables predicted will be the same for any of them approximately, and exactly if the leading logarithms have been resummed (see previous section).

6 Conclusions and discussion

In this section we summarize the main conclusions of the work that has been presented. We comment on the most relevant results obtained and discuss some important open problems.

This thesis has addressed two of the most interesting problems in the physics of graphene. The first one is concerned with the interplay of the morphology of the samples and their electronic properties. The second is a prevalent problem in condensed matter physics that has special relevance in graphene, the problem of how to handle singular long ranged Coulomb interactions.

The structural features of graphene are essential to understand its electronic properties. Corrugations have been found experimentally in most of the samples [17, 20, 98, 19], and they have been quoted to substantially influence the transport properties [31, 116–121, 42]. In particular, they are considered as one of the possible scattering mechanisms limiting the mobility in graphene [122].

In this thesis we have proposed a model to study the smooth corrugations of the samples that predicts a new effect of the curvature: a space-dependent Fermi velocity. In this model, presented in chapter 3, electrons in corrugated graphene sheets are described by the Dirac equation in the corresponding curved background metric. This geometrical model reproduces the effective gauge field obtained in the elasticity approach [30] as the geometrical spin connection, and predicts the additional effect of the variable Fermi velocity, which has observable consquences.

This was shown by studying the case of an axially symmetric gaussian bump as an example. The local electronic density of states was computed perturbatively in a parameter measuring the deviations from flatness. The correction of the gauge field was shown to vanish, but the variable Fermi velocity (and the determinant of the metric) produces a correction which correlates with the shape of the bump. These corrections to the LDOS can be observed with STS experiments. The search of an alternative microscopic derivation for the Fermi velocity term remains a very interesting open problem, which will aquire special relevance if experiments verify the predicted correlations between LDOS and morphology.

The geometrical model proposed can also be used to describe the presence of topological defects, another perturbation to graphene's morphology. Disclinations have been modeled before as singular sources of curvature [131–133], but dislocations require another ingredient in the model: they represent sources of torsion [138, 124]. Our contribution in this work has been to set up the formalism for coupling Dirac fermions to the torsion field. More

importantly, we have shown that the use of this formalism is not limited to graphene, and it will find relevant applications to three dimensional systems containing screw dislocations and supporting Dirac fermions, in particular topological insulators [144].

Another original aspect of this work regarding topological defects, discussed in chapter 2, has been to study their effect in the magnetic properties of graphene. The magnetic ground state of the system has been shown by many studies [48–52] to conform to a robust picture given by Lieb's theorem: The total spin of the ground state is given by the sublattice imbalance. Although Lieb's theorem was proven for a bipartite lattice with Hubbard interactions only, different first principles approaches which go beyond the Hubbard model still produce results in accordance with this rule [85–87], which has become a paradigm for the study of magnetism in graphene.

Our contribution has been to test the importance of the bipartite lattice hypothesis for Lieb's rule to hold. We have shown that a single pentagonal link, that makes the lattice non-bipartite, is enough to change the ground state significantly even for clusters as large as 3200 atoms. We presented a mean field Hubbard model calculation to show that the system has Lieb's ground state for high enough U, but has a transition to a different state as U is lowered. The importance of this result lies on the fact that the type of defects discussed are very probably present in graphene, and will modify the previous estimations on the magnetism of the samples.

The second general problem addressed in this thesis concerns the long range Coulomb interactions in graphene. In condensed matter physics, the fact that the Coulomb potential does not have a scale, so that its effects extend to arbitrarily large distances, always represents a complicated problem because of infrared divergeces [153]. This problem is solved in the electron liquid by taking into account screening, but as discussed in the text the vanishing density of states in undoped graphene implies that Coulomb interactions remain truly long ranged and the non-linear screening of the Coulomb impurity problem is highly non trivial [34–37].

The infrared divergence problem is also explicit when a long range potential is taken to model random disorder in a condensed matter system [190]. In the case of graphene, long ranged charged impurities are an important scattering mechanism , but their treatment in the undoped case suffers precisely from this problem [189]. Moreover, the absence of an extended Fermi surface prevents the use of self consistent approximations, which are commonplace in the case of the regular 2DEG [153].

As a first step towards the transport properties of the system, and given the difficulty of the general problem, in chapter 4 we have addressed the effects of random charged impurities on the spectral properties of doped graphene. We have employed RPA screening for the impurities, and the self consistent Born approximation for the averaging procedure. The regime of doping where the SCBA improves on the known first order result was identified by the threshold value k_F^*. The results show that Coulomb impurities produce a finite lifetime,

linear with doping in the high doping region, but which deviates characteristically from this behaviour below the threshold k_F^*. The density of states at the Dirac point was shown to present a finite value for dopings below the threshold.

This calculation was performed assuming an RPA dielectric function, considered applicable in the high doping limit. To our knowledge, no quantitative criterion exists to decide a doping below which it becomes unreliable in graphene, and we consider this a matter which deserves further work. Also note that the SCBA considers the Born limit of weak scattering, and this work can be extended beyond this limit, for example with a self-consistent T-matrix approximation.

The last part of this thesis deals with the long range Coulomb interaction between electrons in graphene. The paradigm to describe the many-body interacting electron system in condensed matter is the Landau Fermi liquid [235], which is based on the assumptions of an extended Fermi surface and short range interactions. Both assumptions are violated in graphene. This system was studied from the perspective of the renormalization group [147] to determine its infrared nature in the early literature. The renormalization of the Fermi velocity and its running character were established in this context, but the crucial issue of computation of observables and their relation to experiments was not addressed.

The contribution of this work, presented in chapter 5, has been to discuss how observables are computed in the renormalized theory, and to show how to relate the theoretical computation with experiments to a given order in perturbation theory. We have emphasized the similarities of this problem with that of the measurement of the fine structure constant in QED [204], and we have analyzed several possible ways of measuring the parameter v.

One of the aims of the present work was to clarify the role of the cutoff in the effective quantum field theory describing the system, an issue that originated in the discussions on the Coulomb corrections to the optical conductivity [219, 42, 220]. We have shown how the renormalization procedure makes all observables cutoff independent to any order in perturbation theory, computing the first corrections to the conductivity as an example.

We also discussed the possibility to observe the running of the Fermi velocity produced by interactions in the experiments analyzed. It was suggested that the best chance to measure this effect is to study it in suspended samples, where interactions are enhanced due to the absence of screening. This would represent a distinctive signal of interactions in this system.

In summary, we have addressed two of the most important open problems in the physics of graphene, the influence of morphology and of long range interactions in the electronic properties, and we have presented our novel contributions to the understanding of these problems, and discussed their experimental implications.

7 Conclusiones y discusión

En esta sección se resumen las conclusiones principales del trabajo que se ha presentado. Se comenta sobre los resultados más relevantes obtenidos y se discuten algunos problemas abiertos importantes.

Esta tesis trata sobre dos de los problemas más importantes en la física del grafeno. El primero es la influencia de la morfología de las muestras en las propiedades electrónicas. El segundo es un problema recurrente en materia condensada que tiene especial relevancia en grafeno, el problema de cómo tratar las interacciones de largo alcance singulares.

Las características estructurales del grafeno son esenciales para entender sus propiedades electrónicas. La mayoría de experimentos en grafeno han encontrado corrugaciones [17, 20, 98, 19], y muchos trabajos han remarcado su influencia sustancial en las propiedades de transporte [31, 116–121, 42]. En particular, se consideran uno de los posibles mecanismos que limitan la movilidad en grafeno [122].

En esta tesis se ha propuesto un modelo para estudiar las corrugaciones de las muestras que predice un nuevo efecto de la curvatura: una velocidad de Fermi dependiente del punto. En este modelo, presentado en el capítulo 3, los electrones en muestras de grafeno corrugado se describen por la ecuación de Dirac en la métrica curva correspondiente. Este modelo geométrico reproduce el campo gauge efectivo que se obtiene en el formalismo de la elasticidad [30] como la conexión de spin geométrica, y predice el efecto adicional de la velocidad de Fermi variable, que tiene consecuencias observables.

Estas consecuencias se han ilustrado estudiando el caso de una perturbación gausiana de simetría axial como ejemplo. La densidad de estados local se ha calculado de forma perturbativa en un parámetro que mide la desviación con respecto a la configuración plana. Se ha mostrado que la corrección debida al campo gauge es nula, pero la velocidad de Fermi (así como el determinante de la métrica) producen una corrección que está correlacionada con la forma de la perturbación. Estas correcciones a la densidad local de estados se pueden observar en experimentos de espectroscopía túnel. La búsqueda de una derivación microscópica alternativa del término correspondiente a la velocidad de Fermi continúa siendo un problema abierto de gran interés, que adquirirá relevancia especial si los experimentos verifican las correlaciones predichas entre densidad de estados y morfología.

El modelo geométrico propuesto puede usarse también para describir la presencia de defectos topológicos, otra perturbación a la morfología del grafeno. Las disclinaciones han sido descritas con anterioridad como fuentes singulares de curvatura [131–133], pero las

dislocaciones requieren la presencia de otro ingrediente en el modelo: representan fuentes de torsión [138, 124]. La contribución de este trabajo ha sido la discusión del formalismo para acoplar fermiones de Dirac al campo de torsión. Además se ha mostrado que el uso de este formalismo no está limitado al grafeno, y tendrá aplicaciones relevantes en sistemas de tres dimensiones con dislocaciones de tornillo y fermiones de Dirac, en particular los aislantes toplógicos [144].

Otro aspecto original de este trabajo, que tiene que ver con defectos topológicos y ha sido discutido en el capítulo 2, es el estudio de sus efectos en las propiedades magnéticas de grafeno. Muchos estudios han demostrado [48–52] que el estado fundamental magnético del sistema se ajusta a la predicción robusta del teorema de Lieb: El espín total del estado fundamental está determinado por la diferencia entre el número de átomos de distintas subredes. Aunque el teorema de Lieb se demostró para una red bipartita y solamente con interacciones tipo Hubbard, varios cálculos de primeros principios [85–87] que van más allá del modelo de Hubbard producen igualmente resultados que satisfacen esta regla, que se ha convertido en un paradigma para el estudio del magnetismo en grafeno.

La contribución de este trabajo ha sido evaluar la importancia de la hipótesis de red bipartita en la aplicabilidad de la regla de Lieb. Se ha mostrado como un solo pentágono, que hace la red no bipartita, es suficiente para cambiar de forma sustancial el estado fundamental incluso para redes de hasta 3200 átomos. Se ha presentado un cálculo de campo medio para el modelo de Hubbard que demuestra que el sistema tiene el estado fundamental de Lieb para U suficientemente alta, pero tiene una transición a un estado diferente al decrecer U. La importancia de este resultado está en el hecho de que el tipo de defectos discutidos están presentes con mucha probabilidad en grafeno, y por tanto modifican las estimaciones previas de magnetismo en las muestras.

El segundo problema general del que trata esta tesis es el problema de las interacciones de largo alcance en grafeno. En física de materia condensada, el hecho de que el potencial de Coulomb no tiene escala, y por tanto sus efectos se extienden hasta distancias arbitrariamente grandes, siempre representa un problema complicado debido a las divergencias infrarojas [153]. Este problema se resuelve en el líquido de electrones si se tiene en cuenta el apantallamiento, pero como se ha discutido en el texto la densidad de estados nula en grafeno sin dopar implica que las interacciones de Coulomb se mantienen siempre de largo alcance. Por ejemplo, el problema del apantallamiento no lineal de la impureza de Coulomb es altamente no trivial [34–37].

El problema de las divergencias infrarojas es también explícito cuando se toma un potencial de largo alcance como modelo de desorden en un sistema de materia condensada [190]. En el caso de grafeno, las impurezas cargadas de largo alcance son mecanismo importante de dispersión, pero su tratamiento en el caso sin dopar tiene precisamente este problema [189]. Además, la ausencia de una superficie de Fermi extendida impide el uso de aproximaciones autoconsistentes, que son habituales en el caso del gas de electrones bidimensional [153].

Como un primer paso hacia las propiedades de transporte del sistema, y dada la dificultad general del problema, en el capítulo 4 se han tratado los efectos de las impurezas cargadas en las propiedades espectrales de grafeno dopado. Se ha empleado apantallamiento RPA para las impurezas, y la aproximación de Born autoconsistente para el promedio sobre las posiciones de las impurezas. El régimen de dopajes en el que esta aproximacion mejora el resultado conocido de primer orden en teoría de perturbaciones se ha identificado con el valor crítico k_F^*. Los resultados muestran que las impurezas de Coulomb producen una vida media del electrón finita, lineal con el dopaje a altos dopajes pero que se desvía de forma característica de este comportamiento a dopajes por debajo del valor crítico k_F^*. La desidad de estados en el punto de Dirac es finita para dopajes por debajo de este valor.

Este cálculo ha sido llevado a cabo asumiendo una función dieléctrica tipo RPA, que se considera aplicable en el límite de alto dopaje. Como no se conoce un criterio cuantitativo para decidir a qué nivel de dopaje esta aproximación deja de ser fiable, se considera que esta cuestión merece ser tratada con más detalle. También se ha hecho notar que la aproximación de Born autoconsistente considera solamente dispersión débil, de modo que este trabajo puede extenderse más allá de este límite, por ejemplo con una aproximación de matriz T autoconsistente.

La última parte de esta tesis trata de la interacción de Coulomb de largo alcance entre electrones en grafeno. El paradigma para describir el problema electrónico de muchos cuerpos en interacción en materia condensada es el líquido de Fermi [235], que está basado en las hipótesis de una superficie de Fermi extendida e interacciones de corto alcance. Ambas hipótesis son violadas en grafeno. Este sistema ha sido estudiado desde el punto de vista del grupo de renormalización [147] para determinar su naturaleza infraroja. La renormalización de la velocidad de Fermi y su dependencia de la energía fueron establecidas en este contexto, pero el problema crucial del cálculo de observables y su relación con experimentos no ha sido tratado.

La contribución de este trabajo, presentada en el capítulo 5, ha sido la discussión sobre como se calculan observables en la teoría renormalizada, y la explicación de como relacionar el cálculo teórico con los experimentos a un order dado en teoría de perturbaciones. Se ha hecho énfasis en la semejanza de este problema con el de la medidad de la constante de estructura fina en electrodinámica cuántica [204], y se han analizado varias maneras posibles de medir el parámetro v.

Uno de los propósitos del presente trabajo ha sido clarificar el papel del regulador en la teoría de campos efectiva que describe el sistema, un problema que se originó con las discusiones sobre las correcciones de la interacción de Coulomb a la conductividad óptica [219, 42, 220]. Se ha mostrado como el proceso de renormalización hace a todos los observables independientes del regulador a cualquier orden en teoría de perturbaciones, calculando como ejemplo las primeras correciones a la conductividad.

También se ha discutido la posibildad de observar la dependencia de la velocidad de Fermi

con la energía producida por las interaciones en los experimentos analizados. Se ha sugerido que la mejor manera de medir este efecto es en muestras suspendidas, donde las interaciones son más relevantes debido a la ausencia de apantallamiento. Esta medida representaría una señal inequívoca de las interacciones en este sistema.

En resumen, se han tratado dos de los problemas abiertos más importantes en la física de grafeno, la influencia de la morfología y las interacciones de largo alcance en las propiedades electrónicas, y se han presentado contribuciones novedosas que contribuyen al entendimiento de estos problemas, discutiéndose también sus implicaciones experimentales.

A Appendix: Curvature, torsion and Dirac fermions

A.1 Differential geometry

In this section we just present a brief introduction to the concepts of differential geometry. For detailed expositions of the subject we refer to [236, 125, 237]. Consider a curved manifold, described by a set of coordinates x^μ. To this manifold we associate a metric $g_{\mu\nu}$ which defines the distance locally. A notion of paralell transport is also needed to compare vectors in different points, in order to construct meaningful derivatives. In principle the connection that represents this paralell transport and the metric need not be related, but we will see that some natural requirements for our manifold to be reasonable impose some relation between them. A first natural requirement is that relative angles and modulus of vectors are preserved under paralell transport, a property which can be encoded in the metricity condition:

$$D_\lambda g_{\mu\nu} = \partial_\lambda g_{\mu\nu} - \Gamma^\rho_{\lambda\mu} g_{\rho\nu} - \Gamma^\rho_{\lambda\nu} g_{\rho\mu} = 0, \tag{A.1}$$

this is, the covariant derivative of the metric vanishes. We will always deal with spaces that satisfy this general condition. With some manipulations [237] it can be seen that the metricity condition necesarily fixes the connection up to an arbitrary tensor K

$$\Gamma^\lambda_{\mu\nu} = \tilde{\Gamma}^\lambda_{\mu\nu} + K^\lambda_{\mu\nu}, \tag{A.2}$$

where

$$\tilde{\Gamma}^\lambda_{\mu\nu} = \left\{ \begin{array}{c} \lambda \\ \mu\ \nu \end{array} \right\}, \tag{A.3}$$

is known as the Christoffel symbol and

$$K^\lambda_{\mu\nu} = \frac{1}{2}\left(T^\lambda_{\mu\nu} + T_\mu{}^\lambda{}_\nu + T_\nu{}^\lambda{}_\mu \right), \tag{A.4}$$

is called the contortion tensor, which is itself defined in terms of the torsion

$$T^\lambda_{\mu\nu} = \Gamma^\lambda_{\mu\nu} - \Gamma^\lambda_{\nu\mu}. \tag{A.5}$$

The only restriction on K is that

$$K_{\lambda\mu\nu} = -K_{\nu\mu\lambda}, \tag{A.6}$$

hence in a d-dimensional space it has $\frac{1}{2}[d^2(d-1)]$ components. The differential geometry of a general curved space is determined by the two tensor fields $g_{\mu\nu}$ and $T^{\alpha}_{\mu\nu}$ (or, equivalently $K^{\alpha}_{\mu\nu}$). This means that when choosing a connection for a metric space, where are always free to choose the antisymmetric part of the connection (the torsion) at will. The symmetric part is the fixed by the metricity condition [1]. The usual choice is to take the torsion equal to zero, so that the metric alone determines all geometric properties. This is, for example, the case of General Relativity. In this case, the connection is called the Levi-Civita connection.

Equations formulated with a connection with torsion are of course still covariant under coordinate transformations. The important part for the covariance is that the connection transforms by adding a non-covariant piece, but it may have a tensorial part that may be arbitrary. (As we said, the contortion is a tensor, and so is the torsion. Their transformation properties can be checked to be those of usual tensors) Covariance under coordinate transformations doesn't really fix what the connection *is*, but rather how it *transforms*.

A.2 Dirac fermions in curved space

The behavior of spinors in curved spaces is more complicated than that of scalar or vector fields because their Lorentz transformation rules do not generalize easily to arbitrary coordinate systems. Instead of the usual metric $g_{\mu\nu}$ we must introduce at each point X described in arbitrary coordinates, a set of locally inertial coordinates ξ^a_X and the vielbein fields $e^a_\mu(x)$, a set of orthonormal vectors labelled by a that fixes the transformation between the local and the general coordinates:

$$e^a_\mu(X) \equiv \frac{\partial \xi^a_X(x)}{\partial x^\mu}|_{x=X}. \tag{A.7}$$

We will later compute the vielbein for our particular metric. The curved space gamma matrices $\gamma^\mu(x)$ satisfying the commutation relations

$$\{\gamma_\mu \gamma_\nu\} = 2g_{\mu\nu}, \tag{A.8}$$

are related with the constant, flat space matrices γ^a by

$$\gamma^\mu(x) = e^\mu_a \gamma_a. \tag{A.9}$$

The spin connection $\Omega_\mu(x)$ is defined from the vielbein by

$$\Omega_\mu(x) = \frac{1}{4}\gamma_a\gamma_b e^a_\lambda(x) g^{\lambda\sigma}(x) \nabla_\mu e^b_\sigma(x), \tag{A.10}$$

[1] There may be a potential source of confusion here. A symmetric connection must be torsionless, and the antisymmetric part of the connection is the torsion. However, the symmetric part of the connection is not just the Christoffel part, because the connection may be split into Christoffel and *contortion*, which has antisymmetric part, the torsion, but also a symmetric one.

with

$$\nabla_\mu e^a_\sigma = \partial_\mu e^a_\sigma - \Gamma^\lambda_{\mu\sigma} e^a_\lambda, \tag{A.11}$$

where $\Gamma^\lambda_{\mu\sigma}$ is the usual affine connection which is related to the metric tensor by [236]

$$\Gamma^\lambda_{\mu\sigma} = \frac{1}{2} g^{\nu\lambda} \{ \frac{\partial g_{\sigma\nu}}{\partial x^\mu} + \frac{\partial g_{\mu\nu}}{\partial x^\sigma} - \frac{\partial g_{\mu\sigma}}{\partial x^\nu} \}. \tag{A.12}$$

Finally, the determinant of the metric needed to define a scalar density lagrangian is given by

$$\sqrt{-g} = [\det(g_{\mu\nu})]^{1/2} = \det[e^a_\mu(x)]. \tag{A.13}$$

The massless Dirac equation in a curved spacetime is given by

$$i\gamma^\mu(\partial_\mu + \Omega_\mu)\Psi = 0, \tag{A.14}$$

where $\gamma^\mu = (\gamma^0, v_F\gamma^i)$, i=1,2. These curved γ matrices satisfy the anticommutation relations

$$\{\gamma^\mu, \gamma^\nu\} = 2g^{\mu\nu}(x), \tag{A.15}$$

and in general become functions of the point in spacetime $x = (t, \mathbf{r})$. $\Omega_\mu(x)$ is the spin connection of the spinor field that can be calculated using the tetrad formalism [125] and will be defined in the appendix A.

A.3 The gaussian bump model

Before going to the computation of the geometric factors related with the metric of eq. (3.10) we will apply the formalism to the flat space in polar coordinates what will help to clarify the physical discussion later. The two dimensional metric of the flat space in polar coordinates is

$$g_{\mu\nu} = \begin{pmatrix} 1 & 0 \\ 0 & r^2 \end{pmatrix}. \tag{A.16}$$

The affine connection $\Gamma^\lambda_{\mu\nu}$ that only depends on the metric is

$$\Gamma^r_{rr} = 0, \quad \Gamma^r_{\theta\theta} = -r, \quad \Gamma^\theta_{r\theta} = \frac{1}{r}. \tag{A.17}$$

Despite the fact that the spin connection appears to be non trivial, the Riemann curvature which is the "observable" quantity and does not depend on the choice of coordinates is zero as corresponds to flat space.

The vielbein fields e^a_μ satisfy:

$$g_{\mu\nu} = e^a_\mu e^b_\nu \eta_{ab}, \tag{A.18}$$

where η_{ab} is the identity matrix in two dimensions.

This relation does not fix e^a_μ uniquely. There are two natural choices: one is

$$e^a_\mu = (e^\mu_a)^{-1} = \begin{pmatrix} 1 & 0 \\ 0 & r \end{pmatrix}, \tag{A.19}$$

and the other one is

$$e^a_\mu = \begin{pmatrix} \cos\theta & -r\sin\theta \\ \sin\theta & r\cos\theta \end{pmatrix}. \tag{A.20}$$

The two choices can be visualized as associated to flat local frames that at points of constant r have fixed directions (last) or rotate with the polar angle (first). The first choice leaves the gamma matrices as in the cartesian plane and induces a constant gauge connection whose "associated magnetic field" is obviously zero.

The second choice transforms the flat gamma matrices and does not induce a gauge connection.

Let us now compute the geometric factors related with the metric of eq. (3.10). The affine connection $\Gamma^\lambda_{\mu\nu}$ for the metric (3.10) is

$$\Gamma^r_{rr} = \frac{\alpha f'}{2(1+\alpha f)}, \quad \Gamma^r_{\theta\theta} = -\tfrac{r}{1+\alpha f}, \quad \Gamma^\theta_{r\theta} = \frac{1}{r}, \tag{A.21}$$

where $f' = df/dr$, and the rest of the elements are zero or related by symmetry.

The geometrical (gaussian) curvature K of the shape given by eq. (3.6) is

$$K(r) = \frac{\alpha f'(r)}{2r(1+\alpha f(r))^2}. \tag{A.22}$$

The vielbein fields e^a_μ satisfy:

$$g_{\mu\nu} = e^a_\mu e^b_\nu \eta_{ab}, \tag{A.23}$$

where $g_{\mu\nu}$ is our metric given in eq. (3.10) and

$$\eta_{ab} = \begin{pmatrix} 1 & 0 & 0 \\ 0 & -1 & 0 \\ 0 & 0 & -1 \end{pmatrix}. \tag{A.24}$$

We choose the e^a_μ to be

$$\begin{array}{lll} e^0_t = 1 & e^0_r = 0 & e^0_\theta = 0 \\ e^1_t = 0 & e^1_r = (1+\alpha f)^{1/2}\cos\theta & e^1_\theta = -r\sin\theta \\ e^2_t = 0 & e^2_r = (1+\alpha f)^{1/2}\sin\theta & e^2_\theta = r\cos\theta \end{array} \tag{A.25}$$

that reduce to the flat set (A.20) when $\alpha = 0$. Now we can compute the spin connection coefficients,

$$\omega^{ab}_\mu = e^a_\nu \left(\partial_\mu + \Gamma^\nu_{\mu\lambda}\right) e^{b\lambda}, \tag{A.26}$$

which are found to be:

$$\omega_{\theta}^{12} = 1 - (1 + \alpha f)^{-1/2}, \tag{A.27}$$

the rest being zero or related by symmetry (the spin connection ω is antisymmetric in the upper indices [236]).

The spin connection

$$\Omega_{\mu} = \frac{1}{8}\omega_{\mu}^{ab}\left[\gamma_a, \gamma_b\right], \tag{A.28}$$

turns out to be

$$\Omega_t = 0, \quad \Omega_r = 0, \quad \Omega_{\theta} = \frac{1 - (1 + \alpha f)^{-1/2}}{2}\gamma^1\gamma^2. \tag{A.29}$$

Finally the Dirac equation coupled to the curved surface is:

$$i\gamma^a e_a{}^{\mu}\left(\partial_{\mu} + \Omega_{\mu}\right)\psi = 0. \tag{A.30}$$

Substituting all previously computed elements and with some more algebra, we can cast (A.14) into the form:

$$\left[i\gamma^0\partial_0 + i\Gamma(\theta)\partial_r + i\Gamma'(\theta)\frac{\partial_{\theta}}{r} + V(r,\theta)\right]\Psi = 0, \tag{A.31}$$

which is the flat Dirac equation in a sort of potential V given by:

$$V(r,\theta) = i\Gamma(\theta)\left[1 - (1 + \alpha f)^{-1/2}\right](\frac{1}{2r} - \partial_r). \tag{A.32}$$

A.4 The Dirac Lagrangian with torsion

In this section, we show how the Lagrangian for Dirac fermions in the presence of torsion is to be obtained. It would be tempting then to propose that the Dirac equation in the space with torsion and curvature is given by eq. (3.1) with the appropriate connection but there are some important subtleties that we will specify [238, 239].

Consider the Dirac field in flat space. The massless, manifestly hermitian Dirac Lagrangian may be written as:

$$\mathcal{L} = \int d^n x \frac{1}{2}\left[\bar{\psi}\gamma^{\mu}\partial_{\mu}\psi - \partial_{\mu}\bar{\psi}\gamma^{\mu}\psi\right]. \tag{A.33}$$

Noting that:

$$\left(\partial_{\mu}\bar{\psi}\right)\gamma^{\mu}\psi = \partial_{\mu}\left[\bar{\psi}\gamma^{\mu}\psi\right] - \bar{\psi}\gamma^{\mu}\partial_{\mu}\psi, \tag{A.34}$$

plus the fact that a total derivative doesn't affect the equations of motion (with suitable boundary conditions), the Lagrangian (A.33) can be traded for:

$$\mathcal{L} = \int d^n x \bar{\psi}\gamma^{\mu}\partial_{\mu}\psi. \tag{A.35}$$

Indeed, the Dirac equation can be derived by variation with respect to $\bar{\psi}$ of any of those Lagrangians. The simpler form (A.35) seems to be not hermitian, but this is not a problem since we can always introduce the boundary term back.

Now consider the same problem in a manifold with curvature and torsion. Consider the hermitian Lagrangian:

$$\mathcal{L} = \int d^n x \sqrt{g} \frac{1}{2} \left[\bar{\psi} \gamma^\mu D_\mu \psi - \left(D_\mu \bar{\psi} \right) \gamma^\mu \psi \right], \tag{A.36}$$

with $D_\mu = \partial_\mu - \omega_{\mu bc} \gamma^b \gamma^c$. Now the equivalent of the chain rule is:

$$\left(D_\mu \bar{\psi} \right) \gamma^\mu \psi = D_\mu \left[\bar{\psi} \gamma^\mu \psi \right] - \bar{\psi} D_\mu \left(\gamma^\mu \psi \right). \tag{A.37}$$

Note the following important point: since the covariant derivative contains gamma matrices, we can not just commute it to make it act directly on the spinor field. The "chain rule" that we have to use is really:

$$\left(D_\mu \bar{\psi} \right) \gamma^\mu \psi = D_\mu \left[\bar{\psi} \gamma^\mu \psi \right] - \bar{\psi} \gamma^\mu D_\mu \psi + 4 \omega_{\mu bc} e^{\mu b} \bar{\psi} \gamma^c \psi, \tag{A.38}$$

where we have used:

$$\gamma^b \gamma^c \gamma^a = \gamma^a \gamma^b \gamma^c + 2 \left(\gamma^b \eta^{ac} - \gamma^c \eta^{ab} \right). \tag{A.39}$$

The commutation with the gamma matrices has introduced a new term, the trace of the connection. This means that the equivalence of the simpler form given in eq. (A.35) is not just obtained by promoting the derivative to a covariant one, but it also requires the introduction of this trace [239].

In four dimensions, the following identity:

$$\gamma^a \gamma^b \gamma^c = \gamma^a g^{bc} + \gamma^c g^{ab} - \gamma^b g^{ac} + i \epsilon^{abcd} \gamma^5 \gamma^d, \tag{A.40}$$

and the definition of the connection (3.40) allows to rewrite this as:

$$\mathcal{L} = \int d^4 x \left(\bar{\psi} \gamma^a \partial_a \psi + \frac{T_{abc}}{4} \bar{\psi} \gamma^{[a} \gamma^b \gamma^{c]} \psi \right), \tag{A.41}$$

or:

$$\mathcal{L} = \int d^4 x \left(\bar{\psi} \gamma^a \partial_a \psi + i \epsilon^{abcd} T_{bcd} \bar{\psi} \gamma^5 \gamma^a \psi \right), \tag{A.42}$$

which reveals the well known result that, in General Relativity, fermions only couple to the antisymmetric part of the torsion [239]. In three dimensions using the identity:

$$[\gamma^a, \gamma^b] = -2 \epsilon^{abc} \gamma_c, \tag{A.43}$$

we can write the action in the form

$$\mathcal{L} = \int d^3 x \left(\bar{\psi} \gamma^a \partial_a \psi + i \epsilon^{abc} T_{abc} \bar{\psi} \psi \right), \tag{A.44}$$

from where the Dirac equation can be extracted directly to read

$$[\gamma^a \partial_a + i \epsilon^{abc} T_{abc}] \psi = 0, \tag{A.45}$$

Bibliography

[1] A. K. Geim. Graphene: Status and prospects. Science **324**, 1530 (2009). (cited on pages 1, 2, and 7)

[2] C. Soldano, A. Mahmood, and E. Dujardin. Production, properties and potential of graphene. cond-mat/1002.0370 (2010). (cited on p. 1)

[3] A. K. Geim and K. S. Novoselov. The rise of graphene. Nature Mat. **6**, 183 (2007). (cited on p. 1)

[4] M. I. Katsnelson. Graphene: carbon in two dimensions. Materials Today **10**, 20 (2007). (cited on p. 1)

[5] S. D. Sarma, S. Adam, E. H. Hwang, and E. Rossi. Electronic transport in two dimensional graphene. cond-mat/1003.4731 (2010). (cited on p. 1)

[6] D. S. L. Abergel, V. Apalkov, J. Berashevich, K. Ziegler, and T. Chakraborty. Properties of graphene: A theoretical perspective. cond-mat/1003.0391 (2010). (cited on p. 1)

[7] A. H. C. Neto, F. Guinea, N. M. R. Peres, K. S. Novoselov, and A. K. Geim. The electronic properties of graphene. Rev. Mod. Phys. **81**, 109 (2009). (cited on pages 1, 3, 5, 20, 31, 51, 52, 75, and 85)

[8] A. H. C. Neto, F. Guinea, and N. M. Peres. Drawing conclusions from graphene. Physics World **19**, 33 (2006). (cited on pages 1, 2, and 4)

[9] P. R. Wallace. The band theory of graphite. Phys. Rev. **71**, 622 (1947). (cited on pages 1, 3, and 43)

[10] K. S. Novoselov, A. K. Geim, S. V. Morozov, D. Jiang, Y. Zhang, S. V. Dubonos, I. V. Grigorieva, and A. A. Firsov. Electric field effect in atomically thin carbon films. Science **306**, 666 (2004). (cited on pages 2, 7, and 75)

[11] K. S. Novoselov, D. Jiang, F. Schedin, T. J. Booth, V. V. Khotkevich, S. V. Morozov, and A. K. Geim. Two-dimensional atomic crystals. Proc. Natl. Acad. Sci. U.S.A. **102**, 10451 (2005). (cited on p. 2)

[12] P. Blake, E. W. Hill, A. H. C. Neto, K. S. Novoselov, D. Jiang, R. Yang, T. J. Booth, and A. K. Geim. Making graphene visible. App. Phys. Lett. **91**, 063124 (2007). (cited on p. 2)

[13] C. Lee, X. Wei, J. W. Kysar, and J. Hone. Measurement of the elastic properties and intrinsic strength of monolayer graphene. Science **321**, 385 (2008). (cited on pages 2 and 29)

[14] L. D. Landau, E. M. Lifshitz, and L. P. Pitaevskii. *Statistical physics* (Elsevier Butterworth-Heinemann, 2006). (cited on p. 2)

[15] N. D. Mermin and H. Wagner. Absence of ferromagnetism or antiferromagnetism in one- or Two-Dimensional isotropic heisenberg models. Phys. Rev. Lett. **17**, 1133 (1966). (cited on p. 2)

[16] D. R. Nelson, T. Piran, and S. Weinberg. *Statistical mechanics of membranes and surfaces* (World Scientific Pub., 2004). (cited on pages 3 and 31)

[17] M. Ishigami, J. H. Chen, W. G. Cullen, M. S. Fuhrer, and E. D. Williams. Atomic structure of graphene on SiO2. Nano Lett. **7**, 1643 (2007). (cited on pages 3, 30, 95, and 99)

[18] V. Geringer, M. Liebmann, T. Echtermeyer, S. Runte, M. Schmidt, R. Rückamp, M. C. Lemme, and M. Morgenstern. Intrinsic and extrinsic corrugation of monolayer graphene deposited on SiO2. Phys. Rev. Lett. **102**, 076102 (2009). (cited on pages 3 and 30)

[19] C. H. Lui, L. Liu, K. F. Mak, G. W. Flynn, and T. F. Heinz. Ultraflat graphene. Nature **462**, 339 (2009). (cited on pages 3, 30, 95, and 99)

[20] J. C. Meyer, A. K. Geim, M. I. Katsnelson, K. S. Novoselov, T. J. Booth, and S. Roth. The structure of suspended graphene sheets. Nature **446**, 60 (2007). (cited on pages 3, 29, 95, and 99)

[21] B. An, S. Fukuyama, K. Yokogawa, M. Yoshimura, M. Egashira, Y. Korai, and I. Mochida. Single pentagon in a hexagonal carbon lattice revealed by scanning tunneling microscopy. App. Phys. Lett. **78**, 3696 (2001). (cited on pages 3, 7, and 14)

[22] A. Hashimoto, K. Suenaga, A. Gloter, K. Urita, and S. Iijima. Direct evidence for atomic defects in graphene layers. Nature **430**, 870 (2004). (cited on pages 3, 7, and 14)

[23] J. L. Mañes, F. Guinea, and M. A. H. Vozmediano. Existence and topological stability of fermi points in multilayered graphene. Phys. Rev. B **75**, 155424 (2007). (cited on pages 5, 32, and 75)

[24] I. F. Herbut. Explanation for the isotropy of the dirac cone in graphene. Phys. Rev. B **79**, 193405 (2009). (cited on pages 5 and 75)

[25] Y. Zhang, Y. Tan, H. L. Stormer, and P. Kim. Experimental observation of the quantum hall effect and berry's phase in graphene. Nature **438**, 201 (2005). (cited on pages 5, 7, and 75)

[26] K. S. Novoselov, A. K. Geim, S. V. Morozov, D. Jiang, M. I. Katsnelson, I. V. Grigorieva, S. V. Dubonos, and A. A. Firsov. Two-dimensional gas of massless dirac fermions in graphene. Nature **438**, 197 (2005). (cited on pages 5, 7, 53, and 75)

[27] M. Sprinkle, D. Siegel, Y. Hu, J. Hicks, A. Tejeda, A. Taleb-Ibrahimi, P. L. Fèvre, F. Bertran, S. Vizzini, H. Enriquez, S. Chiang, P. Soukiassian, C. Berger, W. de Heer, A. Lanzara, and E. Conrad. First direct observation of a nearly ideal graphene band structure. Phys. Rev. Lett. **103** (2009). (cited on pages 5, 59, 63, 85, and 86)

[28] M. Katsnelson and K. Novoselov. Graphene: New bridge between condensed matter physics and quantum electrodynamics. Solid State Commun. **143**, 3 (2007). (cited on p. 5)

[29] M. I. Katsnelson, K. S. Novoselov, and A. K. Geim. Chiral tunnelling and the klein paradox in graphene. Nature Phys. **2**, 620 (2006). (cited on p. 5)

[30] M. A. H. Vozmediano, M. I. Katsnelson, and F. Guinea. Gauge fields in graphene. cond-mat/1003.5179 (2010). (cited on pages 6, 35, 42, 95, and 99)

[31] P. M. Ostrovsky, I. V. Gornyi, and A. D. Mirlin. Electron transport in disordered graphene. Phys. Rev. B **74**, 235443 (2006). (cited on pages 6, 7, 31, 52, 95, and 99)

[32] K. I. Bolotin, F. Ghahari, M. D. Shulman, H. L. Stormer, and P. Kim. Observation of the fractional quantum hall effect in graphene. Nature **462**, 196 (2009). (cited on pages 6 and 75)

[33] X. Du, I. Skachko, F. Duerr, A. Luican, and E. Y. Andrei. Fractional quantum hall effect and insulating phase of dirac electrons in graphene. Nature **462**, 192 (2009). (cited on pages 6 and 75)

[34] M. I. Katsnelson. Nonlinear screening of charge impurities in graphene. Phys. Rev. B **74**, 201401 (2006). (cited on pages 7, 50, 51, 96, and 100)

[35] A. V. Shytov, M. I. Katsnelson, and L. S. Levitov. Vacuum polarization and screening of supercritical impurities in graphene. Phys. Rev. Lett. **99**, 236801 (2007). (cited on pages 7, 50, 51, 96, and 100)

[36] R. R. Biswas, S. Sachdev, and D. T. Son. Coulomb impurity in graphene. Phys. Rev. B **76**, 205122 (2007). (cited on pages 7, 50, 51, 96, and 100)

[37] V. M. Pereira, J. Nilsson, and A. H. C. Neto. Coulomb impurity problem in graphene. Phys. Rev. Lett. **99**, 166802 (2007). (cited on pages 7, 50, 51, 96, and 100)

[38] A. W. W. Ludwig, M. P. A. Fisher, R. Shankar, and G. Grinstein. Integer quantum hall transition: An alternative approach and exact results. Phys. Rev. B **50**, 7526 (1994). (cited on pages 7 and 52)

[39] M. Katsnelson. Zitterbewegung, chirality, and minimal conductivity in graphene. Eur. Phys. J. B **51**, 4 pages (2006). (cited on p. 7)

[40] K. Ziegler. Minimal conductivity of graphene: Nonuniversal values from the kubo formula. Phys. Rev. B **75**, 233407 (2007). (cited on p. 7)

[41] S. Ryu, C. Mudry, A. Furusaki, and A. W. W. Ludwig. Landauer conductance and twisted boundary conditions for dirac fermions in two space dimensions. Phys. Rev. B **75**, 205344 (2007). (cited on p. 7)

[42] I. F. Herbut, V. Juričić, and O. Vafek. Coulomb interaction, ripples, and the minimal conductivity of graphene. Phys. Rev. Lett. **100**, 046403 (2008). (cited on pages 7, 31, 84, 95, 97, 99, and 101)

[43] M. Orlita, C. Faugeras, P. Plochocka, P. Neugebauer, G. Martinez, D. K. Maude, A. Barra, M. Sprinkle, C. Berger, W. A. de Heer, and M. Potemski. Approaching the dirac point in High-Mobility multilayer epitaxial graphene. Phys. Rev. Lett. **101**, 267601 (2008). (cited on p. 7)

[44] Z. H. Ni, L. A. Ponomarenko, R. R. Nair, R. Yang, S. Anissimova, I. V. Grigorieva, F. Schedin, Z. X. Shen, E. H. Hill, K. S. Novoselov, and A. K. Geim. On resonant scatterers as a factor limiting carrier mobility in graphene. cond-mat/1003.0202 (2010). (cited on pages 7 and 31)

[45] J. Barzola-Quiquia, P. Esquinazi, M. Rothermel, D. Spemann, T. Butz, and N. García. Experimental evidence for two-dimensional magnetic order in proton bombarded graphite. Phys. Rev. B **76**, 161403 (2007). (cited on pages 7 and 19)

[46] H. Ohldag, T. Tyliszczak, R. Höhne, D. Spemann, P. Esquinazi, M. Ungureanu, and T. Butz. \pi -Electron ferromagnetism in Metal-Free carbon probed by soft X-Ray dichroism. Phys. Rev. Lett. **98**, 187204 (2007). (cited on pages 7 and 19)

[47] Y. Wang, Y. Huang, Y. Song, X. Zhang, Y. Ma, J. Liang, and Y. Chen. Room-Temperature ferromagnetism of graphene. Nano Lett. **9**, 220 (2009). (cited on pages 7 and 19)

[48] M. Fujita, K. Wakabayashi, K. Nakada, and K. Kusakabe. Peculiar localized state at zigzag graphite edge. J. Phys. Soc. Jpn. **65**, 1920 (1996).
(cited on pages 7, 21, 96, and 100)

[49] K. Wakabayashi, M. Fujita, H. Ajiki, and M. Sigrist. Electronic and magnetic properties of nanographite ribbons. Phys. Rev. B **59**, 8271 (1999).
(cited on pages 7, 21, 96, and 100)

[50] M. A. H. Vozmediano, M. P. López-Sancho, T. Stauber, and F. Guinea. Local defects and ferromagnetism in graphene layers. Phys. Rev. B **72**, 155121 (2005).
(cited on pages 7, 21, 96, and 100)

[51] H. Kumazaki and D. S. Hirashima. Nonmagnetic-Defect-Induced magnetism in graphene. J. Phys. Soc. Jpn. **76**, 064713 (2007). (cited on pages 7, 21, 96, and 100)

[52] J. J. Palacios, J. Fernández-Rossier, and L. Brey. Vacancy-induced magnetism in graphene and graphene ribbons. Phys. Rev. B **77**, 195428 (2008).
(cited on pages 7, 21, 96, and 100)

[53] N. D. Mermin. The topological theory of defects in ordered media. Rev. Mod. Phys. **51**, 591 (1979). (cited on p. 11)

[54] J. P. Hirth and J. Lothe. *Theory of dislocations* (Krieger Pub. Co., 1992). (cited on p. 12)

[55] A. Stone and D. Wales. Theoretical studies of icosahedral c60 and some related species. Chem. Phys. Lett. **128**, 501 (1986). (cited on p. 13)

[56] M. T. Lusk and L. D. Carr. Nanoengineering defect structures on graphene. Phys. Rev. Lett. **100**, 175503 (2008). (cited on p. 13)

[57] R. Saito, G. Dresselhaus, and M. S. Dresselhaus. *Physical properties of carbon nanotubes* (Imperial College Press, 1998). (cited on p. 13)

[58] J. Charlier. Defects in carbon nanotubes. Acc. Chem. Res. **35**, 1063 (2002).
(cited on p. 13)

[59] R. Saito, G. Dresselhaus, and M. S. Dresselhaus. Topological defects in large fullerenes. Chem. Phys. Lett. **195**, 537 (1992). (cited on p. 13)

[60] A. Maiti, C. J. Brabec, and J. Bernholc. Structure and energetics of single and multilayer fullerene cages. Phys. Rev. Lett. **70**, 3023 (1993). (cited on p. 13)

[61] J. Charlier, T. W. Ebbesen, and P. Lambin. Structural and electronic properties of pentagon-heptagon pair defects in carbon nanotubes. Phys. Rev. B **53**, 11108 (1996).
(cited on p. 13)

[62] L. Chico, V. H. Crespi, L. X. Benedict, S. G. Louie, and M. L. Cohen. Pure carbon nanoscale devices: Nanotube heterojunctions. Phys. Rev. Lett. **76**, 971 (1996). (cited on p. 13)

[63] H. Terrones, M. Terrones, E. Hernández, N. Grobert, J. Charlier, and P. M. Ajayan. New metallic allotropes of planar and tubular carbon. Phys. Rev. Lett. **84**, 1716 (2000). (cited on p. 13)

[64] C. P. Ewels, M. I. Heggie, and P. R. Briddon. Adatoms and nanoengineering of carbon. Chem. Phys. Lett. **351**, 178 (2002). (cited on p. 13)

[65] M. T. Lusk, D. T. Wu, and L. D. Carr. Graphene nanoengineering and the Inverse-Stone-Thrower-Wales defect. cond-mat/0902.4494 (2009). (cited on p. 13)

[66] A. Carpio and L. L. Bonilla. Periodized discrete elasticity models for defects in graphene. Phys. Rev. B **78**, 085406 (2008). (cited on p. 13)

[67] J. Coraux, A. T. N'Diaye, C. Busse, and T. Michely. Structural coherency of graphene on ir(111). Nano Lett. **8**, 565 (2008). (cited on p. 14)

[68] J. C. Meyer, C. Kisielowski, R. Erni, M. D. Rossell, M. F. Crommie, and A. Zettl. Direct imaging of lattice atoms and topological defects in graphene membranes. Nano Lett. **8**, 3582 (2008). (cited on p. 14)

[69] M. H. Gass, U. Bangert, A. L. Bleloch, P. Wang, R. R. Nair, and G. K. Free-standing graphene at atomic resolution. Nature Nanotech. **3**, 676 (2008). (cited on p. 14)

[70] N. W. Ashcroft and N. D. Mermin. *Solid state physics* (Saunders College, 1976). (cited on pages 15 and 90)

[71] D. Feng and G. Jin. *Introduction to condensed matter physics* (World Scientific, 2005). (cited on pages 15 and 20)

[72] L. Pisani, J. A. Chan, B. Montanari, and N. M. Harrison. Electronic structure and magnetic properties of graphitic ribbons. Phys. Rev. B **75**, 064418 (2007). (cited on pages 16 and 20)

[73] S. Reich, J. Maultzsch, C. Thomsen, and P. Ordejón. Tight-binding description of graphene. Phys. Rev. B **66**, 035412 (2002). (cited on p. 16)

[74] R. Moradian and A. Fathalian. Ferromagnetic semiconductor single-wall carbon nanotubes. Nanotechnology **17**, 1835 (2006). (cited on p. 19)

[75] S. Okada and A. Oshiyama. Magnetic ordering in hexagonally bonded sheets with First-Row elements. Phys. Rev. Lett. **87**, 146803 (2001). (cited on p. 19)

[76] K. Kusakabe and M. Maruyama. Magnetic nanographite. Phys. Rev. B **67**, 092406 (2003). (cited on p. 20)

[77] J. Hubbard. Electron correlations in narrow energy bands. Proc. Roy. Soc. A **276**, 238 (1963). (cited on p. 20)

[78] V. M. Pereira, F. Guinea, J. M. B. L. dos Santos, N. M. R. Peres, and A. H. C. Neto. Disorder induced localized states in graphene. Phys. Rev. Lett. **96**, 036801 (2006). (cited on pages 20 and 52)

[79] V. M. Pereira, J. M. B. L. dos Santos, and A. H. C. Neto. Modeling disorder in graphene. Phys. Rev. B **77**, 115109 (2008). (cited on pages 20 and 52)

[80] M. M. Ugeda, I. Brihuega, F. Guinea, and J. M. Gómez-Rodríguez. Missing atom as a source of carbon magnetism. Phys. Rev. Lett. **104**, 096804 (2010). (cited on p. 20)

[81] J. Fernández-Rossier and J. J. Palacios. Magnetism in graphene nanoislands. Phys. Rev. Lett. **99**, 177204 (2007). (cited on p. 20)

[82] E. H. Lieb. Two theorems on the hubbard model. Phys. Rev. Lett. **62**, 1201 (1989). (cited on pages 20, 21, and 22)

[83] E. V. Castro, N. M. R. Peres, T. Stauber, and N. A. P. Silva. Low-Density ferromagnetism in biased bilayer graphene. Phys. Rev. Lett. **100**, 186803 (2008). (cited on p. 21)

[84] E. V. Castro, M. P. López-Sancho, and M. A. H. Vozmediano. Pinning and switching of magnetic moments in bilayer graphene. New J. Phys. **11**, 095017 (2009). (cited on p. 21)

[85] L. Pisani, B. Montanari, and N. M. Harrison. A defective graphene phase predicted to be a room temperature ferromagnetic semiconductor. New J. Phys. **10**, 033002 (2008). (cited on pages 21, 96, and 100)

[86] P. O. Lehtinen, A. S. Foster, A. Ayuela, A. Krasheninnikov, K. Nordlund, and R. M. Nieminen. Magnetic properties and diffusion of adatoms on a graphene sheet. Phys. Rev. Lett. **91**, 017202 (2003). (cited on pages 21, 96, and 100)

[87] Y. Ma, P. O. Lehtinen, A. S. Foster, and R. M. Nieminen. Magnetic properties of vacancies in graphene and single-walled carbon nanotubes. New J. Phys. **6**, 68 (2004). (cited on pages 21, 96, and 100)

[88] A. V. Krasheninnikov and F. Banhart. Engineering of nanostructured carbon materials with electron or ion beams. Nature Mat. **6**, 723 (2007). (cited on p. 22)

[89] G. Lee, C. Z. Wang, E. Yoon, N. Hwang, D. Kim, and K. M. Ho. Diffusion, coalescence, and reconstruction of vacancy defects in graphene layers. Phys. Rev. Lett. **95**, 205501 (2005). (cited on p. 22)

[90] P. O. Lehtinen, A. S. Foster, Y. Ma, A. V. Krasheninnikov, and R. M. Nieminen. Irradiation-Induced magnetism in graphite: A density functional study. Phys. Rev. Lett. **93**, 187202 (2004). (cited on p. 22)

[91] E. J. Duplock, M. Scheffler, and P. J. D. Lindan. Hallmark of perfect graphene. Phys. Rev. Lett. **92**, 225502 (2004). (cited on p. 25)

[92] O. Y. Kontsevoi, Y. N. Gornostyrev, O. N. Mryasov, A. J. Freeman, M. I. Katsnelson, and A. V. Trefilov. Electron localization on dislocations in metals: Real-space first-principles calculations. Phys. Rev. B **64**, 134103 (2001). (cited on p. 26)

[93] O. Y. Kontsevoi, O. N. M. Yu, N. Gornostyrev, A. J. Freeman, M. I. Katsnelson, and A. V. Trefilov. Real-space first-principles electronic structure of edge dislocations: NiAl. Philos. Mag. Lett. **78**, 427 (1998). (cited on p. 26)

[94] S. Sorella and E. Tosatti. Semi-Metal-Insulator transition of the hubbard model in the honeycomb lattice. Europhys. Lett. **19**, 699 (1992). (cited on p. 26)

[95] T. J. Booth, P. Blake, R. R. Nair, D. Jiang, E. W. Hill, U. Bangert, A. Bleloch, M. Gass, K. S. Novoselov, M. I. Katsnelson, and A. K. Geim. Macroscopic graphene membranes and their extraordinary stiffness. Nano Lett. **8**, 2442 (2008). (cited on p. 29)

[96] K. S. Kim, Y. Zhao, H. Jang, S. Y. Lee, J. M. Kim, K. S. Kim, J. Ahn, P. Kim, J. Choi, and B. H. Hong. Large-scale pattern growth of graphene films for stretchable transparent electrodes. Nature **457**, 706 (2009). (cited on p. 29)

[97] W. Bao, F. Miao, Z. Chen, H. Zhang, W. Jang, C. Dames, and C. N. Lau. Controlled ripple texturing of suspended graphene and ultrathin graphite membranes. Nature Nanotech. **4**, 562 (2009). (cited on pages 29 and 30)

[98] E. Stolyarova, K. T. Rim, S. Ryu, J. Maultzsch, P. Kim, L. E. Brus, T. F. Heinz, M. S. Hybertsen, and G. W. Flynn. High-resolution scanning tunneling microscopy imaging of mesoscopic graphene sheets on an insulating surface. Proc. Natl. Acad. Sci. U.S.A. **104**, 9209 (2007). (cited on pages 30, 95, and 99)

[99] Y. Zhang, V. W. Brar, F. Wang, C. Girit, Y. Yayon, M. Panlasigui, A. Zettl, and M. F. Crommie. Giant phonon-induced conductance in scanning tunnelling spectroscopy of gate-tunable graphene. Nature Phys. **4**, 627 (2008). (cited on p. 30)

[100] M. L. Teague, A. P. Lai, J. Velasco, C. R. Hughes, A. D. Beyer, M. W. Bockrath, C. N. Lau, and N. Yeh. Evidence for Strain-Induced local conductance modulations in Single-Layer graphene on SiO2. Nano Lett. **9**, 2542 (2009). (cited on p. 30)

[101] Y. Zhang, V. W. Brar, C. Girit, A. Zettl, and M. F. Crommie. Origin of spatial charge inhomogeneity in graphene. Nature Phys. **5**, 722 (2009). (cited on pages 30, 31, and 85)

[102] A. Deshpande, W. Bao, F. Miao, C. N. Lau, and B. J. LeRoy. Spatially resolved spectroscopy of monolayer graphene on SiO2. Phys. Rev. B **79**, 205411 (2009). (cited on pages 30 and 85)

[103] P. Mallet, F. Varchon, C. Naud, L. Magaud, C. Berger, and J. Veuillen. Electron states of mono- and bilayer graphene on SiC probed by scanning-tunneling microscopy. Phys. Rev. B **76**, 041403 (2007). (cited on p. 30)

[104] V. W. Brar, Y. Zhang, Y. Yayon, T. Ohta, J. L. McChesney, A. Bostwick, E. Rotenberg, K. Horn, and M. F. Crommie. Scanning tunneling spectroscopy of inhomogeneous electronic structure in monolayer and bilayer graphene on SiC. App. Phys. Lett. **91**, 122102 (2007). (cited on p. 30)

[105] G. M. Rutter, J. N. Crain, N. P. Guisinger, T. Li, P. N. First, and J. A. Stroscio. Scattering and interference in epitaxial graphene. Science **317**, 219 (2007). (cited on pages 30 and 85)

[106] I. Brihuega, P. Mallet, C. Bena, S. Bose, C. Michaelis, L. Vitali, F. Varchon, L. Magaud, K. Kern, and J. Veuillen. Quasiparticle chirality in epitaxial graphene probed at the nanometer scale. Phys. Rev. Lett. **101** (2008). (cited on p. 30)

[107] J. Sabio, C. Seoánez, S. Fratini, F. Guinea, A. H. C. Neto, and F. Sols. Electrostatic interactions between graphene layers and their environment. Phys. Rev. B **77**, 195409 (2008). (cited on p. 30)

[108] K. Xu, P. Cao, and J. R. Heath. Scanning tunneling microscopy characterization of the electrical properties of wrinkles in exfoliated graphene monolayers. Nano Lett. **9**, 4446 (2009). (cited on p. 30)

[109] G. Li, A. Luican, and E. Y. Andrei. Scanning tunneling spectroscopy of graphene on graphite. Phys. Rev. Lett. **102**, 176804 (2009). (cited on pages 30, 75, and 86)

[110] E. Stolyarova, D. Stolyarov, K. Bolotin, S. Ryu, L. Liu, K. T. Rim, M. Klima, M. Hybertsen, I. Pogorelsky, I. Pavlishin, K. Kusche, J. Hone, P. Kim, H. L. Stormer, V. Yakimenko, and G. Flynn. Observation of graphene bubbles and effective mass transport under graphene films. Nano Lett. **9**, 332 (2009). (cited on p. 31)

[111] S. Morozov, K. Novoselov, M. Katsnelson, F. Schedin, L. Ponomarenko, D. Jiang, and A. Geim. Strong suppression of weak localization in graphene. Phys. Rev. Lett. **97** (2006). (cited on pages 31 and 35)

[112] J. Martin, N. Akerman, G. Ulbricht, T. Lohmann, J. H. Smet, K. von Klitzing, and A. Yacoby. Observation of electron-hole puddles in graphene using a scanning single-electron transistor. Nature Phys. **4**, 144 (2008). (cited on pages 31 and 85)

[113] V. Galitski, S. Adam, and S. D. Sarma. Statistics of random voltage fluctuations and the low-density residual conductivity of graphene. Phys. Rev. B **76**, 245405 (2007). (cited on p. 31)

[114] E. Rossi, S. Adam, and S. D. Sarma. Effective medium theory for disordered two-dimensional graphene. Phys. Rev. B **79**, 245423 (2009). (cited on pages 31 and 53)

[115] E. Kim and A. H. Castro Neto. Graphene as an electronic membrane. Europhys. Lett. **84**, 57007 (2008). (cited on pages 31 and 39)

[116] A. F. Morpurgo and F. Guinea. Intervalley scattering, Long-Range disorder, and effective Time-Reversal symmetry breaking in graphene. Phys. Rev. Lett. **97**, 196804 (2006). (cited on pages 31, 35, 95, and 99)

[117] K. Ziegler. Long-range correlations in disordered graphene. Phys. Rev. B **78**, 125401 (2008). (cited on pages 31, 52, 95, and 99)

[118] M. M. Fogler, F. Guinea, and M. I. Katsnelson. Pseudomagnetic fields and ballistic transport in a suspended graphene sheet. Phys. Rev. Lett. **101**, 226804 (2008). (cited on pages 31, 95, and 99)

[119] O. Vafek. Dynamical conductivity of ungated suspended graphene. cond-mat/0810.3697 (2008). (cited on pages 31, 95, and 99)

[120] A. Cortijo and M. A. H. Vozmediano. Minimal conductivity of rippled graphene with topological disorder. Phys. Rev. B **79**, 184205 (2009). (cited on pages 31, 44, 54, 95, and 99)

[121] T. Stauber, N. M. R. Peres, and F. Guinea. Electronic transport in graphene: A semiclassical approach including midgap states. Phys. Rev. B **76**, 205423 (2007). (cited on pages 31, 54, 95, and 99)

[122] M. I. Katsnelson and A. K. Geim. Electron scattering on microscopic corrugations in graphene. Phil. Trans. R. Soc. A **366**, 195 (2008). (cited on pages 31, 53, 95, and 99)

[123] I. E. Dzyaloshinskii and G. E. Volovick. Poisson brackets in condensed matter physics. Ann. Phys. **125**, 67 (1980). (cited on p. 32)

[124] M. O. Katanaev and I. V. Volovich. Theory of defects in solids and three-dimensional gravity. Ann. Phys. **216**, 1 (1992). (cited on pages 32, 41, 95, and 100)

[125] N. D. Birrell and P. C. W. Davies. *Quantum fields in curved space* (Cambridge University Press, 1984). (cited on pages 32, 103, and 105)

[126] J. González, F. Guinea, and M. A. H. Vozmediano. Continuum approximation to fullerene molecules. Phys. Rev. Lett. **69**, 172 (1992). (cited on p. 33)

[127] J. González, F. Guinea, and M. A. H. Vozmediano. Electrostatic screening in fullerene molecules. Mod. Phys. Lett. B **7**, 1593 (1993). (cited on p. 33)

[128] J. González, F. Guinea, and M. A. H. Vozmediano. Theoretical aspects of fullerenes. Int. J. Mod. Phys. B **7**, 4331 (1993). (cited on p. 33)

[129] D. V. Kolesnikov and V. A. Osipov. Electronic properties of curved carbon nanostructures. Rom. J. Phys. **50**, 457 (2005). (cited on p. 33)

[130] D. V. Kolesnikov and V. A. Osipov. The continuum gauge field-theory model for low-energy electronic states of icosahedral fullerenes. Eur. Phys. J. B **49**, 465 (2006). (cited on p. 33)

[131] C. Furtado and F. Moraes. On the binding of electrons and holes to disclinations. Phys. Lett. A **188**, 394 (1994). (cited on pages 33, 95, and 99)

[132] A. Cortijo and M. A. Vozmediano. Effects of topological defects and local curvature on the electronic properties of planar graphene. Nucl. Phys. B **763**, 293 (2007). (cited on pages 33, 38, 95, and 99)

[133] A. Cortijo and M. A. H. Vozmediano. Electronic properties of curved graphene sheets. Europhys. Lett. **77**, 47002 (2007). (cited on pages 33, 38, 95, and 99)

[134] E. Aurell. Torsion and electron motion in quantum dots with crystal lattice dislocations. J. Phys. A **32**, 571 (1999). (cited on p. 33)

[135] A. Mesaros, D. Sadri, and J. Zaanen. Parallel transport of electrons in graphene parallels gravity. cond-mat/0909.2703 (2009). (cited on p. 33)

[136] I. S. Gradshteyn and I. M. Ryzhik. *Table of integrals, series, and products* (Academic Press, 1980). (cited on p. 37)

[137] K. Kondo. On the analytical and physical foundations of the theory of dislocations and yielding by the differential geometry of continua. Int. J. Eng. Sci. **2**, 219 (1964). (cited on p. 41)

[138] H. Kleinert. *Gauge Fields in Condensed Matter: Stresses and defects* (World Scientific, 1989). (cited on pages 41, 95, and 100)

[139] G. D. Mahan. *Many-particle physics* (Springer, 2000). (cited on pages 41, 45, and 49)

[140] G. R. Hennig. Screw dislocations in graphite. Science **147**, 733 (1965). (cited on p. 43)

[141] J. C. Slonczewski and P. R. Weiss. Band structure of graphite. Phys. Rev. **109**, 272 (1958). (cited on p. 43)

[142] M. Orlita, C. Faugeras, G. Martinez, D. K. Maude, M. L. Sadowski, J. M. Schneider, and M. Potemski. Magneto-transmission as a probe of dirac fermions in bulk graphite. J. Phys.: Condens. Matter **20**, 454223 (2008). (cited on p. 43)

[143] S. Y. Zhou, G. Gweon, J. Graf, A. V. Fedorov, C. D. Spataru, R. D. Diehl, Y. Kopelevich, D. Lee, S. G. Louie, and A. Lanzara. First direct observation of dirac fermions in graphite. Nature Phys. **2**, 595 (2006). (cited on p. 43)

[144] J. Moore. Topological insulators: The next generation. Nature Phys. **5**, 378 (2009). (cited on pages 43, 96, and 100)

[145] M. Z. Hasan and C. L. Kane. Topological insulators. cond-mat/1002.3895 (2010). (cited on p. 43)

[146] Y. Xia, D. Qian, D. Hsieh, L. Wray, A. Pal, H. Lin, A. Bansil, D. Grauer, Y. S. Hor, R. J. Cava, and M. Z. Hasan. Observation of a large-gap topological-insulator class with a single dirac cone on the surface. Nature Phys. **5**, 398 (2009). (cited on p. 43)

[147] J. González, F. Guinea, and M. A. H. Vozmediano. Non-Fermi liquid behavior of electrons in the half-filled honeycomb lattice (A renormalization group approach). Nucl. Phys. B **424**, 595 (1994).
(cited on pages 44, 75, 76, 78, 79, 81, 88, 89, 91, 92, 97, and 101)

[148] J. González, F. Guinea, and M. A. H. Vozmediano. Electron-electron interactions in graphene sheets. Phys. Rev. B **63**, 134421 (2001). (cited on p. 44)

[149] T. Stauber, F. Guinea, and M. A. H. Vozmediano. Disorder and interaction effects in two-dimensional graphene sheets. Phys. Rev. B **71**, 041406 (2005). (cited on p. 44)

[150] P. A. Lee and T. V. Ramakrishnan. Disordered electronic systems. Rev. Mod. Phys. **57**, 287 (1985). (cited on p. 45)

[151] J. Rammer. *Quantum transport theory* (Westview Press, 1998).
(cited on pages 45, 46, 47, and 49)

[152] A. Altland and B. Simons. *Condensed matter field theory* (Cambridge University Press, 2006). (cited on pages 45, 47, 49, and 83)

[153] H. Bruus and K. Flensberg. *Many-body quantum theory in condensed matter physics* (Oxford University Press, 2004). (cited on pages 45, 48, 49, 96, and 100)

[154] E. N. Economou. *Green's functions in quantum physics* (Springer, 2006). (cited on pages 45 and 48)

[155] R. G. Newton. *Scattering theory of waves and particles* (Courier Dover Publications, 2002). (cited on pages 47 and 49)

[156] T. Ando, A. B. Fowler, and F. Stern. Electronic properties of two-dimensional systems. Rev. Mod. Phys. **54**, 437 (1982). (cited on pages 49, 50, and 51)

[157] E. Zaremba, I. Nagy, and P. M. Echenique. Nonlinear screening in Two-Dimensional electron gases. Phys. Rev. Lett. **90**, 046801 (2003). (cited on p. 50)

[158] A. Efros. Non-linear screening and the background density of 2DEG states in magnetic field. Solid State Commun. **67**, 1019 (1988). (cited on p. 50)

[159] T. Ando. Effect of level broadening on the polarizability in a Two-Dimensional system. J. Phys. Soc. Jpn. **51**, 3215 (1982). (cited on p. 50)

[160] S. D. Sarma. Theory for the polarizability function of an electron layer in the presence of collisional broadening effects and its experimental implications. Phys. Rev. Lett. **50**, 211 (1983). (cited on p. 50)

[161] D. P. DiVincenzo and E. J. Mele. Self-consistent effective-mass theory for intralayer screening in graphite intercalation compounds. Phys. Rev. B **29**, 1685 (1984). (cited on pages 50 and 51)

[162] M. M. Fogler, D. S. Novikov, and B. I. Shklovskii. Screening of a hypercritical charge in graphene. Phys. Rev. B **76**, 233402 (2007). (cited on pages 50 and 51)

[163] I. S. Terekhov, A. I. Milstein, V. N. Kotov, and O. P. Sushkov. Screening of coulomb impurities in graphene. Phys. Rev. Lett. **100**, 076803 (2008). (cited on pages 50 and 51)

[164] M. Ghaznavi, Z. L. Miskovic, and F. O. Goodman. Non-linear screening of charged impurity by graphene. cond-mat/0910.3614 (2009). (cited on p. 50)

[165] S. Gangadharaiah, A. M. Farid, and E. G. Mishchenko. Charge response function and a novel plasmon mode in graphene. Phys. Rev. Lett. **100**, 166802 (2008). (cited on p. 50)

[166] S. D. Sarma, B. Y. Hu, E. H. Hwang, and W. Tse. Electron-Electron interactions in graphene. cond-mat/0708.3239 (2007). (cited on p. 50)

[167] M. Polini, A. H. MacDonald, and G. Vignale. Drude weight, plasmon dispersion, and pseudospin response in doped graphene sheets. cond-mat/0901.4528 (2009). (cited on p. 50)

[168] K. W. K. Shung. Dielectric function and plasmon structure of stage-1 intercalated graphite. Phys. Rev. B **34**, 979 (1986). (cited on p. 50)

[169] T. Ando. Screening effect and impurity scattering in monolayer graphene. J. Phys. Soc. Jpn **75**, 074716 (2006). (cited on pages 50 and 52)

[170] E. H. Hwang and S. D. Sarma. Dielectric function, screening, and plasmons in two-dimensional graphene. Phys. Rev. B **75**, 205418 (2007). (cited on p. 50)

[171] B. Wunsch, T. Stauber, F. Sols, and F. Guinea. Dynamical polarization of graphene at finite doping. New J. Phys. **8**, 318 (2006). (cited on p. 50)

[172] E. Fradkin. Critical behavior of disordered degenerate semiconductors. II. spectrum and transport properties in mean-field theory. Phys. Rev. B **33**, 3263 (1986). (cited on pages 52 and 53)

[173] A. Altland, B. D. Simons, and M. R. Zirnbauer. Theories of low-energy quasi-particle states in disordered d-wave superconductors. Phys. Rep. **359**, 283 (2002). (cited on pages 52 and 53)

[174] N. M. R. Peres, F. Guinea, and A. H. C. Neto. Electronic properties of disordered two-dimensional carbon. Phys. Rev. B **73**, 125411 (2006). (cited on pages 52 and 59)

[175] N. H. Shon and T. Ando. Quantum transport in two dimensional graphite system. J. Phys. Soc. Jpn. **67**, 2421 (1998). (cited on pages 52 and 53)

[176] B. Y. Hu, E. H. Hwang, and S. D. Sarma. Density of states of disordered graphene. Phys. Rev. B **78**, 165411 (2008). (cited on pages 52, 59, and 60)

[177] S. Wu, L. Jing, Q. Li, Q. W. Shi, J. Chen, H. Su, X. Wang, and J. Yang. Average density of states in disordered graphene systems. Phys. Rev. B **77**, 195411 (2008). (cited on p. 52)

[178] E. H. Hwang and S. D. Sarma. Quasiparticle spectral function in doped graphene: Electron-electron interaction effects in ARPES. Phys. Rev. B **77**, 081412 (2008). (cited on p. 52)

[179] A. A. Nersesyan, A. M. Tsvelik, and F. Wenger. Disorder effects in two-dimensional fermi systems with conical spectrum: exact results for the density of states. Nucl. Phys. B **438**, 561 (1995). (cited on p. 53)

[180] I. L. Aleiner and K. B. Efetov. Effect of disorder on transport in graphene. Phys. Rev. Lett. **97**, 236801 (2006). (cited on p. 53)

[181] K. Nomura and A. H. MacDonald. Quantum transport of massless dirac fermions. Phys. Rev. Lett. **98**, 076602 (2007). (cited on pages 53 and 60)

[182] Y. Tan, Y. Zhang, K. Bolotin, Y. Zhao, S. Adam, E. H. Hwang, S. D. Sarma, H. L. Stormer, and P. Kim. Measurement of scattering rate and minimum conductivity in graphene. Phys. Rev. Lett. **99**, 246803 (2007). (cited on p. 53)

[183] J. Chen, C. Jang, S. Adam, M. S. Fuhrer, E. D. Williams, and M. Ishigami. Charged-impurity scattering in graphene. Nature Phys. **4**, 377 (2008). (cited on p. 53)

[184] L. A. Ponomarenko, R. Yang, T. M. Mohiuddin, M. I. Katsnelson, K. S. Novoselov, S. V. Morozov, A. A. Zhukov, F. Schedin, E. W. Hill, and A. K. Geim. Effect of a high-kappa environment on charge carrier mobility in graphene. Phys. Rev. Lett. **102**, 206603 (2009). (cited on p. 53)

[185] T. O. Wehling, S. Yuan, A. I. Lichtenstein, and M. I. Katsnelson. Resonant scattering by realistic impurities in graphene. cond-mat/1003.0609 (2010). (cited on p. 54)

[186] S. Hands and C. Strouthos. Quantum critical behavior in a graphenelike model. Phys. Rev. B **78**, 165423 (2008). (cited on pages 54 and 88)

[187] X. Hong, K. Zou, and J. Zhu. Quantum scattering time and its implications on scattering sources in graphene. Phys. Rev. B **80**, 241415 (2009). (cited on pages 54 and 55)

[188] M. Monteverde, C. Ojeda-Aristizabal, R. Weil, K. Bennaceur, M. Ferrier, S. Guéron, C. Glattli, H. Bouchiat, J. N. Fuchs, and D. L. Maslov. Transport and elastic scattering times as probes of the nature of impurity scattering in Single-Layer and bilayer graphene. Phys. Rev. Lett. **104**, 126801 (2010). (cited on pages 54 and 55)

[189] D. V. Khveshchenko. Effects of long-range correlated disorder on dirac fermions in graphene. Phys. Rev. B **75**, 241406 (2007). (cited on pages 54, 96, and 100)

[190] A. G. Aronov, A. D. Mirlin, and P. Wolfle. Localization of charged quantum particles in a static random magnetic field. Phys. Rev. B **49**, 16609 (1994). (cited on pages 54, 96, and 100)

[191] D. V. Khveshchenko and A. G. Yashenkin. Planar dirac fermions in long-range-correlated random vector potential. Phys. Lett. A **309**, 363 (2003). (cited on p. 54)

[192] A. Bostwick, T. Ohta, J. L. McChesney, T. Seyller, K. Horn, and E. Rotenberg. Renormalization of graphene bands by many-body interactions. Solid State Commun. **143**, 63 (2007). (cited on p. 59)

[193] S. Y. Zhou, G. Gweon, A. V. Fedorov, P. N. First, W. A. de Heer, D. Lee, F. Guinea, A. H. C. Neto, and A. Lanzara. Substrate-induced bandgap opening in epitaxial graphene. Nature Mat. **6**, 770 (2007). (cited on pages 59 and 85)

[194] A. Bostwick, T. Ohta, T. Seyller, K. Horn, and E. Rotenberg. Quasiparticle dynamics in graphene. Nature Phys. **3**, 36 (2007). (cited on pages 59, 75, and 85)

[195] P. W. Anderson. *Basic notions of condensed matter physics* (Perseus Books Group, 1997). (cited on p. 65)

[196] J. Zinn-Justin. *Quantum field theory and critical phenomena* (Oxford University Press, 2002). (cited on p. 65)

[197] K. G. Wilson. The renormalization group: Critical phenomena and the kondo problem. Rev. Mod. Phys. **47**, 773 (1975). (cited on p. 66)

[198] N. N. Bogoliubov and D. V. Shirkov. *Introduction to the theory of quantized fields* (John Wiley, 1980). (cited on pages 66 and 73)

[199] P. Ramond. *Field theory* (Perseus Books, 1997). (cited on pages 66, 67, 70, 74, 88, and 91)

[200] G. P. Lepage. What is renormalization? hep-ph/0506330 (2005). (cited on p. 66)

[201] J. Polchinski. Effective field theory and the fermi surface. hep-th/9210046 (1992). (cited on p. 66)

[202] H. Georgi. Effective field theory. Annu. Rev. Nucl. Part. Sci. **43**, 209 (1993). (cited on p. 66)

[203] M. L. Bellac. *Quantum and statistical field theory* (Oxford University Press, 1991). (cited on pages 67, 68, 73, 74, 81, and 90)

[204] M. E. Peskin and D. V. Schroeder. *An introduction to quantum field theory* (Westview Press, 1995). (cited on pages 67, 68, 69, 74, 83, 90, 97, and 101)

[205] D. Hanneke, S. Fogwell, and G. Gabrielse. New measurement of the electron magnetic moment and the fine structure constant. Phys. Rev. Lett. **100** (2008). (cited on p. 69)

[206] A. V. Smilga. *Lectures on quantum chromodynamics* (World Scientific, 2001). (cited on p. 74)

[207] R. Shankar. Renormalization-group approach to interacting fermions. Rev. Mod. Phys. **66**, 129 (1994). (cited on p. 75)

[208] T. Giamarchi. *Quantum Physics in one dimension* (Oxford University Press, 2004). (cited on p. 75)

[209] Z. Jiang, E. A. Henriksen, L. C. Tung, Y. Wang, M. E. Schwartz, M. Y. Han, P. Kim, and H. L. Stormer. Infrared spectroscopy of landau levels of graphene. Phys. Rev. Lett. **98**, 197403 (2007). (cited on p. 75)

[210] Z. Q. Li, E. A. Henriksen, Z. Jiang, Z. Hao, M. C. Martin, P. Kim, H. L. Stormer, and D. N. Basov. Dirac charge dynamics in graphene by infrared spectroscopy. Nature Phys. **4**, 532 (2008). (cited on pages 75 and 86)

[211] R. R. Nair, P. Blake, A. N. Grigorenko, K. S. Novoselov, T. J. Booth, T. Stauber, N. M. R. Peres, and A. K. Geim. Fine structure constant defines visual transparency of graphene. Science **320**, 1308 (2008). (cited on pages 75 and 86)

[212] S. Y. Zhou, D. A. Siegel, A. V. Fedorov, and A. Lanzara. Kohn anomaly and interplay of electron-electron and electron-phonon interactions in epitaxial graphene. Phys. Rev. B **78**, 193404 (2008). (cited on p. 75)

[213] J. González, F. Guinea, and M. A. H. Vozmediano. Marginal-Fermi-liquid behavior from two-dimensional coulomb interaction. Phys. Rev. B **59**, R2474 (1999). (cited on p. 75)

[214] I. Herbut. Interactions and phase transitions on graphene's honeycomb lattice. Phys. Rev. Lett. **97**, 146401 (2006). (cited on pages 76 and 88)

[215] E. G. Mishchenko. Effect of Electron-Electron interactions on the conductivity of clean graphene. Phys. Rev. Lett. **98**, 216801 (2007). (cited on p. 81)

[216] R. Balian and J. Zinn-Justin (editors) *Methods in field theory*. Proceedings of Les Houches Summer School (North-Holland, 1976). (cited on p. 83)

[217] J. C. Collins. *Renormalization* (Cambridge University Press, 1985). (cited on p. 83)

[218] S. Weinberg. *The Quantum Theory of Fields Vol. 1* (Cambridge University Press, 2005). (cited on p. 83)

[219] E. G. Mishchenko. Minimal conductivity in graphene: interaction corrections and ultraviolet anomaly. Europhys. Lett. **83**, 17005 (2008). (cited on pages 84, 97, and 101)

[220] D. E. Sheehy and J. Schmalian. Optical transparency of graphene as determined by the fine-structure constant. Phys. Rev. B **80**, 193411 (2009). (cited on pages 84, 97, and 101)

[221] K. R. Knox, S. Wang, A. Morgante, D. Cvetko, A. Locatelli, T. O. Mentes, M. A. Niño, P. Kim, and R. M. Osgood. Spectromicroscopy of single and multilayer graphene supported by a weakly interacting substrate. Phys. Rev. B **78** (2008). (cited on p. 85)

[222] G. Li and E. Y. Andrei. Observation of landau levels of dirac fermions in graphite. Nature Phys. **3**, 623 (2007). (cited on p. 86)

[223] R. S. Deacon, K. Chuang, R. J. Nicholas, K. S. Novoselov, and A. K. Geim. Cyclotron resonance study of the electron and hole velocity in graphene monolayers. Phys. Rev. B **76**, 081406 (2007). (cited on p. 86)

[224] V. G. Kravets, A. N. Grigorenko, R. R. Nair, P. Blake, S. Anisimova, K. S. Novoselov, and A. K. Geim. Optics of flat carbon - spectroscopic ellipsometry of graphene flakes. cond-mat/1003.2618 (2010). (cited on p. 86)

[225] D. V. Khveshchenko and H. Leal. Excitonic instability in layered degenerate semimetals. Nucl. Phys. B **687**, 323 (2004). (cited on p. 88)

[226] J. E. Drut and T. A. Lähde. Lattice field theory simulations of graphene. Phys. Rev. B **79**, 165425 (2009). (cited on p. 88)

[227] J. E. Drut and T. A. Lähde. Critical exponents of the semimetal-insulator transition in graphene: A monte carlo study. Phys. Rev. B **79**, 241405 (2009). (cited on p. 88)

[228] J. E. Drut and T. A. Lähde. Is graphene in vacuum an insulator? Phys. Rev. Lett. **102**, 026802 (2009). (cited on p. 88)

[229] F. Mandl and G. Shaw. *Quantum field theory* (J. Wiley, 1993). (cited on p. 89)

[230] J. D. Jackson. *Classical electrodynamics* (Wiley, 1962). (cited on p. 90)

[231] O. L. Brill and B. Goodman. Causality in the coulomb gauge. Am. J. Phys. **35**, 832 (1967). (cited on p. 90)

[232] T. Holstein, R. E. Norton, and P. Pincus. de haas-van alphen effect and the specific heat of an electron gas. Phys. Rev. B **8**, 2649 (1973). (cited on p. 90)

[233] A. M. Tsvelik. *Quantum field theory in condensed matter physics* (Cambridge University Press, 2003). (cited on p. 90)

[234] J. L. Mañes. Symmetry-based approach to electron-phonon interactions in graphene. Phys. Rev. B **76**, 045430 (2007). (cited on p. 92)

[235] G. Giuliani and G. Vignale. *Quantum theory of the electron liquid* (Cambridge University Press, 2005). (cited on pages 97 and 101)

[236] S. Weinberg. *Gravitation and cosmology: principles and applications of the general theory of relativity* (Wiley, 1972). (cited on pages 103, 105, and 107)

[237] M. Nakahara. *Geometry, topology, and physics* (CRC Press, 2003). (cited on p. 103)

[238] I. L. Shapiro. Physical aspects of the space-time torsion. Phys. Rep. **357**, 113 (2002). (cited on p. 107)

[239] R. T. Hammond. Torsion gravity. Rep. Prog. Phys. **65**, 599 (2002). (cited on pages 107 and 108)